2D SIMULATIONS BASED ON THE GENERAL TIME DEPENDENT RECIPROCAL RELATION AND INITIAL EXPERIMENTS FOR LFEIT

A THESIS SUBMITTED TO
THE GRADUATE SCHOOL OF NATURAL AND APPLIED SCIENCES
OF
MIDDLE EAST TECHNICAL UNIVERSITY

BY

MÜRSEL KARADAŞ

IN PARTIAL FULFILLMENT OF THE REQUIREMENTS
FOR
THE DEGREE OF MASTER OF SCIENCE
IN
ELECTRICAL AND ELECTRONICS ENGINEERING

SEPTEMBER 2014

Approval of the thesis:

2D SIMULATIONS BASED ON THE GENERAL TIME DEPENDENT RECIPROCAL RELATION AND INITIAL EXPERIMENTS FOR LFEIT

submitted by **MÜRSEL KARADAŞ** in partial fulfillment of the requirements for the degree of **Master of Science in Electrical and Electronics Engineering Department, Middle East Technical University** by,

Prof. Dr. Canan Özgen
Dean, Graduate School of **Natural and Applied Sciences** _____

Prof. Dr. Gönül Turhan Sayan
Head of Department, **Electrical and Electronics Engineering** _____

Prof. Dr. Nevzat Güneri Gençer
Supervisor, **Electrical and Electonics Eng. Dept., METU** _____

Examining Committee Members:

Prof. Dr.Murat Eyüboğlu
Electrical and Electonics Engineering Dept., METU _____

Prof. Dr. Nevzat Güneri Gencer
Electrical and Electonics Engineering Dept., METU _____

Prof. Dr. Ergin Atalar
Electrical and Electonics Engineering Dept., Bilkent University _____

Assoc. Prof. Dr. Yeşim Serinağaoğlu Doğrusöz
Electrical and Electonics Engineering Dept., METU _____

Assoc. Prof. Dr. Lale Alatan
Electrical and Electonics Engineering Dept., METU _____

Date: 05.09.2014

I hereby declare that all information in this document has been obtained and presented in accordance with academic rules and ethical conduct. I also declare that, as required by these rules and conduct, I have fully cited and referenced all material and results that are not original to this work.

Name, Last Name: MÜRSEL KARADAŞ

Signature :

ABSTRACT

2D SIMULATIONS BASED ON THE GENERAL TIME DEPENDENT RECIPROCAL RELATION AND INITIAL EXPERIMENTS FOR LFEIT

Mürsel Karadaş,
M.S., Department of Electrical and Electronics Eng.
Supervisor : Prof. Dr. Nevzat Güneri Gençer

September 2014, 105 pages

In this study, the new imaging modality Lorentz Field Electrical Impedance Tomography (LFEIT) is investigated. In LFEIT, the main aim is finding the conductivity distribution of different tissues. This method is based on the development of the current density distribution in the conductive medium. To develop the current density, the object is located in a static magnetic field and pressure wave due to an ultrasonic transducer develops particle movements inside the body. As a result, a velocity current distribution is created in the conductive medium via Lorentz force. An induction coil sensor placed around the body is utilized to measure the change in the magnetic flux density due to the velocity current distribution. To simulate the new technique, multiphysics solution is required which couples acoustic and electromagnetic equations. These equations in the conductive medium are reviewed and the numerical tools such as Finite Element Method (FEM) and Finite Difference Time Domain (FDTD) are used for their solution. To relate the conductive perturbation to the measurement, general time dependence reciprocal relation is used. The continuous forward

problem is linearized and discretized to obtain a linear system of equations. The sensitivity matrix is obtained for different coil configurations and ultrasound transducer positions and its characteristics are analyzed. Thereafter, the image reconstruction algorithms and regularization methods are evaluated by means of the simulation data. The results show that, the imaging system provides high resolution for conductivity perturbation. Moreover, an initial experimental study is given to demonstrate the proof of the concept.

Keywords: Medical Imaging, Electrical Impedance Tomography, Conductivity Imaging, Ultrasound, Lorentz Force, Finite Element Method, Regularization

ÖZ

LFEIT İÇİN GENEL ZAMANA BAĞLI KARŞILIKLILIK İLİŞKİSİ TEMELLİ 2D BENZETİMLER VE BAŞLANGIÇ DENEYLERİ

Mürsel Karadaş,
Yüksek Lisans, Elektrik ve Elektronik Mühendisliği Bölümü
Tez Yöneticisi : Prof. Dr. Nevzat Güneri Gençer

Eylül 2014, 105 sayfa

Bu çalışmada yeni bir görüntüleme yöntemi olan Lorentz Alan Elektriksel Empedans Tomografisi (LAEET) incelenmiştir. LAEET'de temel amaç, farklı dokuların iletkenlik dağılımını elde etmektir. Bu metot iletken bir ortamda akım yoğunluğu dağılımını oluşturmak üzerine kurulmuştur. Akım yoğunluğunu oluşturabilmek için, obje sabit bir manyetik alan içerisine yerleştirilmekte ve ultrasonik dönüştürücü yoluyla oluşturulan basınç dalgası vücut içerisinde parçacık hareketi oluşturmaktadır. Bunun sonucunda, Lorentz kuvveti vasıtası ile iletken ortamda bir hız akım yoğunluğu yaratılmaktadır. Bu hız akımı yoğunluğunun oluşturmuş olduğu manyetik akı yoğunluğundaki değişim, cisim etrafına yerleştirilmiş endüksiyon bobini ile ölçülmektedir. Benzetim çalışmaları yapabilmek için akustik ve elektromagnetik denklemlerin beraber çözülmesi gerekmektedir. İletken ortam için bu denklemler gözden geçirilmiş ve sonlu elemanlar yöntemi (FEM) ve zamanda sonlu farklar yöntemi (FDTD) gibi nümerik araçlar kullanılarak çözümler elde edilmiştir. Ölçümler ve iletkenlik dağılımını ilişkilendirmek

için genel zamana bağlı karşılıklılık ilişkisi kullanılmıştır. Sürekli ileri problem doğrusallaştılıp, ayrıklaştılıp doğrusal denklemler sistemi elde edilmiştir. Farklı bobin konfigürasyonları ve ultrasonik dönüştürücü pozisyonları için duyarlılık matrisi hesaplanıp, matrisin karakteristiği incelenmiştir. Daha sonrasında, farklı geriçatma algoritmaları ve düzenleme metotları benzetim dataları kullanılarak değerlendirilmiştir. Sonuçlar, iletkenlik görüntüleme için görüntüleme sisteminin yüksek çözünürlülük sağladığını göstermektedir. Bunlara ek olarak, kavramın kanıtlanabilirliğini göstermek için başlangıç deneyleri yapılmıştır.

Anahtar Kelimeler: Medikal Görüntüleme, Elektrik Empedans Tomografisi, İletkenlik Görüntüleme, Ultrason, Lorentz Kuvveti, Sonlu Elemanlar Yöntemi, Düzenleme

To my family and friends

ACKNOWLEDGMENTS

I would like to express my sincere appreciation to my supervisor, Prof. Dr. Nevzat Güneri Gençer for his support, invaluable guidance, supervision and friendly encouragement.

I would like to express my deepest gratitude to Azadeh Kamali for not only her invaluable support through my study-journey but especially for make me feeling that there always must be one more season waiting to be discovered through our hands :). I am grateful to Dr. Reyhan Zengin for her precious support, advices, and guidance during my graduate studies; to Dr. Can Barış Top not only for sharing his experiences but also for creating an environment to reach a scientific point of view; to Balkar Erdoğan for his guidance and kindness; to Ulaş Can Inan for his support in the experimental study and to all the members of Brain Research Laboratory.

I would like to thank to a very special group of friends: Dr. Tuğcan Aktaş, Selim Özgen, Pınar Şen, Feylesof Fikret for creating lovely, wonderful times as well as sharing it with me. It was a perfect feeling to know that whatever i need they will provide.

I would like to express my gratitude to Berna Akıncı and Ufuk Suat Aydın for sharing almost one hundred years of solitudeness of BRL and for arousing joyful, valuable times; as well as to Serkan Sarıtaş, Damla Alptekin and to the members of Kardiosis, Venavis, MRIRL and Telecommunication laboratory.

I would like to acknowledge TÜBİTAK for the scholarship they supplied for two years of my study.

Finally, I would like to thank to my family for their endless support during my whole study life. I truly owe my all success to them.

TABLE OF CONTENTS

LIST OF TABLES

TABLES

LIST OF FIGURES

FIGURES

LIST OF ABBREVIATIONS

AET	Acousto-Electrical Tomography
ART	Algebraic Reconstruction Technique
CAV	Component Averaging
CG	Conjugate Gradient
CGLS	Conjugate Gradient Least Squares
EIT	Electrical Impedance Tomography
FDA	Food and Drug Administration
FEM	Finite Element Method
FDM	Finite Difference Method
FDTD	Finite Difference Time Domain
GPRS	Gradient Projection for Sparse Reconstruction
ICEIT	Induced Current Electrical Impedance Tomography
IRLS	Iteratively Reweighted Least Square
I_{SPPA}	Spatial Peak-Pulse Average Intensity
I_{SPTA}	Spatial Peak-Temporal Average Intensity
LFEIT	Lorentz Field Electrical Impedance Tomography
MAET	Magneto-Acoustic-Electrical Tomography
MAT-MI	Magneto-Acoustic Tomography with Magnetic Induction
MI	Mechanical Index
MoM	Method of Moments
MRCDI	Magnetic Resonance Current Density Imaging
MREIT	Magnetic Resonance Electrical Impedance Tomography
MIT	Magentic Induction Tomography
PSD	Positive Semi Definite
RF	Radio Frequency
SEM	Series Expansion Method
SIRT	Simultaneous Iterative Reconstruction Technique
SNR	Signal-to-Noise Ratio
SVD	Singular Value Decomposition
TSVD	Truncated Singular Value Decomposition
TwIST	Two-step Iterative Shrinkage/Thresholding
US	Ultrasound

CHAPTER 1

INTRODUCTION

Statistics show that breast cancer is one of the most common cancer among the women worldwide [3, 4]. Early stage diagnosis of the breast cancer is essential to decrease its mortality rate. In the recent decades, mammography has been used as the general tool for cancerous tissue detection [5, 6]. However, diagnosis based on mammography alone may result in unnecessary biopsies due to its high false positive rates. On the other hand, alternative imaging modalities such as magnetic resonance imaging (MRI), ultrasound and nuclear medicine cannot distinguish the malignant tissue from the benign tissue at most instances [4]. Consequently, there is a need for an efficient method to overcome these limitations. Recently, it was realized that there are differences between the conductivity of the normal and malignant tissues in the low frequency ranges [7].

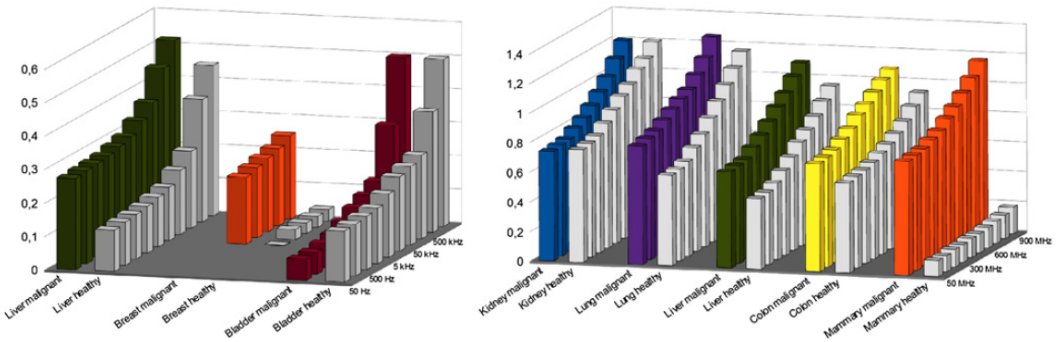

Figure 1.1: Contrast of conductivity in biological tissue [7]

Electrical conductivity is a promising feature to differentiate cancerous tissues. Several electromagnetic methods have been proposed to measure the conductivity of biological tissues. The pioneering approach for conductivity imaging is Electrical Impedance Tomography (EIT) [8–10]. In this approach, the surface electrodes are placed equidistantly around the body and a pair is used for current injection at 50 kHz. Meanwhile, the potential difference is sensed from other electrode pairs. By changing the drive and measurement electrode pairs independent data are acquired and used for image reconstruction. EIT has been used in various clinical applications and continues to attract substantial research interest because of its functional information. However, its spatial resolution is limited.

In induced current electrical impedance tomography (ICEIT), induction method is used instead of applying currents to the body directly [11–13]. A sinusoidal current at 50 kHz is applied to the coil encircling body and time-varying magnetic fields are generated. The resultant voltages due to induced currents are measured by using the surface electrodes, as in applied current EIT.

The injected/induced currents generate magnetic fields. Once these fields are measured inside the body, the conductivity distribution can be reconstructed with a higher resolution. Magnetic Resonance Electrical Impedance Tomography (MREIT) is a method based on the magnetic field measurements due to externally applied currents using an MRI device. In earlier studies, Joy an Scott proposed the measurement of the magnetic flux density due to injected currents using MRI [14–16]. The method is named as magnetic resonance current density imaging (MRCDI), since the measurements are used to form images of the internal current density distribution. Combining MRCDI and EIT methods, MREIT technique was proposed [17, 18]. In this method, the conductivity distribution is obtained utilizing the internal current density reconstructions of MRCDI.

In the late 90's the magnetic induction tomography (MIT) was proposed [19–21]. In MIT, transmitter and receiver coils are placed around the conductive tissue and eddy currents are induced inside the body by applying electrical current to the transmitter coil. Subsequently, secondary magnetic flux density is sensed by

the receiver coils. In this approach, physical contact is not required between the body and the measurement system. In addition, the number of measurements can be increased by shifting the coil array.

The electromagnetic waves have a good penetration depth due to their large wavelength. For imaging purposes, however, they provide lower spatial resolution unless higher frequencies are employed for excitation (lowering the penetration depth). On the other hand, acoustic imaging methods provide higher spatial resolution with reasonable penetration depth. To make use of the high spatial resolution of acoustic imaging techniques, hybrid methods were proposed that may generate images of both electrical and acoustic properties. Acousto-electrical tomography (AET), magneto-acoustic tomography with magnetic induction (MAT-MI), and Magneto-acoustic-electrical tomography (MAET) are the well-known methods which deal with both electrical and acoustic properties.

In MAT-MI, the body is placed inside the static magnetic field and eddy currents are induced by applying secondary time-varying magnetic fields [22–24]. The interaction between the main component of the magnetic field and eddy current causes a Lorentz force on the conductive body. Consequently, an acoustic vibration is developed. The resultant acoustic wave is sensed by an ultrasound transducer placed around the object.

In MAET, the object is located in a static magnetic field and pressure wave due to an ultrasonic transducer develops particle movements inside the body [25–29]. As a result, a current distribution is created in the conductive medium via Lorentz force. The voltage/current is measured using surface electrodes.

AET is based on the localized change in the resistivity which is created by focused ultrasonic waves [30]. In AET, an ultrasound excitation is added to the standard EIT technique. In this method, data is collected similar to the conventional EIT but an ultrasound wave is sent to the object while data is acquired. The volume at focal spot of transducer is imposed by periodic cycles of mechanical compression and rarefaction determined by the ultrasound frequency. Conductivity changes occur only inside the embedded volume, so

spatial encoding can be achieved.

One may conclude that, all acousto-electrical imaging methods have a potential to provide better spatial resolution compared to the EIT method. Resolution in these methods is limited by the axial and lateral beam width of the ultrasound wave. Since bipolar ultrasound waves are applied to the body, integration of the wave is zero in the domain of constant conductivity. Therefore, the signal can be recorded only from the conductivity interfaces.

In 2012, Zengin and Gencer proposed a new hybrid imaging modality called as Lorentz Field Electrical Impedance Tomography (LFEIT) [1]. In this method, a current density distribution is developed in the conductive medium similar to conventional MAET method. In LFEIT, pick-up coils are used for measurement instead of the surface electrodes. The relation between conductivity and the measurement is derived by means of reciprocity theorem. The method is evaluated by solving multiphysic problem (piezoelectric, acoustic, electromagnetic) in COMSOL Multiphysics. Furthermore, the derived relation between the measurement and conductivity distribution is linearized around the initial conductivity distribution and the sensitivity matrix is obtained. The characteristics of the imaging system are studied by analyzing the sensitivity matrix using the singular value decomposition (SVD). Simulation studies are done to analyze the performance of the imaging system.

1.1 Scope of the Thesis

In this thesis, LFEIT method is evaluated in detail to realize the efficiency of this method. In [1], the original problem was analyzed and the first numerical study was done. However, in this study, the inverse problem and reciprocal formulations are discussed to obtain more information about the potential of LFEIT method in finding the conductivity distribution of different tissues. To evaluate the feasibility of the system, the method should be analyzed, experimentally. Therefore, the scope of this thesis can be listed as:

- Finding the general-time dependence reciprocity relation. Since the exci-

tation is not time-harmonic, the fields related to it are not time-harmonic, too. So, the reciprocity relation should be derived for a general-time dependence case.

- Evaluating the electric field distribution for reciprocal problem.
- Conducting the numerical study of forward and reciprocal problems.
- Analyzing the limitations and the feasibility of the method by means of numerical study.
- Performing simulation studies on inverse problem.
- Analyzing the effect of different coil configuration and transducer excitation on performance of the system.
- Preparing an initial experimental setup to evaluate the method, practically.

1.2 Thesis Organization

In Chapter 2, a forward and reciprocal problem formulation is given. In addition, the general-time dependence reciprocity theorem is discussed.

In Chapter 3, the numerical study on the original and reciprocal problem is conducted. To solve the acoustic, electromagnetic problem numerically, a commercial COMSOL Multiphysics, Finite Element Method (FEM) solver, is used. FDTD and FEM simulations are done to verify the results of COMSOL Multiphysics.

In Chapter 4, the problem is linearized and the imaging modality is analyzed using the sensitivity analysis. The effect of coil configuration and pressure wave on the obtained results are discussed. In addition, different regularization methods are compared.

In Chapter 5, LFEIT method is evaluated, experimentally. The initial experimental setup and the received signal are provided.

CHAPTER 2

FORWARD PROBLEM OF LFEIT

2.1 Introduction

The direct *forward problem* of Lorentz Field Electrical Impedance Tomography (LFEIT) is defined as solving the magnetic field distribution due to Lorentz fields given the body geometry and conductivity distribution (Figure 2.1) [1]. The reciprocal problem is defined as finding the electric field distribution due to a reciprocal current in the measurement coil (Figure 2.2]). In this chapter, the theory of the original (direct) forward problem and reciprocal problem are reviewed. A general time-dependent reciprocity relation is derived in Laplace's domain and transformed to time-domain.

2.2 The Original Forward Problem of LFEIT

In LFEIT, measurements are the voltages received from pick-up coils (Figure 2.1). The induced voltage $V_{ind}(t)$ in a receiver coil is expressed as follows:

$$V_{ind}(t) = -\int_S \frac{\partial \vec{B}}{\partial t} \cdot d\vec{S} \tag{2.1}$$

where $\vec{B}$ is the total magnetic flux density, and $d\vec{S}$ denotes the differential surface element on the coil plane. To solve the pick-up voltages, the partial differential equation governing the behavior of flux density must be obtained. By neglecting

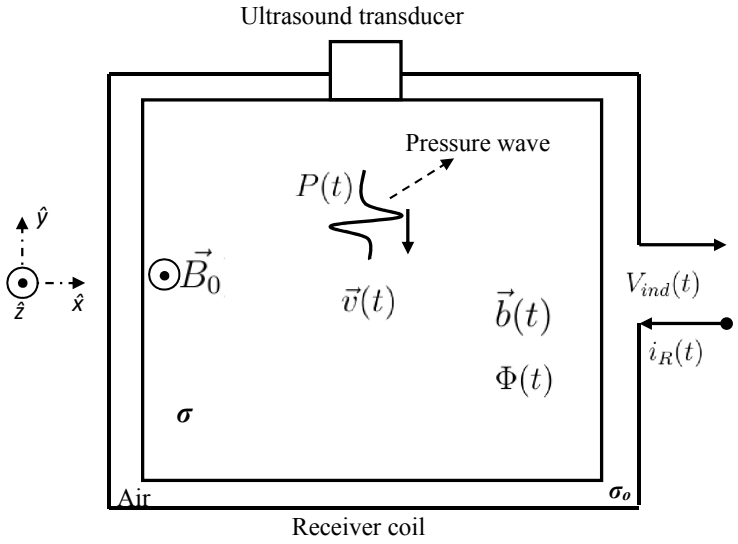

Figure 2.1: Problem geometry of LFEIT. . The particle velocity $\vec{v}(t)$ is developed by an ultrasound transducer. Under the static magnetic field $\vec{B}_0$, the velocity current distribution $\sigma(\vec{v}\times\vec{B})$ is generated in the conductive medium. The change in the magnetic field, $\vec{b}(t)$, is measured using a coil encircling the body or placed close to the body. $P(t)$ and $\Phi(t)$ are ultrasound pressure and scalar potential.

the displacement currents and considering Ampere' law one obtains [1]:

$$\nabla \times \nabla \times \vec{B} = \nabla \times (\mu\sigma(\vec{v} \times \vec{B} - \nabla\Phi)) \tag{2.2}$$

where $\vec{v}$ is the particle velocity due to the ultrasound excitation, $\vec{B}$ is the total magnetic flux density, and Φ is the electric scalar potential. The relation between $\vec{v}$ and the ultrasound excitation was derived in [1]. The total magnetic flux density consists of two components: the static magnetic flux density $\vec{B_0}$, and time-varying magnetic flux density $\vec{b(t)}$. The scalar potential due to the velocity current distribution $\sigma(\vec{v} \times \vec{B})$ is calculated by the following partial differential equation

$$\nabla \cdot \Big(\sigma\nabla\Phi - \sigma(\vec{v} \times \vec{B})\Big) = 0 \tag{2.3}$$

Since $\vec{b}(t)$ is too small compared to the static magnetic field $\vec{B_0}$, and divergence of $\vec{B}$ is zero, 2.2 reduces to

$$\nabla^2\vec{b} = \nabla \times (\mu\sigma(\vec{v} \times \vec{B_0} - \nabla\Phi)) \tag{2.4}$$

Let b_0 represents the magnetic flux density for an initial conductivity distribution of σ_0, then it satisfies the following equation:

$$\nabla^2 \vec{b_0} = \nabla \times (\mu\sigma_0(\vec{v} \times \vec{B_0} - \nabla\Phi_0)) \tag{2.5}$$

When there is a perturbation $\Delta\sigma$ in conductivity, the change in the magnetic flux density Δb is [1].

$$\nabla^2 \Delta\vec{b} = \nabla \times (\mu\Delta\sigma(\vec{v} \times \vec{B_0} - \nabla\Phi)) \tag{2.6}$$

The solution of the time-varying magnetic flux density distribution $b(\vec{t})$ is obtained in two steps. First, the expression in 2.3 is solved to find the scalar potential distribution Φ. In the second step, 2.4-2.6 are considered with the calculated Φ.

2.3 The Reciprocal Problem

The electric field ($\vec{E}$) in a volume conductor consists of two components: 1) the induced field developed by time-varying current flowing in the coil, 2) the field related to the charges accumulating on the conductivity interfaces and on the boundaries of the body. $\vec{E}$ can be expressed as:

$$\vec{E}(t) = -\nabla\Phi(t) - \frac{\partial\vec{A}(t)}{\partial t} \tag{2.7}$$

The term $\frac{\partial\vec{A}(t)}{\partial t}$ is the electric field due to time-varying current in the coil, and $\nabla\Phi(t)$ is the electric field formed by charges accumulated on the boundaries.

To obtain $\vec{A}$ and Φ for an arbitrary time variation, the following coupled partial differential equations should be solved [11]:

$$\nabla^2\vec{A} = \mu_0(\sigma + \frac{\partial}{\partial t}\epsilon)(-\nabla\Phi - \frac{\partial}{\partial t}\vec{A}) \tag{2.8}$$

$$\nabla \cdot \left[(\sigma + \epsilon\frac{\partial}{\partial t})\nabla\Phi\right] = -\nabla(\sigma + \epsilon\frac{\partial}{\partial t}) \cdot \frac{\partial\vec{A}}{\partial t} \tag{2.9}$$

At the interface of the conductor/air, the normal component of total current is zero, so the total electric field is zero. As a result, the boundary condition becomes:

$$\frac{\partial\Phi}{\partial n} = -\frac{\partial\vec{A}}{\partial t} \cdot \vec{n} \tag{2.10}$$

where $\vec{n}$ is the outward unit normal vector.

The problem of finding the electric field $\vec{E}$ is considerably simplified by using the following assumptions : 1) the total magnetic vector potential $\vec{A}$ is approximately equal to the primary magnetic vector potential $\vec{A}_p$ which exists in the absence of conducting body, and 2) the displacement current $(\epsilon\frac{\partial\vec{E}}{\partial t})$ is negligible compared to conduction current $(\sigma\vec{E})$ [11]. Consequently,2.9 and 2.10 reduces to:

$$\nabla \cdot (\sigma \nabla \Phi) = -\nabla\sigma \cdot \frac{\partial \vec{A}_p}{\partial t} \tag{2.11}$$

$$\frac{\partial \Phi}{\partial n} = -\frac{\partial \vec{A}_p}{\partial t} \cdot \vec{n} \tag{2.12}$$

Since the effect of the conduction current is neglected, the primary magnetic vector potential and the electric field $\vec{E_A}$ can be calculated analytically as:

$$\vec{E_A} = -\frac{\partial \vec{A}_p}{\partial t} = -\frac{\mu_0 N}{4\pi}\frac{\partial I}{\partial t}\int\limits_{Coil}\frac{\vec{dl}}{R} \tag{2.13}$$

where

N : the number of turns in the coil,

I : the current flowing in the coil,

$\vec{dl}$: differential element on the coil path,

R : the distance between source and field points

Note that if the initial body conductivity is assumed homogeneous, the problem reduced to the Laplace's equation with the Neumann boundary conditions:

$$\sigma\nabla^2\Phi = 0 \tag{2.14}$$

$$\frac{\partial \Phi}{\partial n} = -\frac{\partial \vec{A}_p}{\partial t} \cdot \vec{n} \tag{2.15}$$

In the case of inhomogeneous conductivity distribution, the continuity conditions should be satisfied on the boundary between conductivity of σ_1 and σ_2.

$$\Phi_1 = \Phi_2 \tag{2.16}$$

$$\sigma_1\vec{n} \cdot \nabla\Phi_1 = \sigma_2\vec{n} \cdot \nabla\Phi_2 \tag{2.17}$$

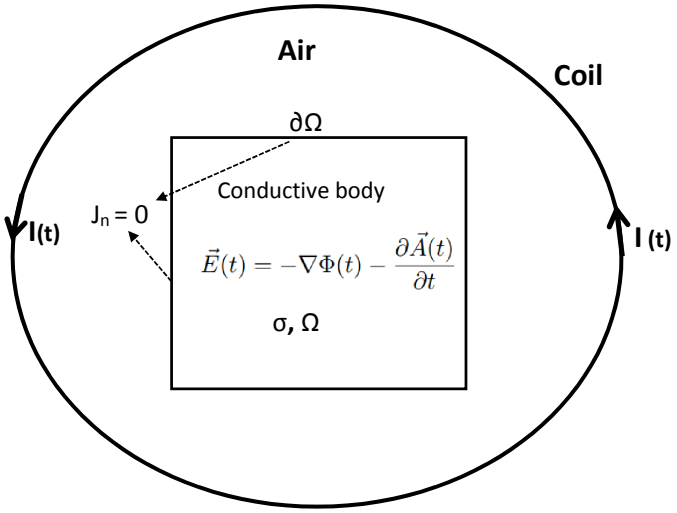

Figure 2.2: Reciprocal problem geometry. The receiver coil encircles the conductive body and carries a time-varying current. The electric field has two main components: $-\frac{\partial\vec{A}(t)}{\partial t}$ and $-\nabla\Phi(t)$

where $\vec{n}$ is the unit normal vector on the boundary, Φ_1 and Φ_2 are scalar potentials in conductor 1 and 2. By considering the electric field due to the magnetic induction, the continuity equation in 2.17 becomes:

$$\sigma_1 \left(\vec{n} \cdot \vec{E_A} - \frac{\partial \Phi_1}{\partial \vec{n}} \right) = \sigma_2 \left(\vec{n} \cdot \vec{E_A} - \frac{\partial \Phi_2}{\partial \vec{n}} \right) \tag{2.18}$$

To sum up, the induced electric field in a volume conductor consist of two component as given in 2.7. The magnetic vector potential component can be calculated analytically by using 2.13. The field component due to the charge accumulation at the boundaries determined by solving the electric scalar potential equations which is given in 2.14 and 2.15. In the case of inhomogeneity, the boundary condition is modified as given in 2.16 - 2.18.

2.4 Reciprocal problem: General time-dependence

Since the total flux density $\vec{B}$ is related to the conductivity distribution in the body, the received voltage is a function of the conductivity distribution. How-

ever, equation 2.1 does not show this relation, explicitly. In this study, reciprocity theorem is used to obtain such a relation.In short, this theorem states that the location of the detector and source can be changed without affecting the detected signal amplitude. Therefore, the detected signal can be expressed in terms of the volume integral of sources inside the body. The sensitivity of the measurement to a specific vector source is determined by the scalar product of a lead-field vector (the electric field generated by a reciprocal unit current in the detector coil) and the selected source. Thus, once the lead field vector is solved for specific detector geometry, the detector voltage for an arbitrary source can be easily calculated by integrating over the source domain. This approach can be applied if the lead field vector for LFEIT can be identified [1]. Since the problem is not simply time-harmonic, the Lorentz reciprocity theorem cannot be used [31]. In this section, the same procedure is considered to derive the relation for the lead field vector.

In the direct and reciprocal problems, the sources are the velocity current density distribution $\vec{j}_V(\vec{r},t)$ and the reciprocal current density distribution $\vec{j}_R(\vec{r},t)$, respectively. In the rest of this derivation, for simplicity, the spatial term is omitted (i.e. $\vec{e}(\vec{r},t) = \vec{e}(t)$).

The Faraday and Ampere Laws for time varying electromagnetic fields in linear, isotropic, non-magnetic medium are:

$$\nabla \times \vec{e}(t) = -\mu \frac{\partial \vec{h}(t)}{\partial t} \tag{2.19}$$

$$\nabla \times \vec{h}(t) = \vec{j}_{source}(t) + \sigma \vec{e}(t) + \epsilon \frac{\partial \vec{e}(t)}{\partial t} \tag{2.20}$$

In the Laplace domain, these two equations can be written:

$$\nabla \times \vec{E}(s) = -\mu s \vec{H}(s) + \vec{h}(0^-) \tag{2.21}$$

$$\nabla \times \vec{H}(s) = \vec{J}_{source}(s) + \sigma \vec{E}(s) + \epsilon s \vec{E}(s) - \epsilon \vec{e}(0^-) \tag{2.22}$$

where $\vec{J}_{source}(s)$ term on the right hand side represents possible current sources in the body (which is normally zero at this frequency range). By using the following vector identity

$$\nabla \cdot (\vec{A} \times \vec{B}) = \vec{B} \cdot (\nabla \times A) - \vec{A} \cdot (\nabla \times B) \tag{2.23}$$

with 2.21 and 2.22 and omitting the initial value of the field terms, the following relation is found:

$$\begin{aligned}\nabla \cdot (\vec{E}_V(s) \times \vec{H}_R(s) - \vec{E}_R(s) \times \vec{H}_V(s)) = &-s\mu\vec{H}_V(s) \cdot \vec{H}_R(s) \\ &-\vec{E}_R(s) \cdot (\vec{J}_V(s) + \sigma\vec{E}_V(s) + s\epsilon\vec{E}_V(s)) \\ &+s\mu\vec{H}_R(s) \cdot \vec{H}_V(s) \\ &+\vec{E}_V(s) \cdot (\vec{J}_R(s) + \sigma\vec{E}_R(s) + s\epsilon\vec{E}_R(s))\end{aligned} \tag{2.24}$$

Equal terms on both sides can be canceled yielding the following final form:

$$\nabla \cdot (\vec{E}_V(s) \times \vec{H}_R(s) - \vec{E}_R(s) \times \vec{H}_V(s)) = \vec{E}_R(s) \cdot \vec{J}_V(s) - \vec{E}_V(s) \cdot \vec{J}_R(s) \tag{2.25}$$

Taking the volume integral of both sides in the whole space (i.e., the bounding surface is at infinity) and applying the divergence theorem to the left side of 2.25, we obtain:

$$\begin{aligned}&\int_{V\infty} \nabla \cdot \left(\vec{E}_V(s) \times \vec{H}_R(s) - \vec{E}_R(s) \times \vec{H}_V(s)\right) dV \\ &= \oint_{S\infty} \left(\vec{E}_V(s) \times \vec{H}_R(s) - \vec{E}_R(s) \times \vec{H}_V(s)\right) \cdot d\vec{S}\end{aligned} \tag{2.26}$$

Since the fields vanishes at infinity, the right hand side of 2.26 becomes zero. Therefore, the following relation holds:

$$\int_V (\vec{E}_R(s) \cdot \vec{J}_V(s) - \vec{E}_V(s) \cdot \vec{J}_R(s))dV = 0 \tag{2.27}$$

$\vec{J}_V$ is nonzero inside the body and $\vec{J}_R$ is nonzero in the receiver coil. Consequently, the integral of 2.27 reduces to:

$$\int_{V_{body}} \vec{E}_R(s) \cdot \vec{J}_V(s)dV = \int_{V_{coil}} \vec{E}_V(s) \cdot \vec{J}_R(s)dV \tag{2.28}$$

Since in the coil domain $\vec{J}_R(s)dV = I_R(s)\vec{dl}$, the left hand side of 2.28 reduces to

$$\int_{V_{body}} \vec{E}_R(s) \cdot \vec{J}_V(s)dV = I_R(s) \int_{coil} \vec{E}_V(s) \cdot \vec{dl} \tag{2.29}$$

The result of the integral at the right side of 2.29 is the induced voltage on the receiver coil. Therefore, the measured voltage on the receiver can be written as:

$$V_{ind}(s) = -\frac{1}{I_R(s)} \int_{V_{body}} \vec{E}_R(s) \cdot \vec{J}_V(s)dV \tag{2.30}$$

The velocity current density $\vec{j_V}(\vec{r},t)$ due to particle velocity in the body $\vec{u}(\vec{r},t)$ in the constant static magnetic field $\vec{B_0}$ is:

$$\vec{j_V}(\vec{r},t) = \sigma(\vec{r})\vec{u}(\vec{r},t) \times \vec{B_0} \tag{2.31}$$

from the equation of the motion, the particle velocity can be written as:

$$\frac{\partial \vec{u}(\vec{r},t)}{\partial t} = -\frac{1}{\rho(\vec{r})}\frac{\partial p(\vec{r},t)}{\partial r} \tag{2.32}$$

where $\rho(\vec{r})$ is mass density of the body, $\vec{p}(\vec{r})$ is the pressure wave that propagates in the body. By using 2.31 and 2.32, the velocity current density in the Laplace domain can be obtained as:

$$\vec{J_V}(\vec{r},s) = -\frac{\sigma(\vec{r})}{s\rho(\vec{r})}(\frac{\partial P(\vec{r},s)}{\partial r} \times \vec{B_0}) \tag{2.33}$$

The current $\vec{I_R}$ flowing can be selected so as its time derivative is constant. Such selection makes the reciprocal electric field $\vec{E_R}$ time independent. A suitable choice for $\vec{i_R}$ is:

$$i_R(t) = ctu(t) \tag{2.34}$$

where c is an arbitrary constant and $u(t)$ is the unit step function. With this selection, i_R is locally integrable on $[0,\infty)$, and thus its Laplace transform exists. The corresponding electric field is then:

$$\vec{e_R}(t) = c\vec{e_R^0}u(t) \tag{2.35}$$

where $\vec{e_R^0}$ is the induced electric field for $i_R(t) = t$ and it is constant in the time-domain.

The electric field and the reciprocal current in Laplace's domain are:

$$\vec{e_R}(s) = \frac{c\vec{e_R^0}}{s} \tag{2.36}$$

$$i_R(s) = \frac{c}{s^2} \tag{2.37}$$

By placing 2.33, 2.36 and 2.37 to 2.30, the induced voltage on the coil can be written as:

$$V_{ind}(s) = \int_{V_{body}} \left(\vec{e_R^0}(\vec{r}) \cdot \frac{\sigma(\vec{r})}{\rho(\vec{r})}(\frac{\partial P(\vec{r},s)}{\partial r} \times \vec{B_0}) \right) dV \tag{2.38}$$

Taking the inverse Laplace transform of both sides, the induced voltage in the time domain can be expressed as:

$$V_{ind}(t) = \int_{V_{body}} \left(\vec{e}_R^0(\vec{r}) \cdot \left(\sigma(\vec{r}) \frac{1}{\rho(\vec{r})} \left(\frac{\partial p(\vec{r}, t)}{\partial r} \times \vec{B}_0 \right) \right) \right) dV \tag{2.39}$$

As given in 2.39, the relation between conductivity and the measurement depends on the reciprocal electric field $\vec{e}_R^0$ and the particle acceleration term $\vec{a}(\vec{r}, t) = \frac{1}{\rho(\vec{r})} \left(\frac{\partial p(\vec{r}, t)}{\partial r} \times \vec{B}_0 \right)$.

CHAPTER 3

NUMERICAL STUDY OF LFEIT

3.1 Introduction

In the most complex engineering problems, numerical methods are used to simplify the analysis. In this study, the model has irregular shape or inhomogeneity, and the problem does not have an analytical solution. Therefore, numerical methods are required to obtain realistic solutions. Generally, four types of numerical methods are used for this purpose: Method of Moments (MoM), Finite Element Methods (FEM), Finite Difference Time Domain Methods (FDTD), and the Finite Difference Method (FDM). In this thesis, FEM algorithm is implemented to have the realistic simulations because of the following reasons: 1) the quality of an approximation between grid points is high; 2) inhomogeneous media can be inserted into the simulations; 3) irregular shapes can be modeled easily; 4) commercial softwares are available.

The forward problem of the LFEIT method is a multiphysics problem. It contains a combination of acoustic, mechanical, and the electromagnetic problems. The block diagram of the simulation strategy is shown in Figure 3.1. To solve the forward problem, a commercial software COMSOL Multyphysics is used based on the FEM algorithm [32]. In this software, the user can define the problem geometry, mesh, and also select the special physics modules.

In the mechanical part of the problem, stress-charge equations are solved. An electrical potential difference is given as an input to a piezo-electric module. The

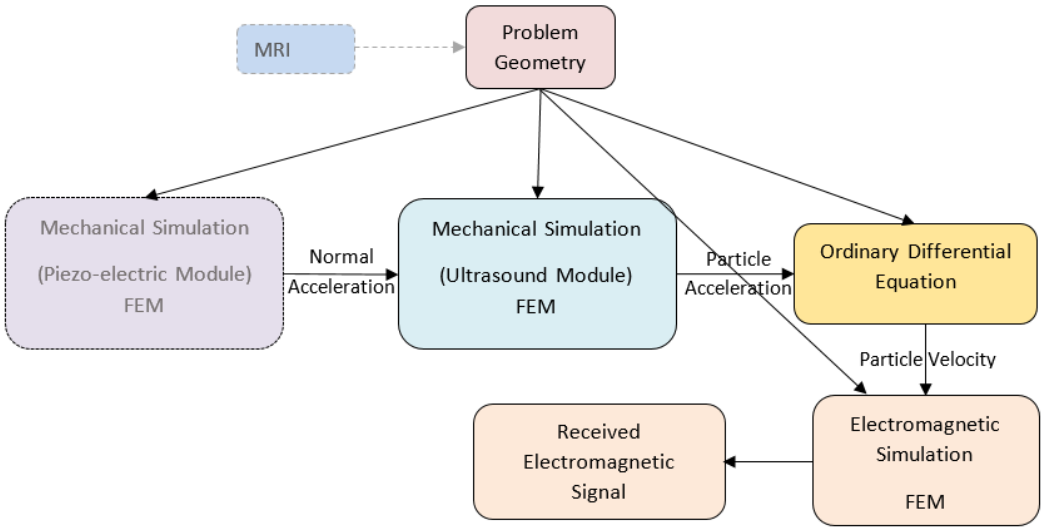

Figure 3.1: Block diagram of the forward problem simulations in LFEIT

displacement is obtained and its second order time derivative is given to the ultrasound simulation section as an input. In the second part, acoustic pressure distribution is calculated.

In the electromagnetic part, the source is the velocity current distribution. Therefore, the particle velocity term obtained from the ultrasound simulation is used as an input of the electromagnetic module. In a second mechanical simulation, the particle acceleration is also obtained. To calculate the particle velocity, an ordinary differential equation solver is implemented.The received signal is determined from the equations given in a previous study [1].

Figure 3.2 shows methodology applied for analyzing the reciprocal problem. The aim is to calculate the total electric field distribution. To achieve this, the Poisson's equation is solved using the FEM method. The input is the magnetic vector potential which can be calculated analytically to ease the calculation.

In this chapter, each step of the forward problem is described and the results using COMSOL Multiphysics are provided. The reciprocal problem is evaluated and the solution is validated by the series expansion method and results of COMSOL Multiphysics.

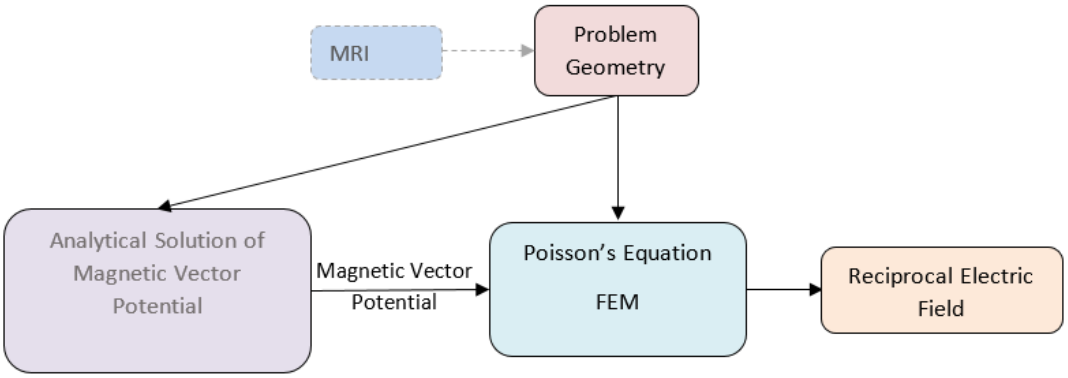

Figure 3.2: Reciprocal Problem Methodology for LFEIT Method.

3.2 Mechanical Simulations

3.2.1 Piezo-electric Module

Certain materials generate an electric charge when they are subjected to the mechanical stress. In addition, their dimensions change when an electric field is applied. These phenomenons are known as the direct and the inverse piezoelectric effects, respectively [33]. They can only occur in anisotropic materials [34].

The relation between mechanical and electrical effects in these materials is expressed by Stress-Charge and Strain-Charge equations:

$$D = \mathbf{e}S + \epsilon^S E \tag{3.1a}$$

$$T = \mathbf{c}^E S - \mathbf{e}^t E \tag{3.1b}$$

$$D = \mathbf{d}T + \epsilon^T E \tag{3.1c}$$

$$S = \mathbf{s}^E T + \mathbf{d}^t E \tag{3.1d}$$

where E, D, S, T denote electric field, displacement field, strain and stress variables, respectively. ϵ, $\mathbf{s}$, $\mathbf{c}$ are permittivity, compliance, and stiffness matrices. The superscripts S, T, and E indicate zero or constant strain, stress and electric field. The relation in 3.1a and 3.1c describe the direct piezoelectric effect, and the others describe an inverse piezoelectric effect of the material.

Equations in 3.1 contain 63 independent variables. However, this number can

be significantly decreased by taking account the symmetry in the PZT material. The poling process will turn the material into a transversely isotropic material with a rotational symmetry around the direction of polarization [35]. Therefore, the number of independent variables are decreased to 10. In this case, the stress-charge equation will be in the form of:

$$\begin{bmatrix} T_1 \\ T_2 \\ T_3 \\ T_4 \\ T_5 \\ T_6 \end{bmatrix} = \begin{bmatrix} c_{11}^E & c_{12}^E & c_{13}^E & 0 & 0 & 0 \\ c_{12}^E & c_{11}^E & c_{13}^E & 0 & 0 & 0 \\ c_{13}^E & c_{13}^E & c_{33}^E & 0 & 0 & 0 \\ 0 & 0 & 0 & c_{44}^E & 0 & 0 \\ 0 & 0 & 0 & 0 & c_{44}^E & 0 \\ 0 & 0 & 0 & 0 & 0 & \frac{1}{2}(c_{11}^E - c_{12}^E) \end{bmatrix} \begin{bmatrix} S_1 \\ S_2 \\ S_3 \\ S_4 \\ S_5 \\ S_6 \end{bmatrix} - \begin{bmatrix} 0 & 0 & e_{13} \\ 0 & 0 & e_{13} \\ 0 & 0 & e_{33} \\ 0 & e_{15} & 0 \\ e_{15} & 0 & 0 \\ 0 & 0 & 0 \end{bmatrix} \begin{bmatrix} E_1 \\ E_2 \\ E_3 \end{bmatrix} \tag{3.2}$$

$$\begin{bmatrix} D_1 \\ D_2 \\ D_3 \end{bmatrix} = \begin{bmatrix} 0 & 0 & 0 & 0 & e_{15} & 0 \\ 0 & 0 & 0 & e_{15} & 0 & 0 \\ e_{31} & e_{31} & e_{33} & 0 & 0 & 0 \end{bmatrix} \begin{bmatrix} S_1 \\ S_2 \\ S_3 \\ S_4 \\ S_5 \\ S_6 \end{bmatrix} - \begin{bmatrix} \epsilon_{11}^S & 0 & 0 \\ 0 & \epsilon_{11}^S & 0 \\ 0 & 0 & \epsilon_{33}^S \end{bmatrix} \begin{bmatrix} E_1 \\ E_2 \\ E_3 \end{bmatrix} \tag{3.3}$$

In this thesis study, a well-known ferroelectric material PZT-5H is used to model the ultrasound transducer. The properties of PZT-5H in the material library of COMSOL software are given below [32]:

$$c^E = \begin{bmatrix} 127 & 80.2 & 84.7 & 0 & 0 & 0 \\ 80.2 & 127 & 84.7 & 0 & 0 & 0 \\ 84.7 & 84.7 & 117 & 0 & 0 & 0 \\ 0 & 0 & 0 & 23 & 0 & 0 \\ 0 & 0 & 0 & 0 & 23 & 0 \\ 0 & 0 & 0 & 0 & 0 & 23.5 \end{bmatrix} GPa$$

$$\epsilon = \begin{bmatrix} 2.7713 & 0 & 0 \\ 0 & 2.7713 & 0 \\ 0 & 0 & 3.0104 \end{bmatrix} \times 10^{-8} F/m$$

$$e = \begin{bmatrix} 0 & 0 & 0 & 0 & 17.035 & 0 \\ 0 & 0 & 0 & 17.035 & 0 & 0 \\ -6.228 & -6.228 & -23.240 & 0 & 0 & 0 \end{bmatrix} C/m^2$$

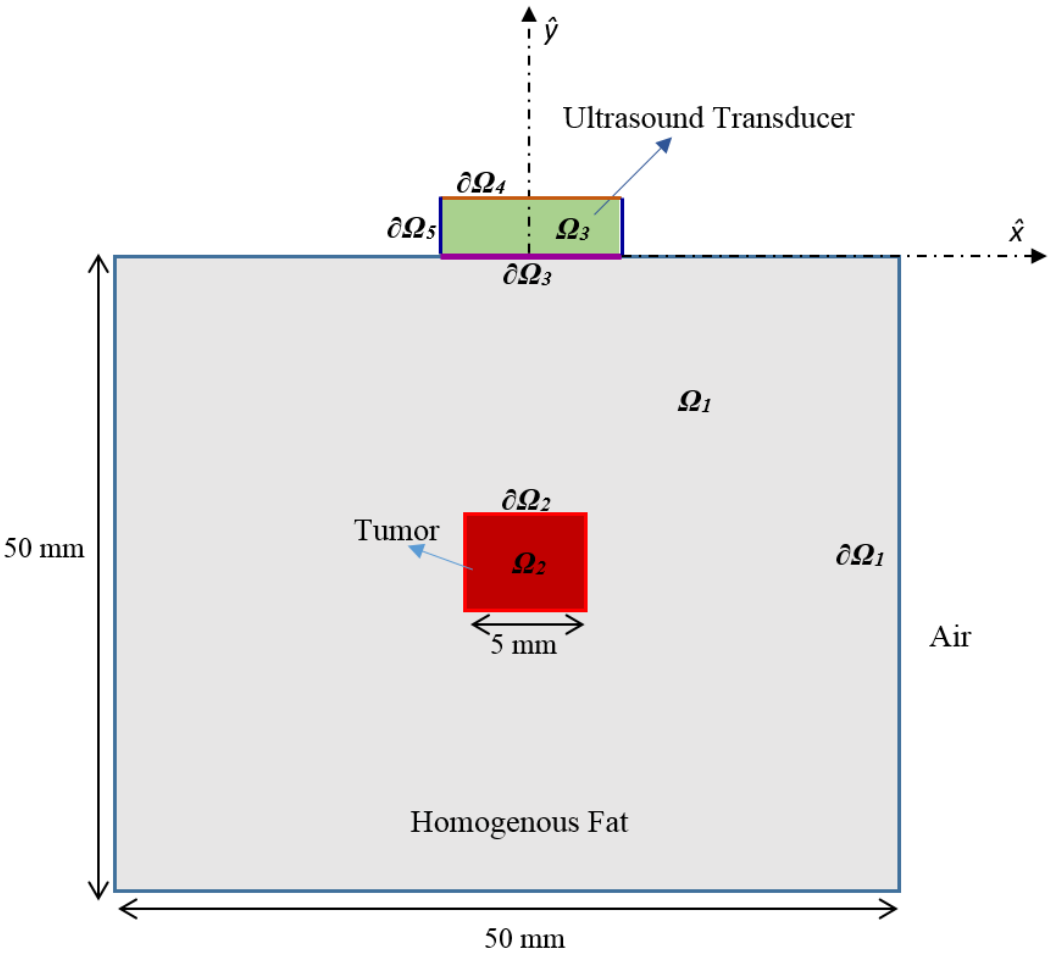

Figure 3.3: Geometry of mechanical simulations. The sub-domains Ω_1 and Ω_2 represent homogeneous fat and tumor tissues. $\partial\Omega_1$ and $\partial\Omega_2$ are the boundaries of homogeneous fat tissue with tumor and air. $\partial\Omega_3$ is the interface between the tissue and the transducer.

The mechanical module of the problem is shown in Figure 3.3. The body volume

of the piezoelectric transducer is Ω_3 and its boundaries are $\partial\Omega_3$, $\partial\Omega_4$, and $\partial\Omega_5$. The electro-mechanical behavior of the transducer is governed by the following partial differential equations:

The electrostatic partial differential equation:

$$\nabla \cdot \vec{D} = q_v \text{ in } \Omega_3 \tag{3.4}$$

subject to the boundary condition:

$$\vec{n} \cdot \vec{D} = -q_s \text{ on } \partial\Omega_3, \ \partial\Omega_4 \text{ and } \partial\Omega_5 \tag{3.5}$$

The mechanical system is defined by:

$$\nabla \cdot \vec{T} = \rho \frac{\partial^2 \vec{u}}{\partial t^2} \text{ in } \Omega_3 \tag{3.6}$$

subject to the boundary condition:

$$\vec{n} \cdot \vec{T} = t \text{ on } \partial\Omega_3, \ \partial\Omega_4 \text{ and } \partial\Omega_5 \tag{3.7}$$

where q_v, n, q_s, ρ, t, and $\vec{u}$ are volume charge, outward normal of boundary surface charge, mass density, traction vector, and the mechanical displacement vector, respectively. The stress-charge constitutive equation is given in 3.1a and 3.1b. The electric field and the strain component can be written in terms of the mechanical displacement and the electric field scalar potential as:

$$S_{ij} = \frac{1}{2}\left[\frac{\partial u_i}{\partial x_j} + \frac{\partial u_j}{\partial x_i}\right] \tag{3.8}$$

$$\vec{E} = -\nabla\Phi \tag{3.9}$$

3.2.2 Acoustic Module

In the LFEIT method, the acoustic pressure distribution should be modeled to obtain the velocity current density inside the body. In Figure 3.3, the body is modeled as a homogeneous fat containing a small tumor. The partial differential equation governing the behavior of pressure distribution in the body is:

$$\frac{\partial P(r,t)}{\partial t} = -\rho c_s^2 \nabla \cdot \vec{v}(r,t) \tag{3.10}$$

$$\frac{\partial \vec{v}(r,t)}{\partial t} = -\frac{1}{\rho}\nabla P(r,t) \tag{3.11}$$

where P is the pressure, ρ is the mass density, c_s is the speed of sound, and $\vec{v}$ is the particle velocity vector. The partial differential equation of the pressure distribution can be derived by rearranging the divergence of 3.11 and the temporal derivative of 3.10.

$$\nabla^2 P(r,t) = \frac{1}{c_s^2}\frac{\partial^2 P(r,t)}{\partial t^2} \tag{3.12}$$

Two different boundary conditions, namely, the normal acceleration and the continuity equations are:

$$\vec{n}\cdot\frac{\partial \vec{v}(r,t)}{\partial t} = -\vec{n}\cdot\frac{1}{\rho}\nabla P(r,t) = a_n \text{ on } \partial\Omega_3 \tag{3.13}$$

$$\vec{n}\cdot(\frac{\partial \vec{v_1}(r,t)}{\partial t} - \frac{\partial \vec{v_2}(r,t)}{\partial t}) = -\vec{n}\cdot\left((\frac{1}{\rho}\nabla P(r,t))_1 - (\frac{1}{\rho}\nabla P(r,t))_2\right) = 0 \text{ on } \partial\Omega_1 \text{ and } \partial\Omega_2 \tag{3.14}$$

The particle velocity is an input of the electromagnetic simulation, and the particle accelaration is the component of a function 2.39. These variables can be calculated numerically using FDTD and equations provided in 3.10 and 3.11 or utilizing FEM and 3.12 equation.

3.2.2.1 FDTD Formulation

FDTD algorithm of the acoustic pressure is developed by discretizing the pressure and velocity components in both time and spatial domains. 2D arrangement of the nodes is shown in Figure 3.4.To obtain the update equations, the discrete form of 3.10 and 3.11 can be written as follows:

$$P_{i,j}^{n+1} = P_{i,j}^{n} - \rho c_s^2 \frac{\Delta t}{\Delta x}(v_{x_{i+1,j}}^{n+1/2} - v_{x_{i,j}}^{n+1/2}) - \rho c_s^2 \frac{\Delta t}{\Delta y}(v_{y_{i,j+1}}^{n+1/2} - v_{y_{i,j}}^{n+1/2}) \tag{3.15}$$

$$v_{x_{i,j}}^{n+1/2} = v_{x_{i,j}}^{n-1/2} - \frac{\Delta t}{\rho \Delta x}(P_{i+1,j}^{n} - P_{i,j}^{n}) \tag{3.16}$$

$$v_{y_{i,j}}^{n+1/2} = v_{y_{i,j}}^{n-1/2} - \frac{\Delta t}{\rho \Delta y}(P_{i,j+1}^{n} - P_{i,j}^{n}) \tag{3.17}$$

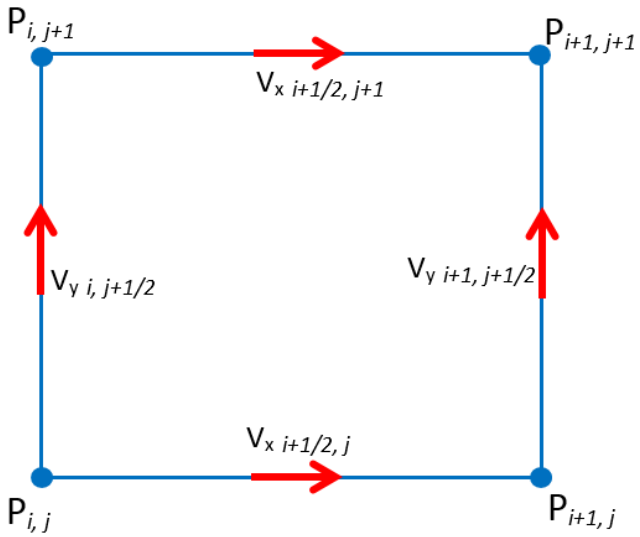

Figure 3.4: Location of the pressure and velocity fields in the unit cell.

3.2.2.2 FEM Formulation

In the FEM formulation, the pressure wave is modeled as a scalar wave equation propagation in the spatial domain (Figure 3.3). It is modeled in the temporal domain with the final time instance T.

$$\begin{aligned} \nabla^2 P &= \frac{1}{c_s^2}\frac{\partial^2 P}{\partial t^2} \quad \text{in} \quad (\Omega_1 \cup \Omega_2) \times (0,T) \\ P(:,0) = 0 \quad &\text{and} \quad \frac{\partial P}{\partial t}(:,0) = 0 \quad \text{in} \quad (\Omega_1 \cup \Omega_2) \\ -\vec{n} \cdot \left((\frac{1}{\rho}\nabla P)_1 - (\frac{1}{\rho}\nabla P)_2 \right) &= \begin{cases} a_n & \text{on } \partial\Omega_3 \times (0,T) \\ 0, & \text{on } (\partial\Omega_1 \cup \partial\Omega_2) \times (0,T) \end{cases} \end{aligned} \tag{3.18}$$

The spatial space is divided into N domains and the temporal space is divided into M domains. If the basis functions are selected such that their space W^P satisfies 3.18, the acoustic pressure solution can be written in terms of these basis functions [36]:

$$P(x,t) = \sum_{i=0}^{N}\sum_{n=1}^{M} P_i^n \varphi_i(x)\psi_n(t) \tag{3.19}$$

where $\varphi_i(x)$ and $\psi_n(t)$ are the continuous linear functions in the space and time, respectively.

To derive the variational form of the acoustic pressure equation, the 3.19 is substituted into 3.18. Then, it is multiplied with test function $v(x,t)$ [36]. Finally, it is integrated on Ω. If the test functions are selected as $v(x,t) = \varphi_j(x)\psi_m(t)$, the final form will be:

$$
\begin{aligned}
-\sum_{i=0}^{N}\sum_{n=1}^{M} P_i^n \int_{\Omega} \frac{1}{c_s^2}\varphi_i(x)\varphi_j(x) \int_{t_{n-1}}^{t_{n+1}} \frac{\partial \psi_n(t)}{\partial t}\frac{\partial \psi_m(x,t)}{\partial t} dxdt \\
+\sum_{i=0}^{N}\sum_{n=1}^{M} P_i^n \int_{\Omega} \nabla\varphi_i(x)\cdot\nabla\varphi_j(x) \int_{t_{n-1}}^{t_{n+1}} \psi_n(t)\psi_m(t) dxdt \\
= \sum_{i=0}^{N}\sum_{n=1}^{M} P_i^n \oint_{\partial\Omega} \int_{t_{n-1}}^{t_{n+1}} a_n(x,t)\varphi_i(x)\psi_n(t) dxdt
\end{aligned}
\tag{3.20}
$$

where P_i^n denotes the unknown coefficient of the basis functions to be determined from 3.20. t_n's are the time steps.

3.2.2.3 FDTD and FEM Results

In FDTD simulations, the inward acceleration a_n is applied to the transducer/tissue interface. In order to model the 16 elements phased-array transducer, the interface is divided into 16 regions with element length and spacing of l and d, respectively. The air/tissue interface and the boundaries where $a_n = 0$ is modeled as sound-hard boundary (i.e. $\frac{\partial P}{\partial n} = 0$). The FEM simulation is made using COMSOL Multiphysics. To validate the results of COMSOL Multiphysics, the same model with the same boundary conditions is simulated in FDTD. The parameters of simulations are given in Table-3.1

In the conventional ultrasound transducer the pressure wave is unimodal (i.e. net momentum is zero). Therefore, a unimodal inward acceleration should be introduced to the interface of the transducer/tissue. The following function is an appropriate choice for 1 MHz transducer excitation to generate a unimodal

Table3.1: Parameters of the Acoustic Simulations

Solver type	FDTD	FEM (COMSOL)
Element number	16	16
Element length (mm)	1	1
Element spacing (mm)	1.5	1.5
Frequency (MHz)	1	1
Maximum element size (mm)	0.1	0.15
Number of elements	250000	326428
Speed of sound (m/s)	1520	1520
mass density (kg/m^3)	1000	1000
Time-step (μs)	0.04	0.1

pressure wave:

$$a_n(t) = Ce^{-\frac{1}{2}(ft-2.5)^2}\cos(2\pi f(t-2.5/f)) \tag{3.21}$$

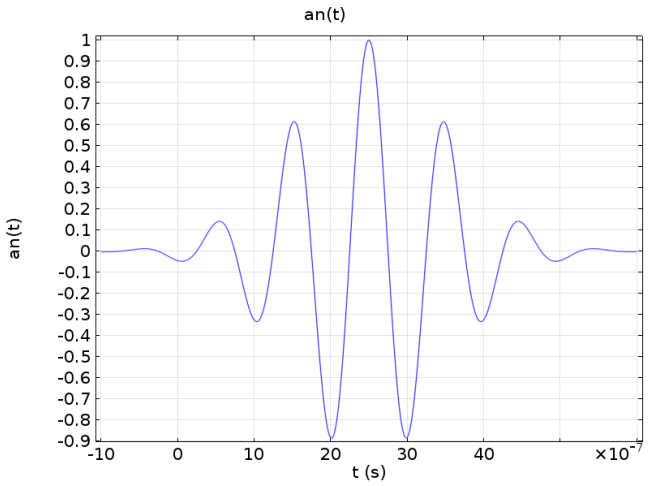

Figure 3.5: Inward accelaration for 1 Mhz unimodal pressure distribution

The simulation results of both methods are shown in Figure 3.6. Instead of continuity boundary condition, the hard wall condition (normal component of the acceleration is zero) is implemented. The FDTD method is employed to justify the results of COMSOL FEM formulations. Under the same conditions, with unimodal inward acceleration excitation, the pressure distributions are given in 3.6-a and 3.6-b. The y-component of the particle accelerations are given in 3.6-c

and 3.6-d. Even though there is a small scale difference between the FDTD and FEM results, the field distributions fields are in a good agreement with each other.

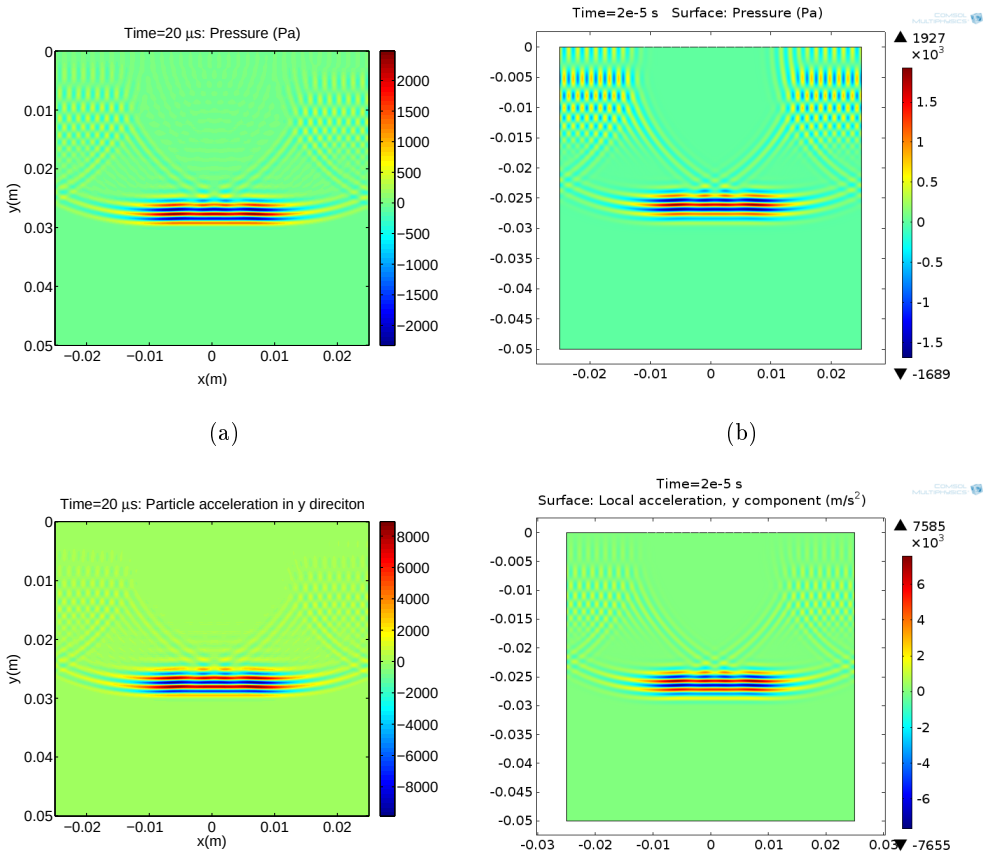

(a) (b)

(c) (d)

Figure 3.6: Comparing the results of two numerical approaches for unimodal inward acceleration excitation. (a) pressure distribution at $t = 20\mu$s (FDTD), (b) pressure distribution at $t = 20\mu$s (COMSOL FEM), (c) y-component of the particle acceleration at $t = 20\mu$s (FDTD), (d) y-component of the particle acceleration at $t = 20\mu$s (COMSOL FEM).

3.3 Electromagnetic Module

In the electromagnetic module, the induced voltage in the receiver coil is calculated. The source of this voltage is the velocity current distribution. In this model, the body is assumed to be in a static magnetic field oriented in the z-direction and the ultrasound excitation is in the xy plane. In the existence of the magnetic field, the movement of the conductive particle generates a current distribution inside the body. The induced voltage depends on the time-derivative of the magnetic flux, so the magnetic flux density should be solved.

To obtain the partial differential equation related to the magnetic flux density, Ampere' law is considered while neglecting the displacement currents.

$$\nabla \times \vec{B} = \mu(\vec{J_s} + \sigma\vec{E}) \tag{3.22}$$

where $\vec{J_s}$ is the source current distribution and $\vec{B}$ is the total magnetic field. They can be defined as:

$$\vec{J_s} = \sigma\vec{v} \times \vec{B} \tag{3.23}$$

$$\vec{B} = B_0\hat{a}_z + \vec{b} \tag{3.24}$$

Here B_0 is the static field and b denotes the magnetic flux density due to Lorentz fields. Since the divergence of the magnetic field is zero and $\|B_0\| \gg \|\vec{b}\|$, the expression 3.22 can be simplified to:

$$\nabla \times \vec{b} = \mu(-\sigma v_x B_0\hat{a}_y + \sigma v_y B_0\hat{a}_x) + \mu\sigma\vec{E} \tag{3.25}$$

where v_x and v_y denote the x- and y- components of the velocity vector $\mathbf{v}$, respectively. Since the sources exist only in the x- and y- directions, the magnetic field has only z component. The electric field can written in terms of the magnetic vector potential A, and electric scalar potential Φ as:

$$\vec{E} = -\frac{\partial\vec{A}}{\partial t} - \nabla\Phi \tag{3.26}$$

If the gauge of $\nabla\Phi = 0$ is assumed and the magnetic flux density $\vec{b}$ is written as $\vec{b} = \nabla \times \vec{A}$, the expression 3.25 is simplified to

$$\nabla \times \nabla \times \vec{A} + \sigma\frac{\partial\vec{A}}{\partial t} = \mu(-\sigma v_x B_0\hat{a}_y + \sigma v_y B_0\hat{a}_x) \tag{3.27}$$

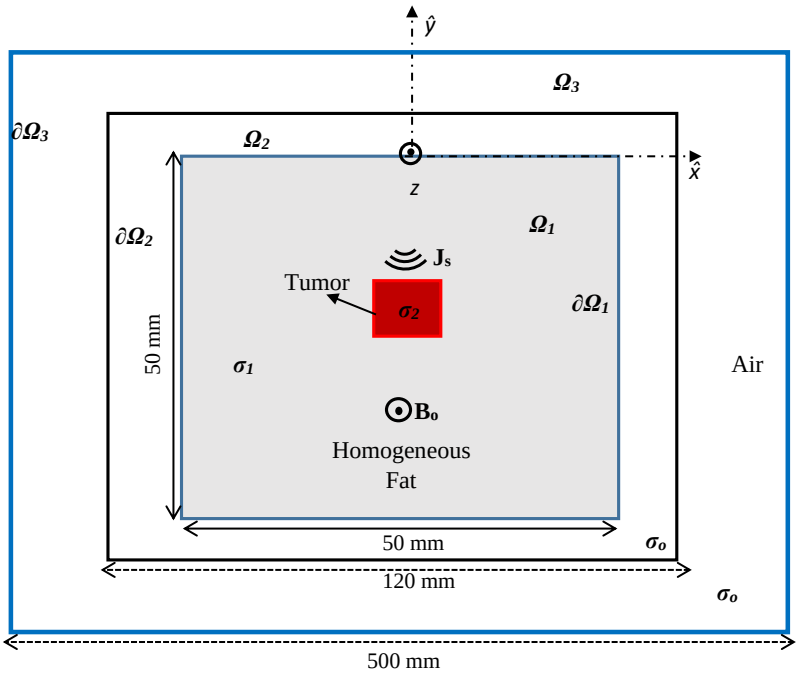

Figure 3.7: Simulation model for the electromagnetic module.

3.3.1 Results

The simulation model for electromagnetic module is illustrated in Figure 3.7. The homogeneous fat is modelled with uniform conductivity of 0.2 S/m. A 5x5 mm rectangular tissue is placed at the centre of the fat region to represent the tumour. The conductivity of the tumour is selected as 0.82 S/m. The ultrasound excitation is applied from the top side of the model. 16- element phased array transducer at 1 MHz is used. x and y component of the velocity current distribution and the magnetic flux density at $t = 8\mu s$ is given in Figure 3.8-a,c,e. It is observed that, the magnetic flux density is mainly due to x component of the current density and it is very weak. The pressure wave at this time instant is in the fat region and it generates sinusoidal current density distribution of one cycle. The fields of positive and negative cycles cancel each other, thus the net flux density is low. In Figure 3.8-b,d,f, same variables are illustrated at $t = 16\mu s$. In this case, the net flux density is high. In contrast to the previous time instant, the negative and positive cycles of the pressure

wave are in the different conductive region. Consequently, the net flux density becomes non-zero and the resultant field strength gets high.

3.4 Reciprocal Problem

According to the reciprocal problem formulation (chapter 2), two different simulation models were proposed (as shown in Fig.3.9). In these models the volume conductor is modelled as 5x5 cm rectangle with conductivity of $\sigma = 0.2$ S/m. As shown in Fig.3.9-b, the domain is divided into $(99 \times 2) \times (99 \times 2)$ triangle meshes. In the first model, a square coil with side length of 20 cm is placed 0.5 cm away from the conductor. The current flows in the x-direction. In the second model, a square encircling coil with side length of 12 cm is considered. In both cases, the current flowing in the coil is $\frac{\partial I}{\partial t} = 1A/s$. The electric field component of the magnetic vector potential is calculated analytically by using Eq.2.13. To solve the scalar potential field distribution, the FEM is used. To calculate field for a inhomogeneous body, a rectangle with side length of 5 mm is placed in the middle of the volume conductor.

3.4.1 Finite Element Method Formulation

To find scalar potential Φ by using finite element method, the following differential equation with the boundary condition is examined [37]:

$$\nabla \cdot (\sigma \nabla \Phi) = 0 \text{ in } \Omega \tag{3.28}$$

$$\vec{n} \cdot (\sigma \nabla \Phi) = g \text{ on } \partial\Omega \tag{3.29}$$

where Ω is a conductive domain and $\vec{n}$ is the outward unit normal. In our problem, the source term $g$on the right hand side of the boundary condition is $g = -\frac{\partial \vec{A}_p}{\partial t} \cdot \vec{n}$. If u is a solution of the given differential equation, multiplying (3.28) with a test function v and integrating on Ω gives:

$$\int_{\Omega} \nabla \cdot (c \nabla u) v dS = 0 \tag{3.30}$$

Using integration by parts and applying the Green's theorem yields:

$$\int_{\Omega} (c \nabla u) \cdot \nabla v \; dS = \int_{\partial\Omega} \vec{n} \cdot (c \nabla u) v \; d\Gamma \tag{3.31}$$

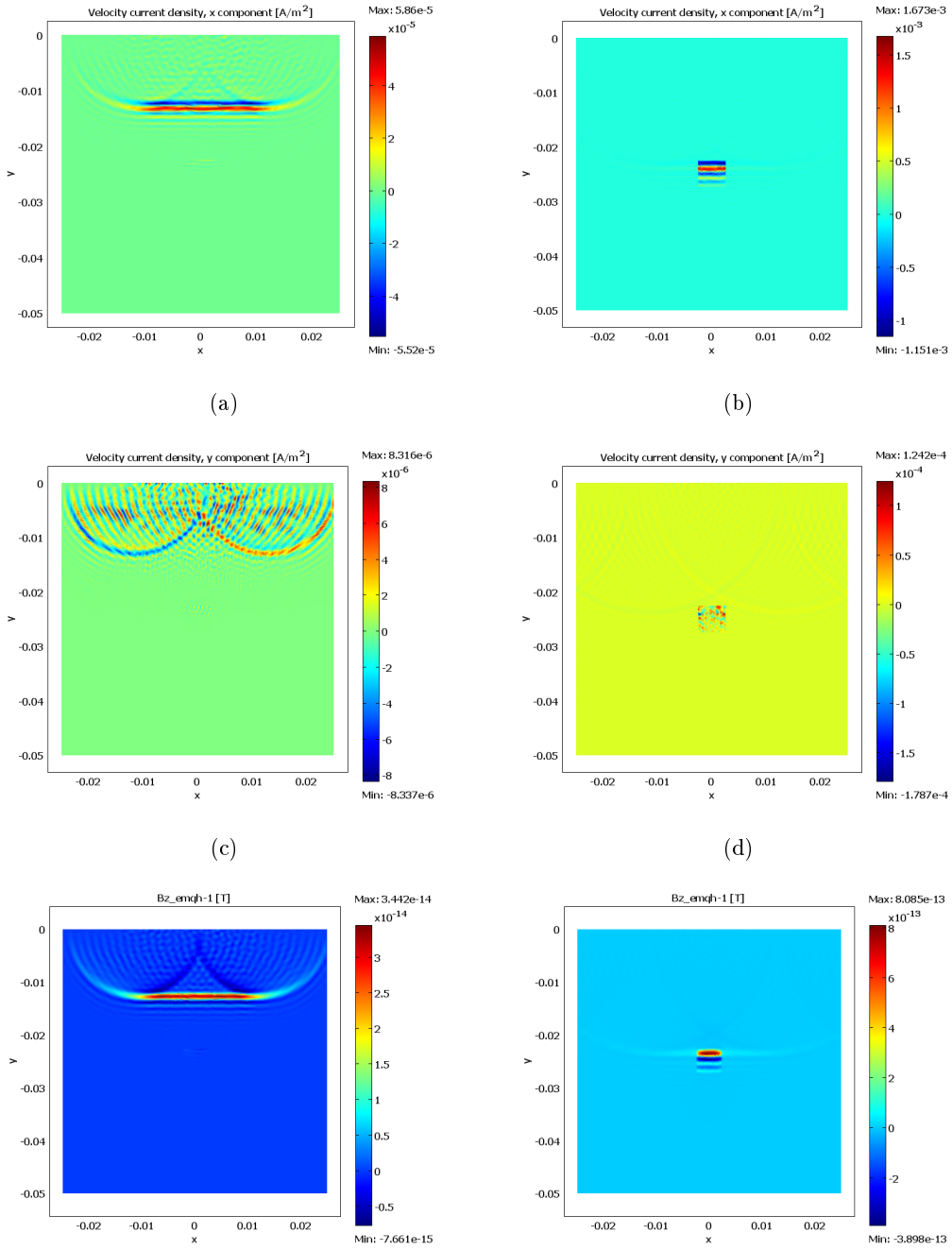

Figure 3.8: The velocity current density components and magnetic flux density distribution at different time instants. The figures on the left shows x- and y-components of the velocity density, and magnetic flux density at $t = 8\mu s$. The figures on the right shows x- and y-components of the velocity density, and magnetic flux density at $t = 16\mu s$.

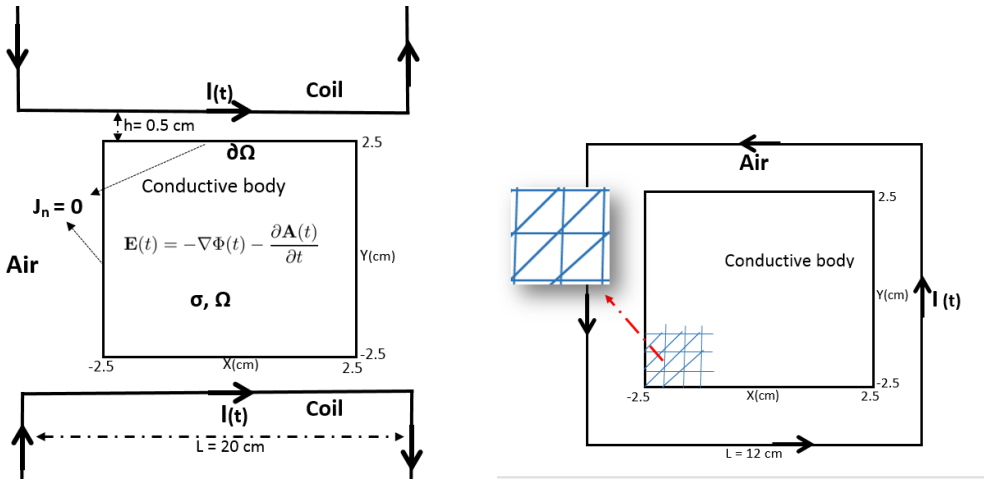

(a) (b)

Figure 3.9: Simulation models for two coil configurations. (a) Two symmetric coils (b) Encircling coil

Replacing the boundary integration with the boundary condition in Eq.(3.29) results:

$$\int_{\Omega} (c\nabla u) \cdot \nabla v \; dS = \int_{\partial\Omega} gv \; d\Gamma \tag{3.32}$$

Instead of solving the original problem given in Eq.(3.28-3.29), u is solved such that it satisfies the variational form:

$$\int_{\Omega} (c\nabla u) \cdot \nabla v \; dS = \int_{\partial\Omega} gv \; d\Gamma \; , \; \forall v \tag{3.33}$$

The solution u and the test function v belong to the function space V. If an N_p dimensional space is selected such that $V_{Np} \subset V$, the solution of the finite dimensional problem will be an element of V_{Np}. In addition, it converges if V_{Np} tends to V as $N_p \to \infty$. Therefore, if test functions are selected as $\alpha_i \; \epsilon \; V_{Np}$, the variational problem is:

$$\int_{\Omega} (c\nabla u) \cdot \nabla \alpha_i \; dS = \int_{\partial\Omega} g\alpha_i \; d\Gamma \; , \; i = 1, 2, 3, ..., N_p \tag{3.34}$$

By expanding u using the basis of V_{Np}

$$u = \sum_{j=1}^{N_p} \phi_j \alpha_j \tag{3.35}$$

a linear system of equation can be obtained from

$$\sum_{j=1}^{N_p} \phi_j \left(\int_{\Omega} (c\nabla\alpha_j) \cdot \nabla\alpha_i \, dS \right) = \int_{\partial\Omega} g\alpha_i \, d\Gamma \ , \ i = 1, 2, 3, ..., N_p \tag{3.36}$$

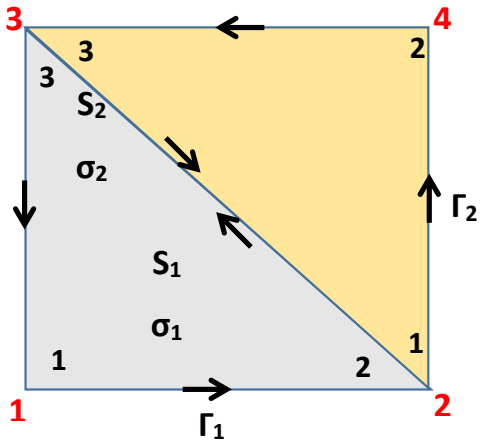

Figure 3.10: A model mesh with 2 triangular elements. The numbers inside the elements represent the local nodes whereas the outside numbers are the global node numbers. S_1, S_2 and σ_1,σ_2 are the element areas and the conductivities, respectively. The arrows show the direction of the integration [11].

The problem of finding electric field distribution in a volume conductor with respect to Eq.(3.36) can be written as:

$$\sum_{j=1}^{N_p} \phi_j \left(\int_{\Omega} (\sigma\nabla\alpha_j) \cdot \nabla\alpha_i \, dS \right) = -\int_{\partial\Omega} \sigma\alpha_i \frac{\partial \vec{A}_p}{\partial t} \cdot d\vec{\Gamma} \ , \ i = 1, 2, 3, ..., N_p \tag{3.37}$$

The volume conductor is assumed to be divided into several triangular meshes. A simple case consisting two triangles with different conductivities is shown in Fig.3.10. The linear system of equations in (3.37) for element 1 is as follows:

$$\begin{bmatrix} C_{11}^1 & C_{12}^1 & C_{13}^1 \\ C_{21}^1 & C_{22}^1 & C_{23}^1 \\ C_{31}^1 & C_{32}^1 & C_{33}^1 \end{bmatrix} \begin{bmatrix} \phi_1^1 \\ \phi_2^1 \\ \phi_3^1 \end{bmatrix} = \begin{bmatrix} -\oint_{\Gamma_1} \sigma_1 \alpha_1^1 \frac{\partial \vec{A}_p}{\partial t} \cdot d\Gamma \\ -\oint_{\Gamma_1} \sigma_1 \alpha_2^1 \frac{\partial \vec{A}_p}{\partial t} \cdot d\Gamma \\ -\oint_{\Gamma_1} \sigma_1 \alpha_3^1 \frac{\partial \vec{A}_p}{\partial t} \cdot d\Gamma \end{bmatrix} \tag{3.38}$$

where

$$C_{ij}^{k} = \int_{S_1} \sigma_k \nabla \alpha_j^k \cdot \nabla \alpha_i^k \; dS \tag{3.39}$$

In terms of the global node numbering, the set of linear equations are explained as:

$$\begin{bmatrix} C_{11}^1 & C_{12}^1 & C_{13}^1 & 0 \\ C_{21}^1 & C_{22}^1 + C_{11}^2 & C_{23}^1 + C_{13}^2 & C_{24}^2 \\ C_{31}^1 & C_{32}^1 + C_{31}^2 & C_{33}^1 + C_{33}^2 & C_{34}^2 \\ 0 & C_{42}^2 & C_{43}^2 & C_{44}^2 \end{bmatrix} \begin{bmatrix} \phi_1 \\ \phi_2 \\ \phi_3 \\ \phi_4 \end{bmatrix} = b(\sigma) \tag{3.40}$$

where $b(\sigma)$ is a 4x1 vector.

$$b(\sigma) = \begin{bmatrix} -\int_1^2 \sigma_1 \alpha_1^1 \frac{\partial \vec{A}_p}{\partial t} \cdot d\vec{\Gamma} - \int_3^1 \sigma_1 \alpha_1^1 \frac{\partial \vec{A}_p}{\partial t} \cdot d\vec{\Gamma} \\ -\int_1^2 \sigma_1 \alpha_2^1 \frac{\partial \vec{A}_p}{\partial t} \cdot d\vec{\Gamma} - \int_3^2 \sigma_2 \alpha_1^2 \frac{\partial \vec{A}_p}{\partial t} \cdot d\vec{\Gamma} - \int_2^3 \sigma_1 \alpha_2^1 \frac{\partial \vec{A}_p}{\partial t} \cdot d\vec{\Gamma} - \int_2^4 \sigma_2 \alpha_1^2 \frac{\partial \vec{A}_p}{\partial t} \cdot d\vec{\Gamma} \\ -\int_4^3 \sigma_2 \alpha_3^2 \frac{\partial \vec{A}_p}{\partial t} \cdot d\vec{\Gamma} - \int_2^4 \sigma_2 \alpha_3^2 \frac{\partial \vec{A}_p}{\partial t} \cdot d\vec{\Gamma} \\ -\int_3^1 \sigma_1 \alpha_3^1 \frac{\partial \vec{A}_p}{\partial t} \cdot d\vec{\Gamma} - \int_2^3 \sigma_1 \alpha_3^1 \frac{\partial \vec{A}_p}{\partial t} \cdot d\vec{\Gamma} - \int_2^3 \sigma_2 \alpha_2^2 \frac{\partial \vec{A}_p}{\partial t} \cdot d\vec{\Gamma} - \int_4^3 \sigma_2 \alpha_2^2 \frac{\partial \vec{A}_p}{\partial t} \cdot d\vec{\Gamma} \end{bmatrix} \tag{3.41}$$

The node voltages can be calculated from Eq.(3.40).

$$V = \mathbf{C}^{-1}(\sigma) b(\sigma) \tag{3.42}$$

where $\mathbf{C}$ is the global coefficient matrix generated from the element coefficient matrix given in Eq.(3.40).

3.4.2 Series Expansion Method (SEM)

In order to solve the scalar potential distribution analytically, a series expansion method can be used. As a result, an approximate solution can be determined. Since the problem geometry is rectangle, the Laplace equation with the Neumann boundary conditions in Cartesian coordinates is considered. In the case of x-oriented two symmetric coils, the top and the bottom boundary conditions can be approximated as homogeneous boundary conditions. This is due to the fact that y-component of the magnetic vector potential is negligibly small. The

problem geometry is given in Figure 3.11 and the governing equations are as follows:

$$\nabla^2\Phi(x,y) = \Phi_{xx} + \Phi_{yy} = 0 \tag{3.43}$$

$$\begin{aligned} B.Cs: \quad & \Phi_y(x,-b/2) = \Phi_y(x,b/2) = 0 \\ & \Phi_x(-a/2,y) = f_1(y),\ \Phi_x(a/2,y) = f_2(y) \end{aligned} \tag{3.44}$$

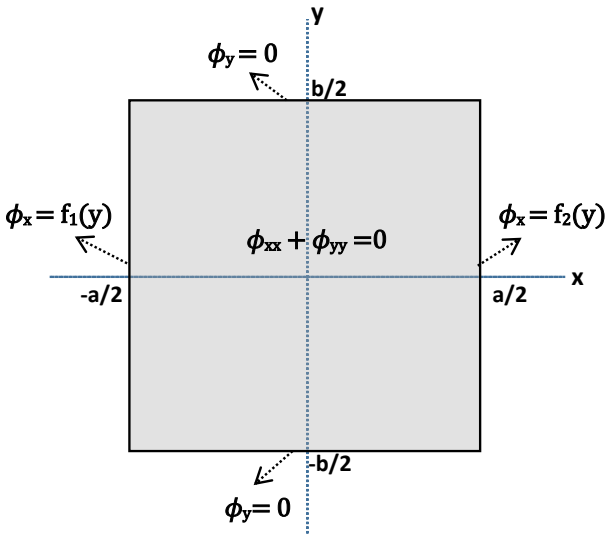

Figure 3.11: The problem geometry (conductive body) for x-oriented two symmetric coils. The top and the bottom boundaries are treated as homogeneous boundaries.

the solution of (3.43) is in the form of:

$$\Phi(x,y) = \sum_{n=1}^{N} \left(C_n \cosh(\lambda_n x) + D_n \sinh(\lambda_n x)\right) \cos(\lambda_n y) \tag{3.45}$$

where $\lambda_n = \frac{2n\pi}{a}$

the coefficient C_n and D_n are determined from the following equations:

$$\lambda_n \left(C_n \sinh(-\lambda_n a/2) + D_n \cosh(-\lambda_n a/2)\right) = \frac{2}{b} \int_{-b/2}^{b/2} f_1(y) \cos(\lambda_n y) dy \tag{3.46}$$

$$\lambda_n \left(C_n \sinh(\lambda_n a/2) + D_n \cosh(\lambda_n a/2)\right) = \frac{2}{b} \int_{-b/2}^{b/2} f_2(y) \cos(\lambda_n y) dy \qquad (3.47)$$

3.4.3 Results

In Figure 3.12 the x-component of $\frac{\partial A}{\partial t}$ for both coil configurations are shown. In the symmetric coil, the y-component of $\frac{\partial A}{\partial t}$ is small, so its contribution to the electric field is negligible. However, in the square loop coil, the y-component has similar distribution with the x- component. The scalar potential Φ obtained from Eq.(3.42) is given in Fig.3.13. The charge accumulates on the boundary of the conductor so that spatial derivative of Φ will be in the reverse direction of time derivative of the magnetic vector potential. Therefore, the electric field is expected to be lower in the conductive medium compared to the non-conductive medium.

The total electric field distributions for both coil configurations are given in Fig.3.14. In the symmetric coil, since the magnetic vector potential is in the x-direction, the field exists mostly in the x-direction. In the encircling coil, as it is expected, the field has the same behaviour in x- and y- directions. The arrow plots of these fields shown in Fig.3.15, give more information about the field distribution. Since at the air-conductor interface the normal component of the current is zero, the field is tangential to the boundary. The rotation direction of the electric field, i.e. the curl of the electric field, shows the direction of the magnetic flux density due to the current flowing in the coil. This is a direct result of the Faraday's Law given in Eq. 2.19. Another result deduced from Fig.3.15 is that it is not possible to get rid of the null point in the volume conductor. In the null point, the electric field is zero, so this point cannot be sensed in the conductivity imaging or stimulation of the nerve excitation.

In order to check the validity of the provided FEM results, the SEM results for the x-oriented symmetric coil are given in the Figure 3.16. The results match with the FEM results provided in the 3.14-a.

To simulate the inhomogeneous case, a 5×5 mm rectangular conductivity per-

turbation is placed in the centre of the model. The field is calculated for the symmetric coil to see the inhomogeneity effect. The results of $\sigma_{inh} = 3\sigma_0$ and $\sigma_{inh} = 100\sigma_0$ are given in Fig.3.17. As shown in Eq.(2.18), normal component of the current is continuous at the boundary, so the electric field decreases in the high conductivity region.

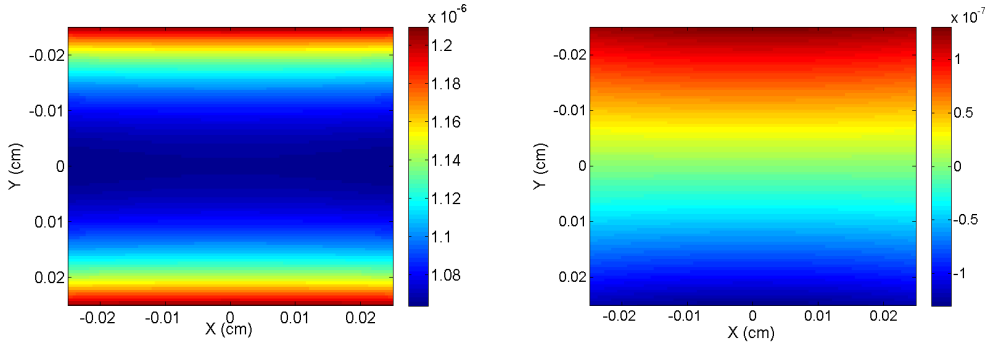

(a) (b)

Figure 3.12: Analytically calculated $\frac{\partial Ax}{\partial t}$ expressions for (a) symmetric coil and (b) encircling square loop coil.

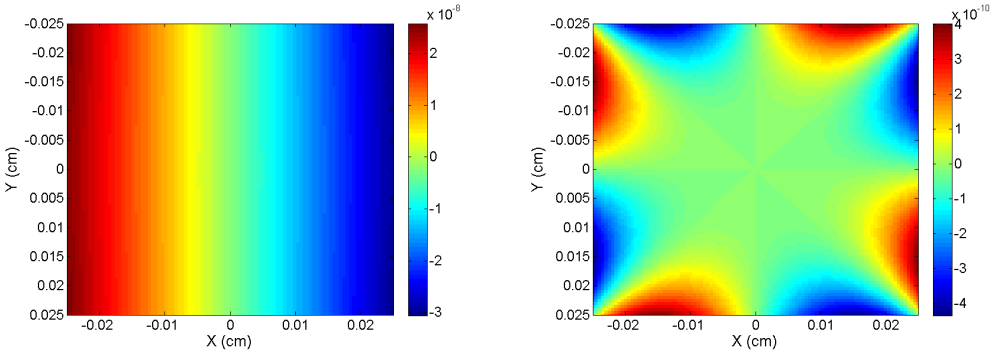

(a) (b)

Figure 3.13: The scalar potential distribution Φ of homogeneous conductive body for (a) symmetric coil and (b) encircling square loop coil.

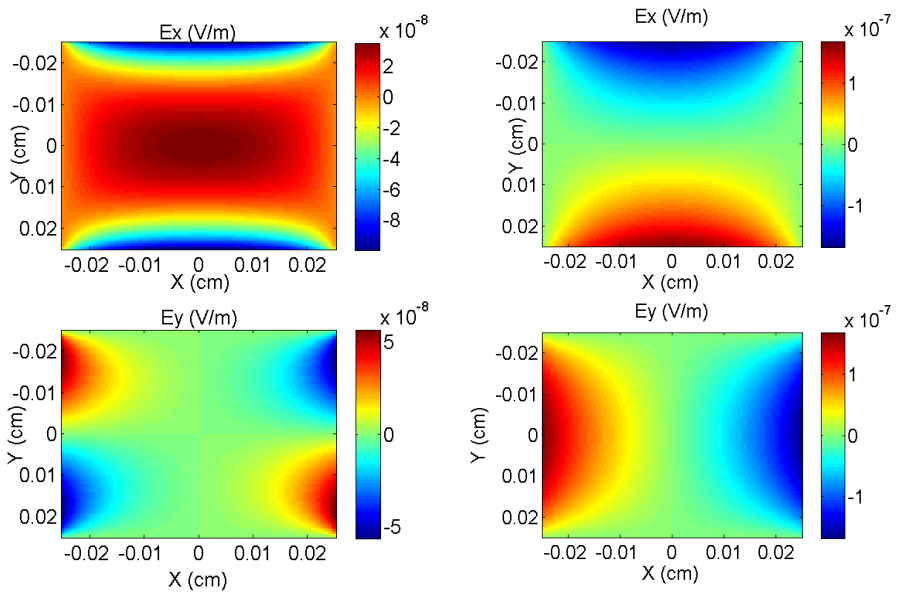

(a) (b)

Figure 3.14: Electric field of the homogeneous conductive body for (a) symmetric coil and (b) encircling square loop coil

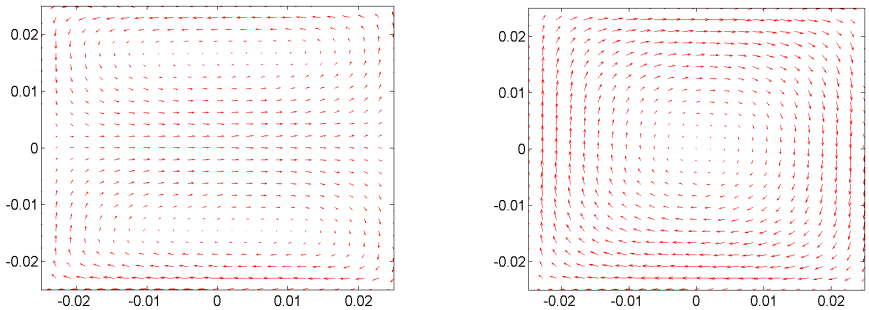

(a) (b)

Figure 3.15: Arrow plot of electric field of the homogeneous conductive body for (a) symmetric coil and (b) encircling square loop coil.

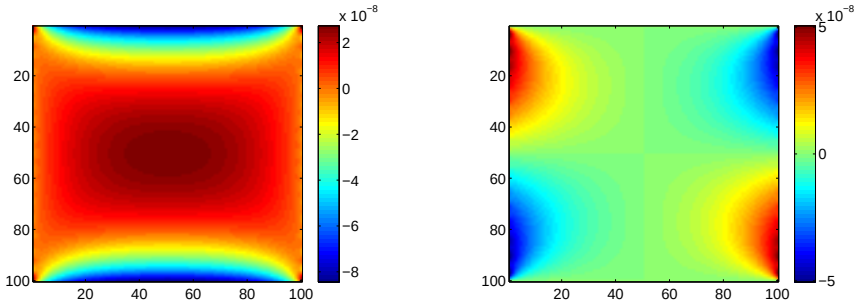

Figure 3.16: SEM result of Electric field of the homogeneous conductive body. Two symmetric coils are placed in the x-direction.

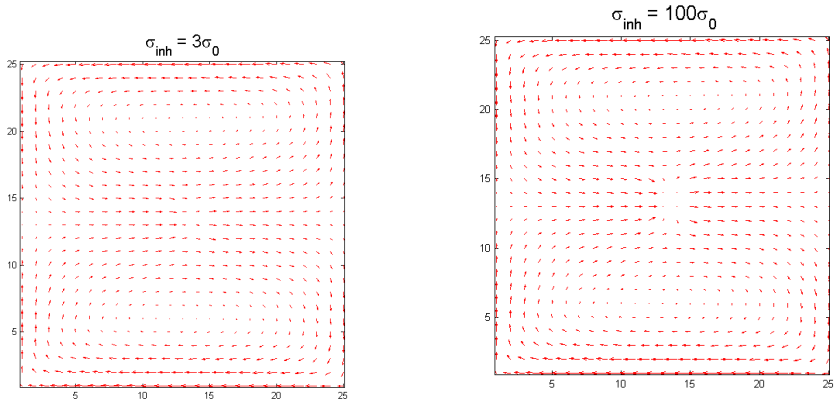

(a) (b)

Figure 3.17: Electric field of the conductive body when 5×5 mm inhomogeneity added to the center of the model (a)$\sigma_{inh} = 3\sigma_0$ (b) $\sigma_{inh} = 100\sigma_0$

3.5 Feasibility and Limitations of the LFEIT

3.5.1 Ultrasound Frequency

As discussed before, the ultrasound excitation on a conductive body (inside a static magnetic field) causes a current distribution inside the body. The dimension of the velocity current distribution is related to the ultrasound beam width and wavelength. In addition, the operation frequency of this excitation affects the developed current distribution. In order to analyse the frequency effect on the received signal, the derived voltage equation 2.39 can be used.

$$V_{ind}(t) = \int_{V_{body}} \left(\vec{E}_R^0(\vec{r}) \cdot \left(\sigma(\vec{r}) \frac{1}{\rho(\vec{r})} \left(\frac{\partial p(\vec{r},t)}{\partial r} \times \vec{B}_0 \right) \right) \right) dr \tag{3.48}$$

The pressure wave is in the form of [38]:

$$p(\vec{r},t) = A\phi \frac{e^{j(\omega t - \vec{k}\cdot\vec{r})}}{|r|} \tag{3.49}$$

where ϕ is a function that represents the shape of the beam and it depends on the shape and the element number of the transducer and A is the amplitude of the pressure wave.

Since the wave number k is a coefficient of the spatial term, the result of the volume integration depends on it and the excitation frequency, as well. In order to evaluate the effect of frequency on the received signal, the model given in Figure-3.18-a is proposed. The conductive volume is divided into two different regions with conductivities of 0.01 S/m and 2 S/m, respectively. The input pressure is one cycle sinusoidal signal. Two different simulations are done with 0.5 MHz and 1 MHz excitation frequencies. The pressure distributions in the time instant of 1.2 μs are shown in Figure-3.18-c and Figure-3.18-d. The received signals are provided in Figure-3.18-e and Figure-3.18-f. As a result of the given simulations, the amplitude of the received signal decreases by increasing the excitation frequency. However, the spatial resolution of the imaging system is low for low frequencies. Consequently, there is a trade off between selecting the proper frequency to observe the higher amplitude signals and also keeping the resolution high.

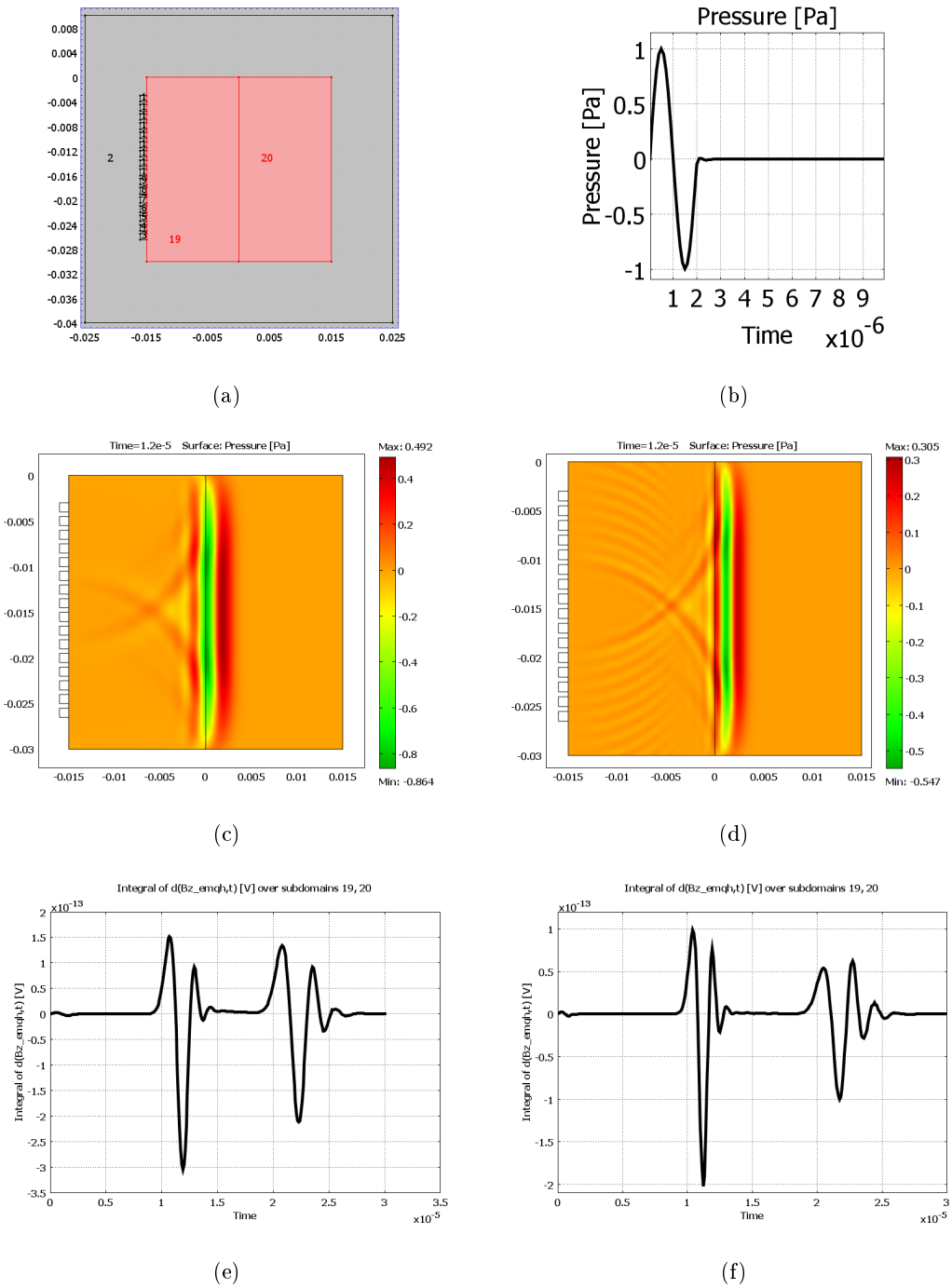

(a) (b)

(c) (d)

(e) (f)

Figure 3.18: Simulation model and the excitation frequency effect on the received signal. (a) simulation model, (b) one cycle excitation signal, (c,e) The pressure distribution and received signal for f = 0.5 MHz,(d,f) The pressure distribution and received signal for f = 1 MHz

3.5.2 Current Limitation

The safety limit on the current is inversely proportional to the operating frequency of the ultrasound. Maximum level of the current density is restricted to 0.2 A/m^2 at 100 kHz, 2 A/m^2 at 1 MHz, and 20 A/m^2 at 10 MHz [39]. The induced current in the body is given in 3.23. For the conductivity of 0.2 S/m and the static magnetic flux density of 1 Tesla, the particle velocity can be increased up to 10 m/s^2 in the case of the 1 MHz ultrasound excitation. The pressure limit can be derived from the governing acoustic wave equation 3.10. The relation between the pressure and the particle velocity is:

$$\frac{|P|}{|v|} = \rho c_s \tag{3.50}$$

For biological tissues the mass density ρ is 1000 kg/m^3 and the velocity of the sound is 1500 m/s. The pressure limit is calculated as 15 MPa with respect to the given conditions.

3.5.3 Ultrasound Exposure

In the biological applications, there exist limitations on the ultrasound radiation. Ultrasound exposure results in two different effects on the tissue, namely, the thermal and mechanical effects. These effects depend on the ultrasound intensity and the exposure duration. The limit for the ultrasound exposure is specified by U.S. Food and Drug Administration (FDA).

Intensity

The transmitted power by the ultrasound wave excitation determines the hazardous effect of the ultrasound exposure. This power is calculated from the wave intensity. The intensity extremely varies in the time and spatial domains. Thus, there are different intensity measures based on the spatial and temporal domains. In the pulse mode operation, the most applicable measures are the spatial peak-pulse average intensity (I_{SPPA}) and the spatial peak-temporal average intensity (I_{SPTA}). The FDA limits on the I_{SSPA} and I_{SPTA} are 190 W/cm^2

and 720 mW/cm^2, respectively [40]. These measures are calculated from the instantaneous intensity:

$$I_{inst} = \frac{P^2}{Z} \tag{3.51}$$

where Z is the acoustic impedance of the medium in terms of Rayls. For biological tissues, it is considered as 1.5 MRayls.

In the case of sinusoidal excitation, the peak pressure value should be less than 2 MPa to keep the I_{SSPA} below the limit. The pressure limit for I_{SPTA} depends on the duty cycle of the excitation pulse. For 0.5% duty cycle, maximum acceptable pressure is 1.74 MPa.

Mechanical Effect

The ultrasound radiation affects the embedded medium, mechanically. It develops the cavitation bubbles phenomenon inside the medium. While the ultrasound pulse passes through a bubble, if the pressure level is high enough, the bubble grows or collapse. The generated pressure and the temperature increase due to the bubble collapse can damage the surrounding tissue, extremely. In order to investigate the mechanical effect of the ultrasound radiation, the mechanical index (MI) term is used [41]:

$$MI = \frac{Max\left\{P_{negative}\right\}}{\sqrt{f}} \tag{3.52}$$

where $Max\left\{P_{negative}\right\}$ is the maximum negative pressure in terms of Mega Pascal and f is the operating frequency in MHz.

The FDA limit of MI is considered as 1.9 [42]. It means, for 1 MHz operating frequency, the peak value of the negative pressure should not exceed 1.9 Mega Pascal.

3.5.4 Receiver Sensitivity

The minimum power that can be received determines the receiver system quality. By assuming the received signal induced in the coil is not attenuated, the minimum signal in the input of receiver system can be calculated from [43]:

$$S_i = FkTB(S/N)_o \tag{3.53}$$

where F is the noise figure of the amplifier, k (1.380650×10^{-23} J/K) is the Boltzmann constant, T (290^o K) is the noise temperature of the receiver, B the bandwidth of amplifier, and $(S/N)_o$ is the minimum SNR at the output to detect the signal. In terms of dB 3.53 can be written as:

$$10logS_i = 10logF - 144 + 10logB + 10log(S/N)_o \tag{3.54}$$

Assuming 10 dB SNR at the output, 5 dB noise figure, and 5 MHz bandwidth, the minimum power in the input of the receiver signal will be:

$$10logS_i = 5 - 144 + 37 + 10 = -92 \;\; dBm \tag{3.55}$$

From the minimum power, the lowest rms value of the signal is determined from [43] :

$$V_{min} = \sqrt{(4R_sS_i)} = 1.589\sqrt{R_s} \;\; \mu V \tag{3.56}$$

where R_s is the source resistance in Ω.

CHAPTER 4

INVERSE PROBLEM IN LFEIT

4.1 Introduction

In the recent studies conducted at METU, the LFEIT has been used to find the electrical conductivity of different biological tissues using magnetic field measurements [1]. In these studies, the pick-up voltage expression (2.39) in the receiver coil is used to calculate the electrical conductivity. As can be seen in this expression, the reconstruction problem is not straightforward, because finding the conductivity distribution is a nonlinear problem. To overcome this problem, *the reference imaging method*, as explained below, can be utilized. In this method, the perturbation in the conductive medium with respect to a reference value is imaged by linearizing the induced voltage expression around a given reference value. Therefore, methods for solving the resultant linear system of equations (i.e. $\mathbf{Ax} = \mathbf{b}$) can be used to reconstruct the conductivity distribution. In the LFEIT formulation, the right hand side vector b represents the pick-up voltages induced in the receiver coil, $\mathbf{A}$ is the sensitivity matrix and x is the conductivity perturbation vector.

In this chapter, the continuous forward problem is linearized and discretized. The sensitivity matrix is obtained for different coil configurations and transducer positions, and its characteristics are analyzed. Thereafter, the image reconstruction algorithms and regularization methods are evaluated. The regularization methods are discussed in two different categories as iterative and sparse regularization techniques.

4.2 Linearization of Inverse Problem

Assuming continuous time domain and uniform conductivity distribution, the pick-up voltage expression (2.39) in the receiver coil is as follows :

$$V_0(t) = \int_{V_{body}} \left(\vec{E}_R^0(\sigma_0, \vec{r}) \cdot \left(\sigma_0 \frac{1}{\rho(\vec{r})} \left(\frac{\partial p(\vec{r}, t)}{\partial r} \times \vec{B}_0 \right) \right) \right) dV \tag{4.1}$$

When a conductivity perturbation exists, the pick-up voltage changes:

$$V(t) = \int_{V_{body}} \left(\vec{E}_R^0(\sigma_0 + \Delta\sigma, \vec{r}) \cdot \left((\sigma_0 + \Delta\sigma) \frac{1}{\rho(\vec{r})} \left(\frac{\partial p(\vec{r}, t)}{\partial r} \times \vec{B}_0 \right) \right) \right) dV \tag{4.2}$$

Since the reciprocal electrical field is also a function of medium conductivity the relation between the measurements and body conductivity is nonlinear. Therefore, it is not easy to solve the conductivity reconstruction problem. However, if the reciprocal electric field is assumed to be same as in the homogeneous case, the problem can be linearized around that homogeneous distribution and a linear equation can be obtained:

$$\Delta V(t) = \int_{V_{body}} \Delta\sigma(\vec{r}) \left(\vec{E}_R^0(\sigma_0, \vec{r}) \cdot \left(\frac{1}{\rho(\vec{r})} \left(\frac{\partial\ p(\vec{r}, t)}{\partial r} \times \vec{B}_0 \right) \right) \right) dV \tag{4.3}$$

where ΔV represents the change in the receiver coil voltage due to conductivity perturbation. The linearization condition is given below:

$$\vec{E}_R^0(\sigma_0 + \Delta\sigma, \vec{r}) = \vec{E}_R^0(\sigma_0, \vec{r}) \tag{4.4}$$

The validity of the linearization process depends on the conductivity changes. To explore the conductivity range necessary for linearity assumption, a conductive body is modeled with a perturbation as in Figure-3.17. In two symmetric coil configuration, a 5x5 mm sized inhomogeneity is placed in the middle of 5x5 cm body model. The reciprocal electric fields for different conductivity changes are solved assuming a coil current in x-direction and $dI/dt = 1\ A/s$. The results show that the linearization assumption is valid up to 50% change around the initial conductivity distribution.

The voltage induced in the receiver coil is illustrated in Figure 4.2 for a 50% change. In this figure, the reciprocal voltage determined by equation (4.3) is provided in addition to the received voltage obtained from the electromagnetic

simulation. The medium is excited by 1 MHz 16 element phased array transducer. As can be seen in Figure 3.5, the pressure wave is unimodal and its amplitude is 1 MPa. The results are in a good agreement with the linearization approximation.

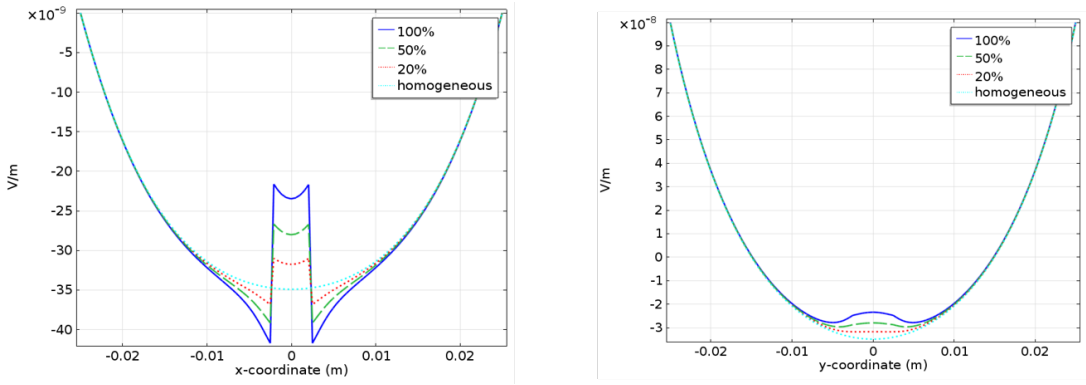

Figure 4.1: Reciprocal electrical fields for different conductivity changes. Two symmetric coils in x- direction are assumed. The change in the conductivity distribution is generated at the center of the body. The electric field distribution is given along the line passing through the center of body where y = 0 (left) and x = 0 (right).

The linearization method can be used for higher changes in conductivity. However, this provides conductivity contrast imaging instead of the true imaging. This study focuses on the true imaging, therefore the conductivity changes below 50% are considered.

The integral equations of 4.3) are similar to the Fredholm integral equations of the first kind (IFK) as given below [44]:

$$\int_a^b K(r,t)f(r)dr = g(t) \tag{4.5}$$

where $K(r,t)$ is a square integrable kernel, $f(r)$ is the solution and $g(t)$ is the measurement.

Equation (4.3) is an IFK when its kernel $\left(\vec{E}_R^0(\sigma_0,\vec{r})\cdot\left(\frac{1}{\rho(\vec{r})}(\frac{\partial\ p(\vec{r},t)}{\partial r}\times\vec{B}_0)\right)\right)$ is square integrable. Since the ultrasound excitation is time limited, the developed pressure wave inside the medium is nonzero only where the US wave is passing. Therefore, the kernel function of Eq. (4.3) is expected to be square-integrable.

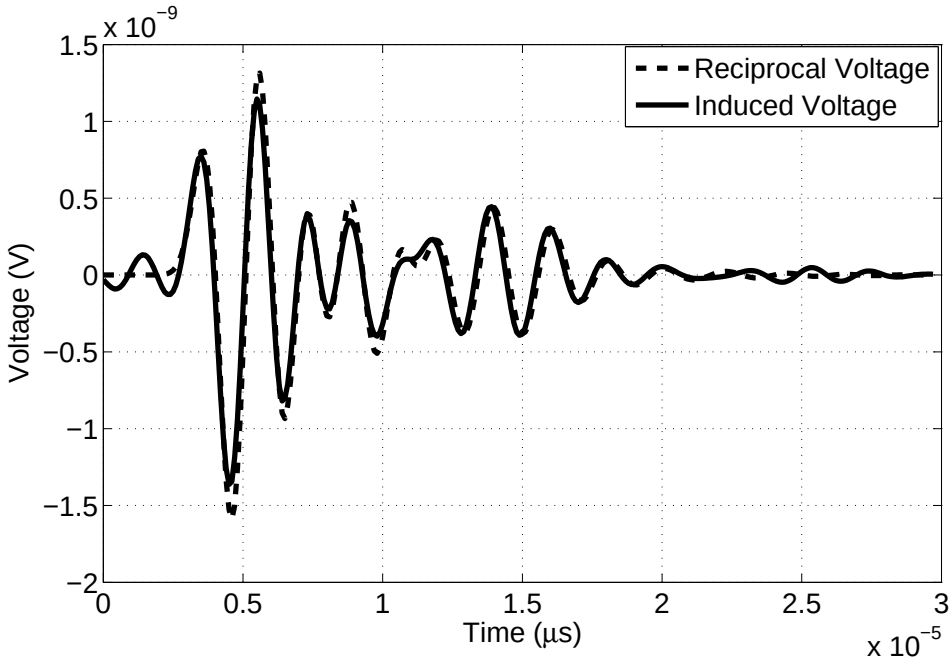

Figure 4.2: Induced voltage in the coil for 50% conductivity perturbation, and 1 MPa excitation with 16 element phased array transducer. Solid line shows the received voltage, dashed line (- - -) is related to the calculated voltage from 4.3

To evaluate the characteristic of the imaging modality, the properties of the IFK should be evaluated.

In order to justify that the mathematical model of the imaging system is well defined, it is crucial to consider *solution existence*, *uniqueness* and *stability* issues [44]. Hadamard's criterion is used to identify if the problem is ill-posed.

1. *Existence*: There should be a solution model to fit the data, perfectly. If the solution does not exist, the mathematical model is wrong and the problem should be redefined.

2. *Uniqueness*: The solution should be unique. It is not unique when the model m_0 lies in the null space of the kernel function. Additional constraint, i.e. minimum norm can be imposed to overcome this problem.

3. *Stability*: The solution should be dependent on the data and parameters. If this condition is not satisfied, the result will be unstable. Therefore, small changes in the measurements yield large variations in the solution. For example,

if the perturbation $\delta f(r) = \tau sin(2\pi mr)$ with $m = 1, 2, \ldots$ is added to the solution $f(r)$ the difference in the measurement will be

$$\delta g(t) = \tau \int_a^b K(r,t) sin(2\pi mr) dx \tag{4.6}$$

According to the Riemann-Lebesgue lemma the result of equation (4.6) approaches to zero as m goes to infinity, and the value of the $\|\delta f(r)\|/\|\delta g(t)\|$ becomes too high [44]. In other words, the high frequency components are dampen more in comparison with the low frequency components. Therefore, the measurements related to the high frequencies will be corrupted by the noise and problems such as being sensitive to the noise is expected in the reconstruction process. This problem is called as *ill-posed problem* [44]. In the discrete domain, the stability of the solution is examined by considering the singular values of the matrix obtained from the kernel function.

In order to have more information about the stability of the equation 4.3, the discrete problem should be considered. The discrete form of the problem can be written as

$$\Delta V(i) = \sum_{j=1}^{N} \Delta\sigma(j) S(i,j) \Delta v \tag{4.7}$$

$$S(i,j) = \left(\vec{E}_R^0(\sigma_0, j) \cdot \left(\frac{1}{\rho(j)} \left(\frac{\partial p(i,\vec{r})}{\partial r} |_{r=j\Delta r} \times \vec{B}_0 \right) \right) \right) \tag{4.8}$$

where $S(i,j)$ is the sensitivity of the measurement at time instant i to the conductivity perturbation on the j^{th} voxel. As shown in equation (4.8), it is determined by the dot product of the reciprocal electric field with particle acceleration. N is the total number of pixels in the conductive model. The number of independent measurements can be increased by changing the transducer/coil configuration as given in Section 3. Consequently, a matrix equation is obtained as follows:

$$\Delta \mathbf{V} = \mathbf{S} \Delta\sigma \tag{4.9}$$

As stated above, $\mathbf{S}$ is expected to be an ill-conditioned matrix since it is derived from a Fredholm integral of the first kind.

4.3 Properties of Sensitivity Matrix

For a specific receiver/transducer configuration the number of measurements is not sufficient to solve the problem. By changing the transducer or coil configuration, the number of independent measurement can be increased. However, this may yield dependent measurements for different excitations and receiver positions. Therefore, the number of independent measurements should be analyzed for a specific body, transducer, and coil configuration. The singular value decomposition (SVD) technique is an analysis tool for this purpose. Also, SVD provides information about the degree of ill-posedness in the imaging system.

Assume that $\mathbf{S}$ is a $n \times m (m < n)$ matrix, the SVD of $\mathbf{S}$ is defined as

$$\mathbf{S} = \mathbf{U}\mathbf{\Sigma}\mathbf{V}^{\mathbf{T}} = \sum_{i=1}^{n} \sigma_i u_i v_i^T \tag{4.10}$$

Here, $\mathbf{\Sigma}$ is a diagonal matrix with the singular values, satisfying $\sigma_1 \geq \sigma_2 \geq ... \geq \sigma_n \geq 0$, the matrices $\mathbf{U}$ and $\mathbf{V}$ consist of orthonormal right ($\mathbf{U} = (u_1, ..., u_n)$) and left ($\mathbf{V} = (v_1, ..., v_n)$) singular vectors.

The SVD gives two independent bases which are constituted from left and right singular vectors, respectively. The voltage measurements obtained from the system are in the basis of the left singular vectors, whereas the reconstructed image ($\Delta\sigma$) is in the basis of the right singular vectors. These bases determine the performance of the system.

In order to understand the response of each pixel in the imaging domain, the resolution matrix can be calculated. If k singular values are used for the reconstruction, then the resolution matrix $\mathbf{R_m}$ is calculated as:

$$\mathbf{R_m} = \mathbf{V(1:k)V(1:k)^T} \tag{4.11}$$

The resolution matrix provides information about the imaging system. A specific diagonal entry of $\mathbf{R}_m$ corresponds to the reconstructed value of the voxel when there is a perturbation in that specific voxel. The image obtained using the diagonal entries of the resolution matrix on the geometrical location is called the **resolution map**. The **resolution maps** evaluated for $k = 2000$ and $k = 3000$

are given in Figure 4.3 when the image consists of 60×60 pixels. In this case, the receiver coil is placed at the center of the system and it encircles the imaging domain. It is clear that the pixels close to the excitation positions are sensed properly. However, the sensitivity of the pixels far from the transducer are poor. As the number of the left singular vectors are increased, the sensitivity becomes better. But the sensitivity of the middle pixel remains low. The low sensitivity is due to the reciprocal electric field behavior. Since, the encircling coil has a null point at its center, the sensitivity is low in the middle part. In addition, when generalized inverse solution or k singular vectors is used, R_m gives information about the amount of the image distortion. This test is called as **resolution test**. In this test, it is assumed that the noise dose not exist in the measurement. The reconstructed image which is obtained from the resolution test can be written as:

$$x_{rec} = \mathbf{R}_m x_{true} \tag{4.12}$$

where x_{rec} and x_{true} are the reconstructed and test images, respectively. The result obtained from the encircling coil is given in Figure 4.4. As it is shown, even if the data is perfect in the resolution map, the perturbation cannot be reconstructed at the center of the image.

The resolution map and the resolution test show the properties of the $\mathbf{S}$ matrix. They reflect the characteristics of the imaging system based on body, coil configuration, ultrasonic transducer position, and ultrasonic excitation properties.

Another property that can be revealed from the SVD of the sensitivity matrix is the stability of the problem. The stability of the imaging system can be evaluated by determining the singular values of the kernel matrix $\mathbf{S}$. The singular values for the case where coil is placed at the center are plotted in Figure 4.5. The condition number of the matrix $\mathbf{S}$ ($cond(\mathbf{S})$) is defined as the ratio of the highest singular value (σ_0) to the smallest singular values (σ_n). The noise in the measurement is increased up to a value less than or equal to $cond(\mathbf{S})$ times of the error in the measurement. Therefore, when the condition number is small, the system is stable and called as *well-posed*. On contrary, large condition number corresponds to the unstable or an *ill-posed* system. From the singular value plot

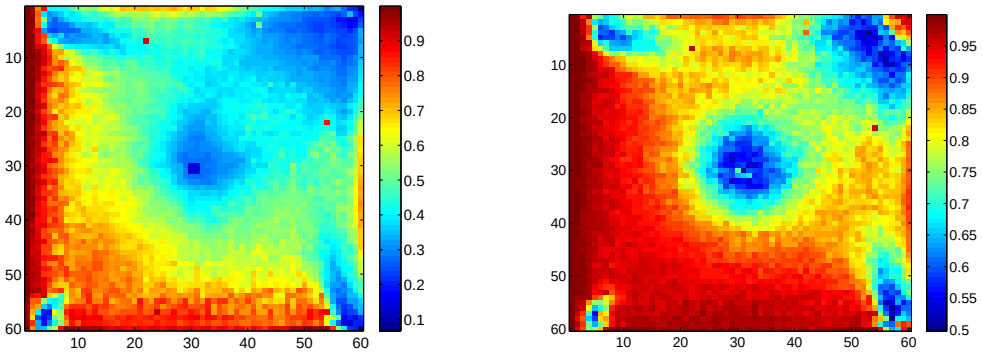

(a) (b)

Figure 4.3: Sensitivity of the system for different number of singular vectors when the encircling coil is placed at the center of the system. (a) 2000 singular vectors (b) 3000 singular vectors

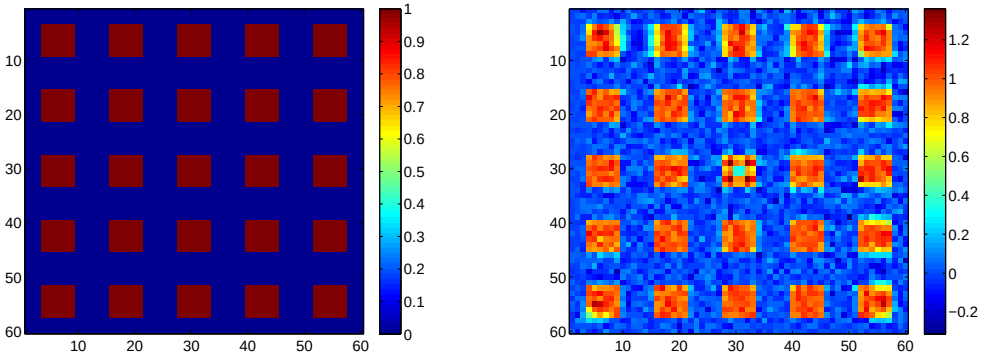

(a) (b)

Figure 4.4: Resolution test results. (a) Test model, (b) Reconstructed image for $k = 2000$

of the LFEIT system with a circular encircling coil as a receiver, the condition number is calculated as $cond(\mathbf{S}) = 4.91 \times 10^{17}$. One may conclude that the LFEIT system with that receiver coil geometry is highly unstable.

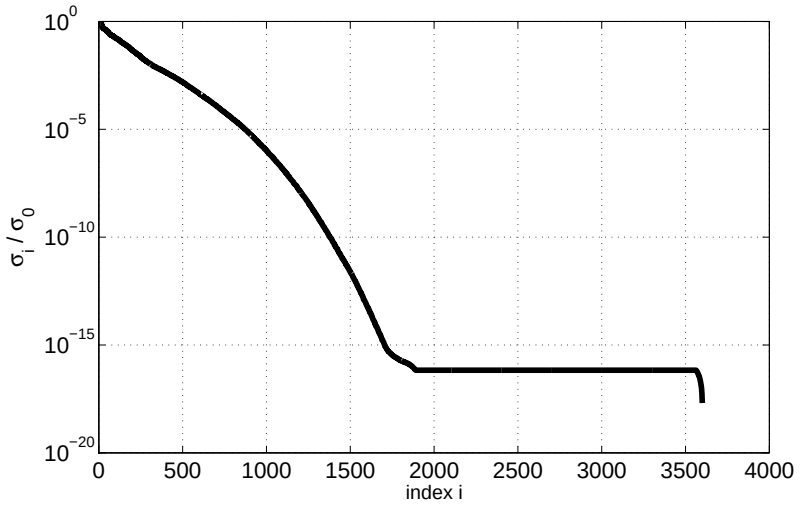

Figure 4.5: Singular values of the kernel matrix when the receiver coil is in the middle. The distance between the medium and the coils are 1 cm. The ultrasound excitation is from top and left side of the medium and maximum pressure is 1 Pa.

4.3.1 The Effect of Coil Configuration

As discussed above, when the receiver coil encircles the medium, the response of the pixel at the center is low. In order to overcome this problem, an alternative coil configuration is proposed in [1]. The electric field distribution of this coil configuration is given in Figure 3.14.

In order to sense the flux density of the velocity current distribution, two different coil pair is placed around the medium. The first pair of coils is at the top and bottom sides of the medium oriented in x direction. The other pair is in the left and right side of the medium in y direction. So, the velocity current distribution in x and y is sensed. Since for each excitation two different measurements are taken, the data length is two times of the one obtained from one encircling

coil. To compare coil configurations with each other, the singular values of the alternative configuration is shown in Figure 4.6. The singular values decays slower but there is no improvement in the condition number. The new system is still ill-posed. The resolution map and the resolution test result is given in Figure 4.7. As expected, the response of the middle pixel is good and the perturbation in the pixels far from the transducer are poor. Even if the new configuration is better, the received signal amplitude is weaker than the received signal obtained from the encircling coil as given in Figure 4.8 and Figure 4.9. Therefore, there is a trade off between the sensitivity and the received signal amplitude.

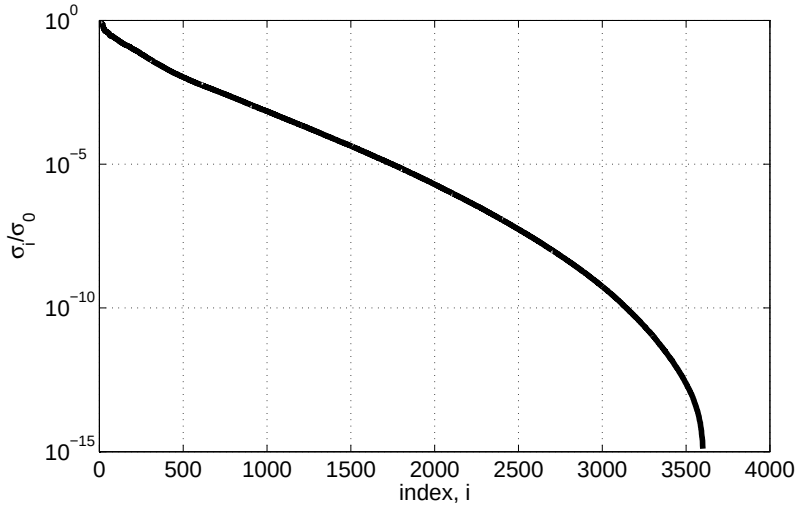

Figure 4.6: Singular values of the kernel matrix when the two symmetric receiver coils are used. The distance between the medium and the coils are 2 cm. The ultrasound excitation is from top and left side of the medium and maximum pressure is 1 Pa.

4.3.2 Effect of the Pressure Pulse Shape

Another variable that effect the sensitivity of the system is the pressure pulse shape. In the previous sections, the sensitivity distribution has been given for the unimodal pressure excitation as shown in Figure 3.5. Similar simulations are done for one cycle of sinusoidal excitation. The singular values of one cycle

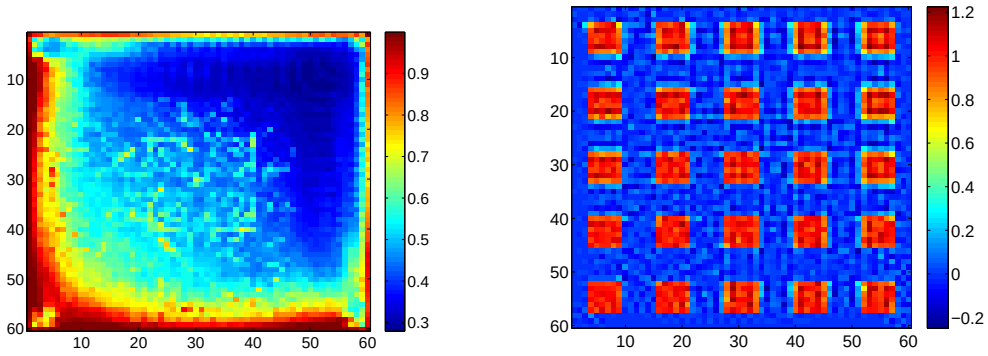

(a) (b)

Figure 4.7: Resolution test results for xy coil. (a) Resolution map, (b) Resolution test of the model 4.4, $k = 2000$

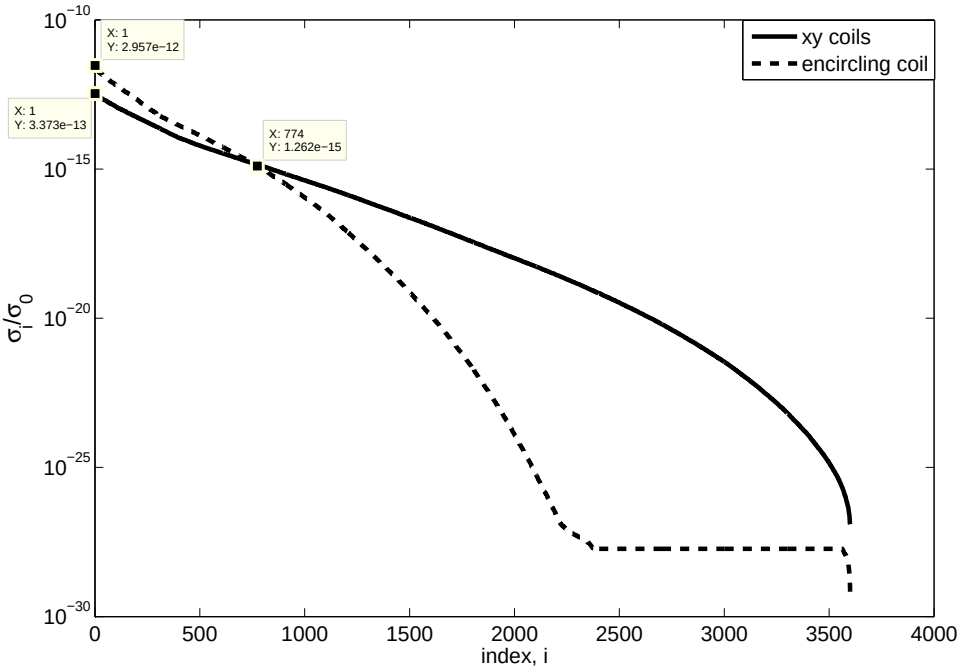

Figure 4.8: Singular value pattern of the encircling and xy coil configuration. In both cases the distance between the medium and the coils are 2 cm. The ultrasound excitation is from top and left side of the medium and maximum pressure is 1 Pa. For encircling coil $\sigma_0 = 2.96e-12$ and for xy coils $\sigma_0 = 3.37e-13$. Their intersection is $\sigma_{774} = 1.28e-15$.

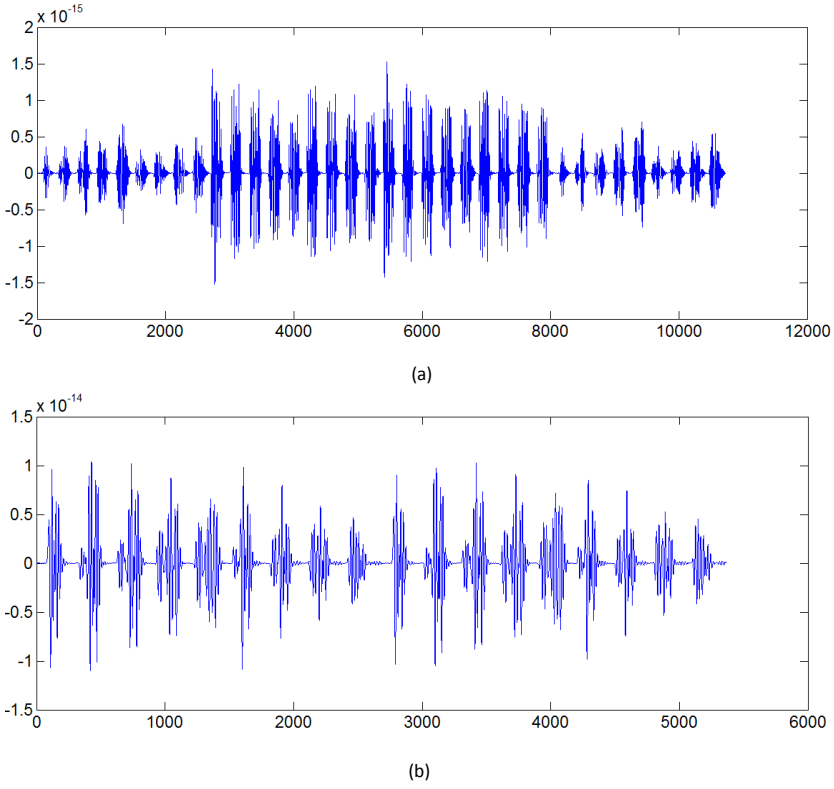

Figure 4.9: Measurement of the (a) encircling and (b) xy coil configuration. The background conductivity is 0.2 S/m and the conductivity perturbation model given in Figure 4.11-a is simulated. In both cases the distance between the medium and the coils are 2 cm and . The ultrasound excitation is from top and left side of the medium and maximum pressure is 1 Pa.

excitation is plotted in Figure 4.10. Comparing the unimodal pressure excitation, the decay pattern of the singular values is better than the one in previous excitation. With that pressure excitation, more independent set of vectors can be used in the image reconstruction. However, the available commercial transducers mostly produce the pressure given in Figure 3.5. Therefore, The results obtained from this type of excitation is provided in this study.

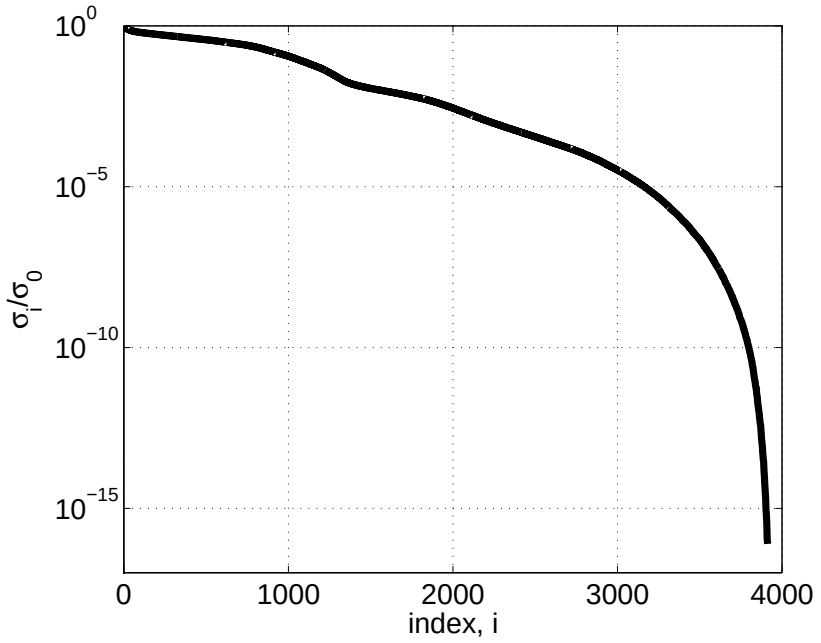

Figure 4.10: Singular values of the kernel matrix. The inward acceleration is one cycle sinusoidal. The ultrasound excitation is from top and left side of the medium and maximum pressure is 1 Pa.

4.4 Image Reconstruction

The least square solution or naive solution of 4.9 is related to the SVD component as:

$$x^{naive} = \sum_{i=1}^{n} \frac{u_i^T b}{\sigma_i} v_i \tag{4.13}$$

The least square solution is composed of the independent vectors obtained using

SVD as given in (4.13). In the least square solution, each component is divided by the corresponding singular value. Therefore, the components related to the small singular values are more sensitive to the noise. Decreasing the singular values, small changes in the measurements are amplified more and the solution starts to diverge from the true solution to the naive solution (least square solution). As mentioned in the previous section, since this system is in the form of IFK, this instability is expected.

In order to analyze instability behavior, Figure 4.12 is illustrated. In this figure, the perturbed x and the exact solution satisfy the following equations:

$$\mathbf{A}x^{exact} = b^{exact}, \quad \text{and} \quad \mathbf{A}x = b = b^{exact} + e \tag{4.14}$$

where e is the measurement noise. The classical perturbation theory satisfies the following error bound [45]:

$$\frac{\|x^{exact} - x\|_2}{\|x^{exact}\|_2} \leq cond(\mathbf{A}) \frac{\|e\|_2}{\|b^{exact}\|_2} \tag{4.15}$$

As shown in Figure 4.11 and Figure 4.12, the perturbed solution is far different from the exact solution, because the condition number of $\mathbf{A}$ is high. This occurs because $\mathbf{u_i^T e}$ term becomes comparable with σ_i even for lower noise. Therefore, the regularization should be employed in the reconstruction process in order to suppress the noise effect. In the following sections, different regularization methods are presented and corresponding solutions are presented.

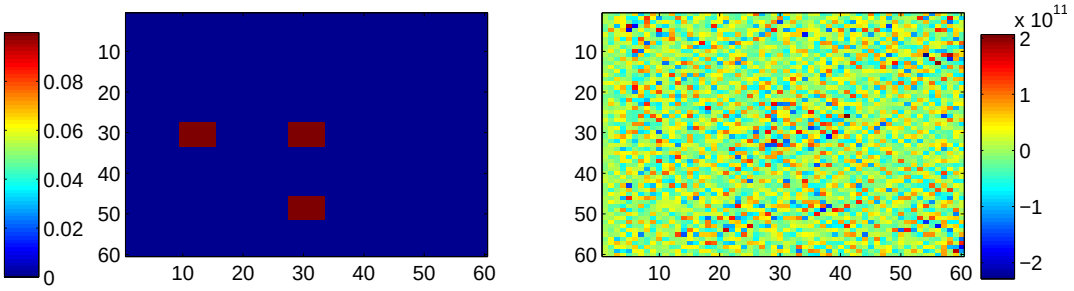

Figure 4.11: (a) Exact solution (b)Naive solution

.

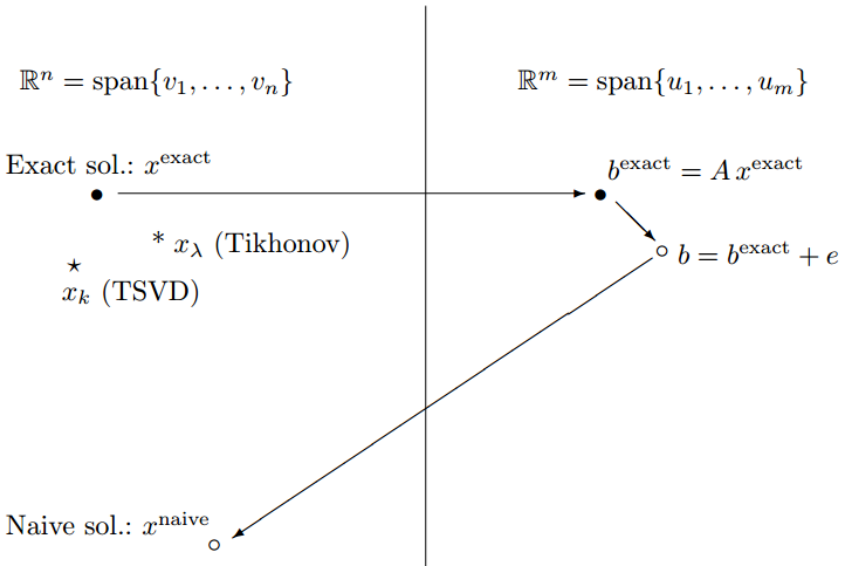

Figure 4.12: The diagram of the solution and the measurement domains. The left side is the space of the right singular vectors and the right side is the left singular vector space. The matrix **A** maps $\mathbb{R}^n$ to $\mathbb{R}^m$ [2]

.

4.4.1 Spectral Filtering

In order to be close to the true solution, the effect of the small singular values should be suppressed or filtered by means of regularization methods. Regularization based on suppression of the singular values is called spectral filtering. The solution obtained from the filtered expansion is in the form of:

$$x_{reg} = \sum_{i=1}^{n} \varphi_i \frac{u_i^T b}{\sigma_i} v_i \tag{4.16}$$

where φ_i is the filter factor associated with the i^{th} singular values.

The truncated SVD (TSVD) and Tikhonov regularization techniques are the most popular spectral filtering methods because of their analysis and implementation simplicity.

4.4.1.1 Truncated SVD

In the TSVD, extremely small singular values are neglected to decrease the noise effect. Thus, the filter factor and the solution obtained from the TSVD for k^{th} truncation become:

$$\varphi_i = \begin{cases} 1 & i < k \\ 0, & i > k \end{cases} \tag{4.17}$$

$$x_k = \sum_{i=1}^{k} \frac{u_i^T b}{\sigma_i} v_i \quad \text{where} \quad k < n \tag{4.18}$$

The perturbation bound for the TSVD is [2]:

$$\frac{\|x^{exact} - x_k\|_2}{\|x_k\|_2} \leq \frac{\sigma_1}{\sigma_k} \frac{\|e_2\|}{\|\mathbf{A}x_k\|_2} \tag{4.19}$$

Since σ_k is greater than σ_n, the error bound in this case is less than (4.15). So, the solution obtained from the TSVD is expected to be closer to the exact solution rather than the naive solution.

4.4.1.2 Tikhonov Regularization

Tikhonov regularization deals with the small singular values by minimizing both residual and smoothing norms. The solution x_λ is resulted from the following minimization problem [46]:

$$\min_x \left\{ \|\mathbf{A}x - b\|^2 + \lambda \|\mathbf{L}x\|^2 \right\} \tag{4.20}$$

The first and the second term of minimization problem are the residual and smoothing terms, respectively. L is smoothing operator and λ is the regularization parameter. The smoothing operator is a matrix and it can be chosen as zero order (identity), first order or a second order derivative matrix. The selection of L depends on the application and as its order increases, it provides smoother solution. In the case of zero order operator, the filter factor associated with Tikhonov solution is:

$$\varphi_i = \frac{\sigma_i^2}{\lambda^2 + \sigma_i^2} \tag{4.21}$$

The perturbation bound for $\mathbf{L} = \mathbf{I}$ is [2]:

$$\frac{\|x^{exact} - x_\lambda\|_2}{\|x_\lambda\|_2} \leq \frac{\sigma_1}{\lambda} \frac{\|e\|_2}{\|\mathbf{A}x_\lambda\|_2} \tag{4.22}$$

The error boundary in Tikhonov regularization depends on the regularization parameter. When λ is large, the solution is determined by the large component of singular values. Therefore, due to the elimination of high frequency components, the solution is "over-smoothed". For small values of λ, the filter factors are nearly equal to 1. Consequently, the solution is "under-smoothed" and converges to the naive solution.

4.4.1.3 Parameter Selection for Spectral Filtering

In the spectral filtering, selection of the regularization parameter value plays an important role. For calculating the truncation parameter in TSVD, the discrete Picard condition, L-curve, and the generalized cross validation (GCV) are the most well known techniques, respectively. In Tikhonov regularization, λ is generally selected by using L-curve. The other techniques such as generalized cross validation, and the discrepancy principle can be used as well.

In the discrete Picard condition, the coefficient $u_i^T b$ and the singular value σ_i are compared [47]. Their ratio $u_i^T b/\sigma_i$ is the weight of the image space vectors (4.15). When the measurement is perturbed by the noise, the small singular values amplifies the noise and the solution becomes irrelevant (Figure 4.11-a). The Picard plot of the model is illustrated in Figure 4.13. In addition to the numerical noise, 1% Gaussian white noise is added to the measurement. As seen in the plot, the coefficient of v_i's increases dramatically for k value higher than 600 and the noise dominates the measurement. Therefore, the truncation parameter k should be lower than 600 in order to get the regularized solution.

In the L-curve method, the norm of the regularization solution $\|x_{reg}\|_2$ versus the norm of the residual error $\|\mathbf{A}x_{reg} - b\|_2$ are plotted [48]. For the ill-posed problem, the plot is given in log-log scale and it has L-shaped characteristic. When the filter factor is small, the solution is close to the naive solution. In this case, the norm of the regularization solution is high whereas the residual

error is nearly constant. Small filter factors corresponds to the vertical part of L-curve where the solution is 'under-smoothed'. For the high value of the filter factors, $\|x_{reg}\|_2$ is small and nearly constant and the residual norm increases by increasing the filter factors. This corresponds to the horizontal part of the L-curve where the solution is 'over-smoothed'. The curvature of the plot (corner of L) gives the optimum value of the regularization parameter.

The L-curves for TSVD and Tikhonov regularization are shown in Figure 4.13-b, and Figure 4.14-a, respectively. In the presence of 1% Gaussian noise, k should be between 360 and 720 and for Tikhonov regularization, the λ should be around 1e-15. The filter factors associated with different values of λ are give in Figure 4.14-b.

Figure 4.15 shows reconstructed images obtained for different truncation values considering the value provided by the L-curve and the Picard plot. The true conductivity perturbation is 0.1 S/m. Considering all reconstructed solutions, the truncation value of 487 is the best choice which is consistent with the obtained value from the parameter selection methods. In this case, the ratio of the lowest singular value (σ_k) to the highest (σ_0) one is 0.00018. This value corresponds to the SNR of 75 dB. The Tikhonov regularization results are given in Figure 4.16. The reconstructed image for $\lambda = 1e-15$ is in a good agreement with the true image.

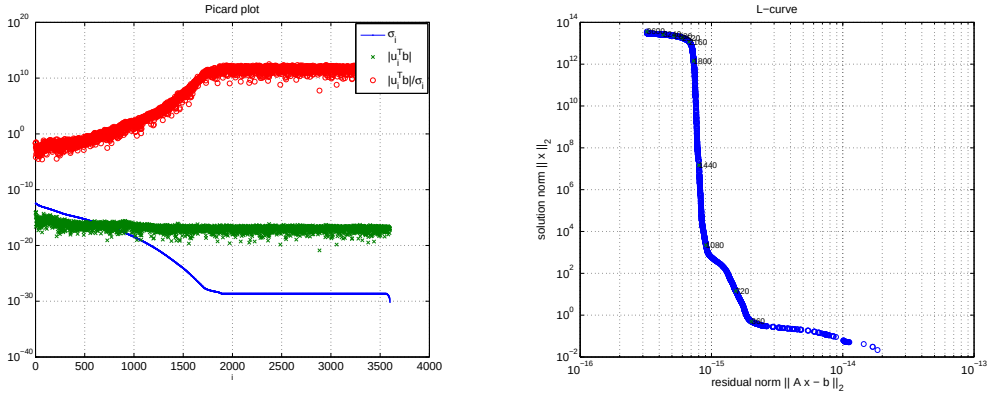

(a) (b)

Figure 4.13: Parameter selection for TSVD (a)discrete Picard plot (b)L-curve

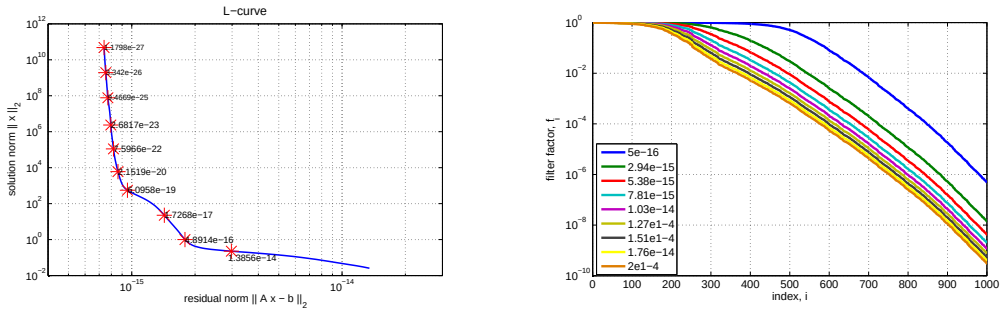

(a) (b)

Figure 4.14: (a) L-curve plot for Tikhonov regularization (b) Filter factors for different λ values

4.4.2 Iterative Algorithms

The method based on the singular value decomposition and the matrix inversion provides satisfactory results. However, as the dimension of the problem increases, the storage and computation time should be considered. Therefore, the method which does not require matrix factorization/inversion is more feasible for large scale problems. The iterative methods are proper choices for those cases.

In iterative methods, a sequence of the solution $x^{[0]} \rightarrow x^{[1]} \rightarrow x^{[2]} \rightarrow \cdots x^{[n]}$ is generated at each iteration from the matrix-vector multiplications. In these methods, iteration number is the regularization parameter. In the TSVD and Tikhonov requlrization the truncation number k and λ are the reqularization numbers, respectively.

Figure 4.19 shows the semi-converges behavior of the iterative methods. As iteration number increases, the solution converges to the exact solution. Then, the solution diverges from the exact solution and reaches to the naive solution. Therefore, these approaches have a semi-convergent behavior, and for optimum solution, the iteration should be stopped in the first region.
The gradient based iterative algorithms try to minimize the following quadratic

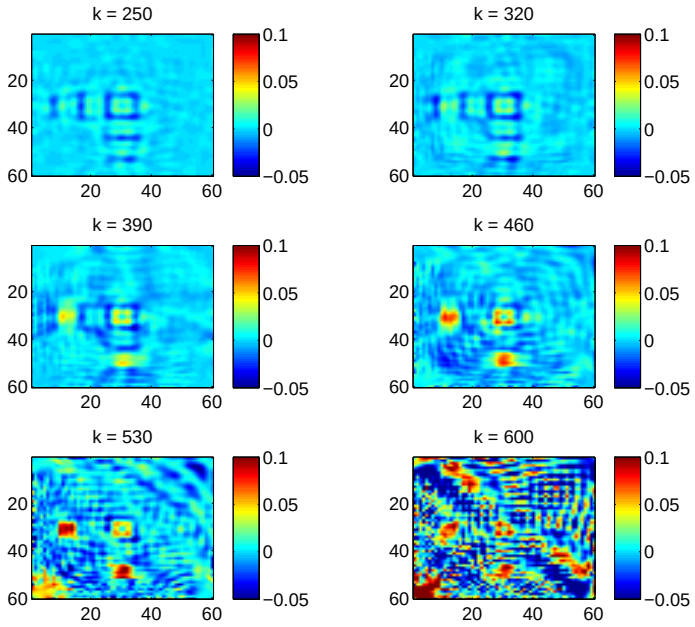

Figure 4.15: The reconstruction of the image by TSVD with different truncation values.

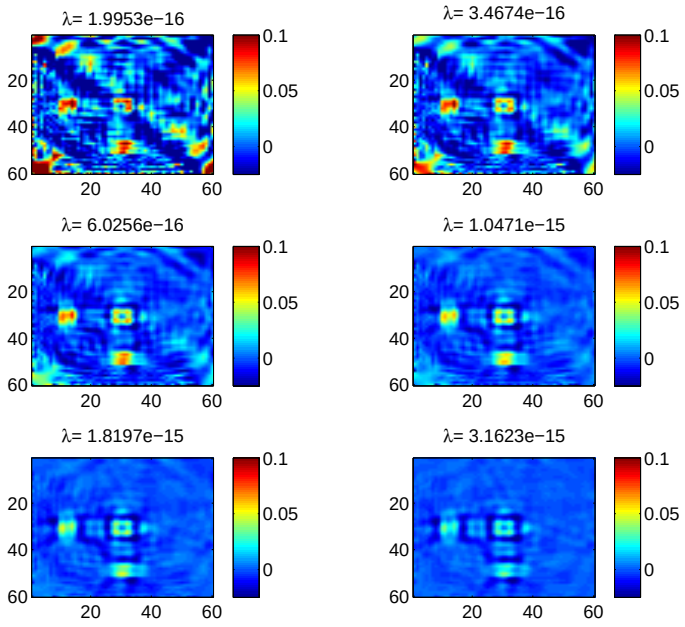

Figure 4.16: The reconstruction of the image by Tikhonov method with different λ values.

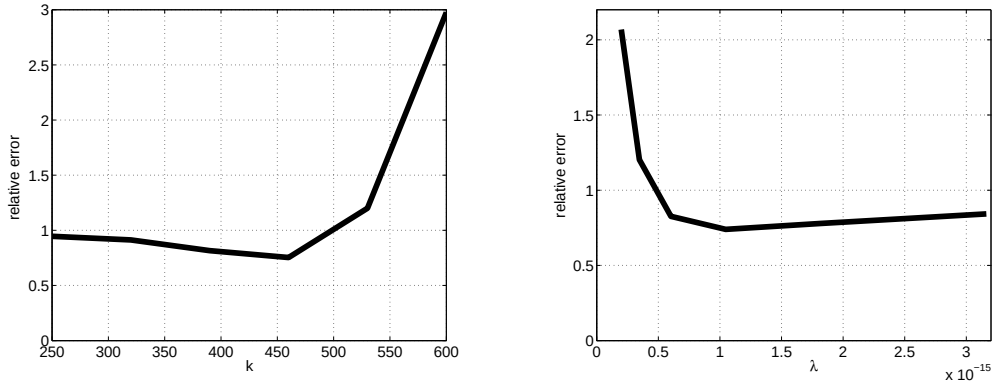

(a) (b)

Figure 4.17: relative error $\epsilon_r = \frac{\|\sigma_{exact} - \sigma_{reconstructed}\|}{\|\sigma_{exact}\|}$ with respect to (a) truncation number k in TSVD (b) regularization parameter λ for Tikhonov regularization

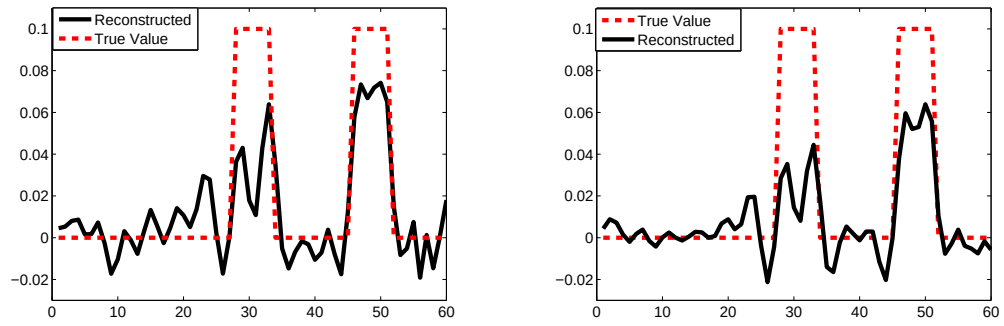

(a) (b)

Figure 4.18: Conductivity perturbation along x=0 (a) TSVD (k=460) (b) Tikhonov regularization ($\lambda = 1e-15$)

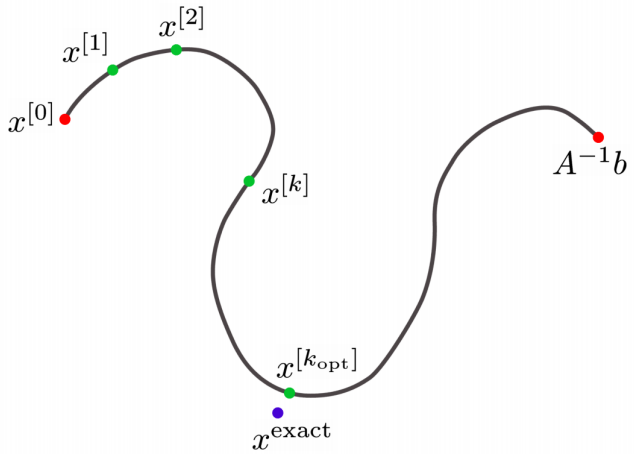

Figure 4.19: Semi-convergent behavior of the iterative methods [2].

cost function: $\phi : \mathbb{R}^n \to \mathbb{R}$:

$$\phi(x) = \frac{1}{2}\|\mathbf{A}x - b\|_2^2 \tag{4.23}$$

Minimization of the cost function starts with x^0 and proceeds iteratively:

$$x^{k+1} = x^k + \alpha_k d_k \tag{4.24}$$

where $d_k \in \mathbb{R}^n$ is the search direction and $\alpha_k \in \mathbb{R}$ is the step length. The search direction is determined, and the step length is calculated from it by solving one dimensional minimization problem.

$$\alpha_k = \arg\min_{\alpha} \left\{\phi(x^k + \alpha d_k)\right\} \tag{4.25}$$

4.4.2.1 Steepest Descent

The steepest descent algorithm selects the search direction as the negative gradient of the cost function $\phi(x)$. Due to the step length derived from one dimensional minimization problem given in 4.25, the consecutive search directions are orthogonal to each other. The error bound of the steepest descent algorithm can be determined using *Kantorovich inequality*. As given in (4.26), the error bound depends on the condition number of $\mathbf{A}^T\mathbf{A}$ i.e. $\kappa(\mathbf{A}^T\mathbf{A})$. Thus, convergence speed is slow for ill-conditioned matrix. As iteration number increases, it

Algorithm 1 Steepest Descent (SD) Algorithm

For initial choose of $x_0 \in \mathbb{R}^n$ and $d = \mathbf{A}^T(b - \mathbf{A}x_0)$, $i = 0$

while $\|d_i\|_2 \geq \epsilon$ **do**

$\alpha_i = \frac{\|d_i\|_2^2}{\|\mathbf{A}d_i\|_2^2}$

$x_{i+1} = x_i + \alpha_i d_i$

$d_i = \mathbf{A}^T(b - \mathbf{A}x_{i+1})$

$i = i + 1$

end while

zigzags around the local minimum point. Although its convergence behavior is poor, it is usually preferred because of its low computation cost.

$$\|e_{k+1}\| \leq \left(\frac{\kappa(\mathbf{A}^T\mathbf{A}) - 1}{\kappa(\mathbf{A}^T\mathbf{A}) - 1}\right) \|e_k\| \tag{4.26}$$

4.4.2.2 Conjugate Gradient

In the SD algorithm, the solution has a zigzag behavior because only the consecutive search directions are guaranteed to be orthogonal to each other. Therefore, the solution may not converge if the iteration number is infinitely large. The conjugate gradient (CG) algorithms are proposed to overcome this drawback. In this method, the proceeding search direction is chosen as "K conjugate" to the former search directions. In addition, it has been proven that CG converges at most in nth iteration for the n-dimensional problem if the solution space is in the nth dimensional Krylov subspace $K_n(K; b)$ [49].

$$K_n(K; b) = span\left\{b, Kb, K^2b, \ldots K^nb\right\} \tag{4.27}$$

The implementation of the CG is given in the Algorithm 2. The residuals $\{r_0, r_1, \cdots, r_{k-1}\}$ are the orthogonal and the search directions $\{p_0, p_1, \cdots, p_{k-1}\}$ are K-conjugate basis of K_n.

K should be a positive semi-definite (PSD) matrix. Since the sensitivity matrix is not a PSD matrix, equation (4.9) should be transformed into the following

Algorithm 2 Conjugate Gradient Algorithm

For a given positive semi-definite symmetric system of equation $\mathbf{Ax} = \mathbf{b}$ with initial solution $\mathbf{x}_0$ and $\beta_{-1} = 0$, $\mathbf{p}_{-1} = 0$, $\mathbf{r}_0 = \mathbf{b} - \mathbf{Ax}_0$, $i = 0$

while $\|\mathbf{r}_i\|_2 \geq \epsilon$ **do**

$\mathbf{p}_i = -\mathbf{r}_i + \beta_{i-1}\mathbf{p}_{i-1}$

$\alpha_i = \dfrac{\|\mathbf{r}_i\|_2^2}{\mathbf{p}_i^T \mathbf{A}\mathbf{p}_i}$

$\mathbf{x}_{i+1} = \mathbf{x}_i + \alpha_i \mathbf{p}_i$

$\mathbf{r}_{i+1} = \mathbf{r}_i + \alpha_i \mathbf{A}\mathbf{p}_i$

$\beta_{i+1} = \dfrac{\|\mathbf{r}_{i+1}\|_2^2}{\|\mathbf{r}_i\|_2^2}$

$i = i + 1$

end while

form by multiplying both sides of the equation with the transpose of the sensitivity matrix:

$$\mathbf{A}^*\mathbf{A}x = \mathbf{A}^*b \tag{4.28}$$

Regarding that modification, it is guaranteed that $\mathbf{K} = \mathbf{A}^*\mathbf{A}$ is a PSD matrix. In the case of noisy measurements, the solution goes to the naive solution as iteration number increases and at the nth iteration it will be far from the exact solution. Therefore, at each iteration the solution should be checked with Morozov's discrepancy principle [50].

The error bound for CG can be determined as done in the SD algorithm. As given in 4.29, this bound is proportional to the square root of the condition number of $\mathbf{A}$ [51]. Therefore, the CG converges faster than the SD algorithm.

$$\|e_{k+1}\| \leq \left(\frac{\sqrt{\kappa(\mathbf{A}^T\mathbf{A})} - 1}{\sqrt{\kappa(\mathbf{A}^T\mathbf{A})} - 1} \right) \|e_k\| \tag{4.29}$$

Even if the CG method converges at most in the nth iteration, it is not computationally efficient for large n values. Since the error bound is determined by the condition number of the matrix, too many iterations may be required for the convergence. In order to decrease the iteration number, the condition number of $\mathbf{K}$ can be decreased by preconditioning $\mathbf{A}$ with a preconditioner matrix $\mathbf{M}$.

4.4.2.3 Algebraic Reconstruction Technique (ART)

Algebraic Reconstruction Technique (ART) or Kaczmarz's iteration is a well-known method in the field of computerized tomography [52]. The method starts with an initial solution and in each step, the solution is projected into the hyperplanes defined by $< a_i, x >= b_i$. The vector a_i denotes the row of $\mathbf{A}^*$ and $b = \{b_1\ b_2\ \cdots\ b_m\}$. Therefore, the algorithm becomes:

$$x_{k+1} = x_k + \frac{b_i - < a_i, x >}{\|a_i\|_2^2} a_i \tag{4.30}$$

It is difficult to find the convergence rate of ART. However, as the consecutive rows of the $\mathbf{A}^*$ become independent from each other, the solution converges faster. According to the literature, using a_i in random order increases the convergence speed considerably [53]. In the randomized ART, the algorithm is adapted as:

$$x_{k+1} = x_k + \frac{b_{r(i)} - < a_{r(i)}, x >}{\|a_{r(i)}\|_2^2} a_{r(i)} \tag{4.31}$$

For the selection of $r(i)$, a $\{1, 2, 3, \cdots, n\}$ is constructed and each element of the set has the probability of $\|a_{r(i)}\|_2^2$. The error bound can be calculated only in the form of expectation. The average of the error is bounded by:

$$\mathbb{E}\|e_{k+1}\|_2^2 \leq \left(1 - \kappa(\mathbf{A})^{-2}\right) \|e_k\|_2^2 \tag{4.32}$$

4.4.2.4 Simultaneous Iterative Reconstruction Techniques (SIRT)

In the ART, in each iteration, the solution is projected into one hyperplane. In order to add the solution component related with each hyperplane, at least n iterations are required to project the solution into all hyperplanes. Also, this makes ART algorithm inappropriate for parallel computations. In the simultaneous iterative reconstruction techniques (SIRT), the solution can be projected to all hyperplanes in each iteration. The simplest and the oldest method is the Landweber's iteration which is in the form of [54]:

$$x_{k+1} = x_k + \lambda_k \mathbf{A}^T (b - \mathbf{A} x_k) \tag{4.33}$$

where λ_k is the relaxation parameter and for convergence $0 < \lambda_k < 2\|\mathbf{A}^T\mathbf{A}\|_2^{-2} = 2\sigma_1^{-1}$ must be satisfied. This method is a special form of the steepest descent

technique and it is widely used in the well-posed problems. Later, this algorithm was modified with a diagonal scaling matrix D to make it proper for ill-posed cases. It is called as Cimmino's iteration and it has the following form:

$$x_{k+1} = x_k + \lambda_k \mathbf{A}^T \mathbf{D}(b - \mathbf{A}x_k) \tag{4.34}$$

where $\mathbf{D} = diag(d_i)$ is a diagonal matrix and its elements are derived from the rows $a_i^T = \mathbf{A}(i,:)$ of A:

$$d_i = \begin{cases} \frac{1}{m}\frac{1}{\|a_i\|_2^2} & a_i \neq 0 \\ 0, & a_i = 0 \end{cases} \tag{4.35}$$

However, when the matrix $\mathbf{A}$ is sparse, only a few number of the a_i elements are nonzero. In large dimensional problems, dividing $\|a_i\|_2^2$ by the large number m makes the $< b - a_i x >$ contribution small. So, the algorithm is adapted for the sparse systems. The factor related to the sparsity of a_i is inserted in terms of $1/m$. This new method is called as "component averaging (CAV)" algorithm and it is different than Cimmino's iteration method due to the diagonal weighting matrix [55].

$$x_{k+1} = x_k + \lambda_k \mathbf{A}^T \mathbf{D}_S(b - \mathbf{A}x_k) \tag{4.36}$$

where $S = \{s_1, s_2, \cdots, s_n\}$ with s_i's defined as the number of nonzero elements in a_i and $\mathbf{D}_S = diag(d_{s_i})$, with entries of:

$$d_{S_i} = \frac{1}{\|a_i\|_S^2} \tag{4.37}$$

4.4.2.5 Results

To evaluate the performance of the iterative methods for LFEIT, steepest descent (SD), conjugate gradient least square (CGLS), randomized ART, and component averaging (CAV) methods are implemented (The implementation and documentation of fundemental iterative algorithms can found in [56]). The results are shown in Figures 4.20-4.25. As discussed above, the convergence behavior of SD is very poor because the singular values decays too fast. The randomized ART and CGLS converge faster than SD. They provide similar results with TSVD and Tikhonov methods up at 300 iterations. However, CAV

algortihm deesnot converge. Because SIRT algortihms has similar convergence behavior with SD.

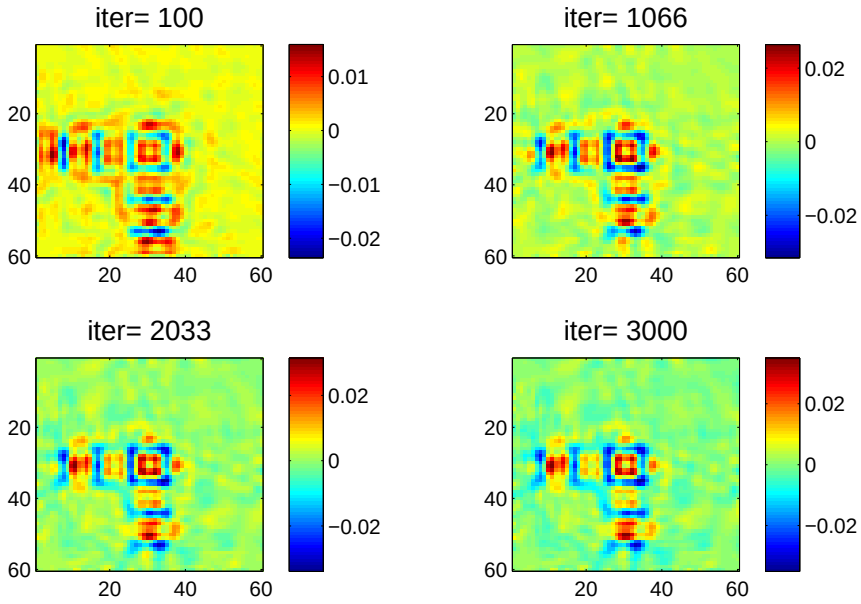

Figure 4.20: Result at different iteration number for reconstruction with the steepest descent methods

.

4.4.3 Sparse Regularization: L_1 norm minimization

In this study, the solution of the linear problem is the conductivity perturbation and it has a sparse distribution. As discussed above, the results of L_2 norm based regularization methods are nonzero coefficients even in the zero perturbation region. To remove the unwanted perturbations which correspond to the noise, a sparsity condition can be imposed to the cost function given in 4.23. This can be achieved by substituting L_1 norm constraint in the Tikhonov algorithm instead of L_2 norm constraint:

$$\min \|x\|_1 \quad \text{subject to} \quad \|\mathbf{A}x - b\|_2 \leq \delta \tag{4.38}$$

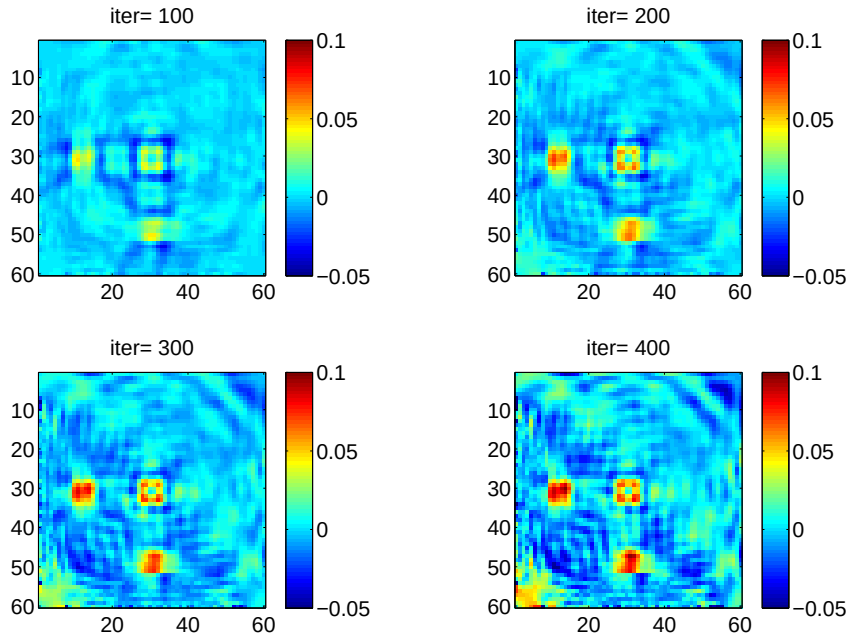

Figure 4.21: Result at different iteration number for reconstruction with conjugate gradient least square

.

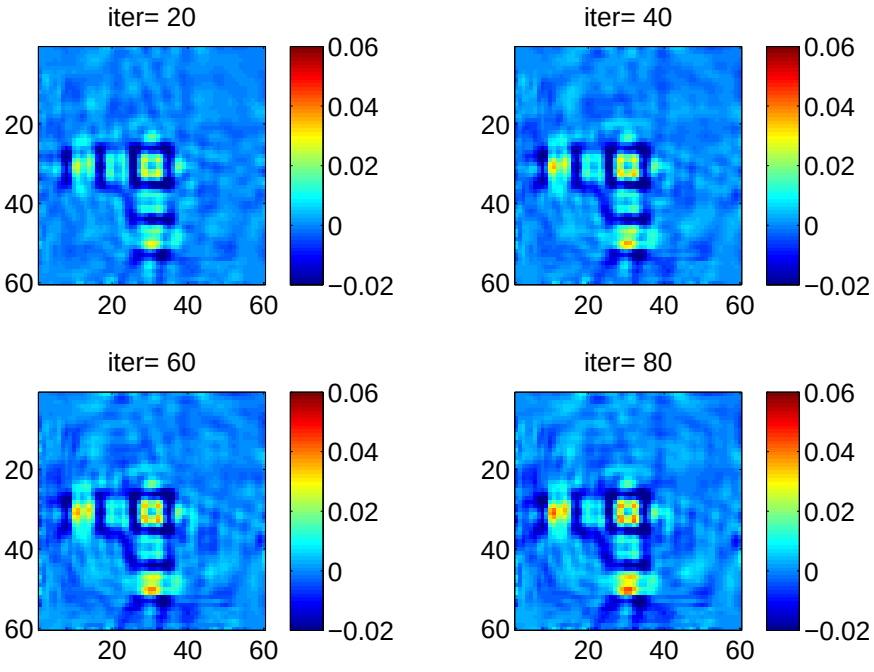

Figure 4.22: Result at different iteration number for reconstruction with randomized Kaczmarz algortihm

.

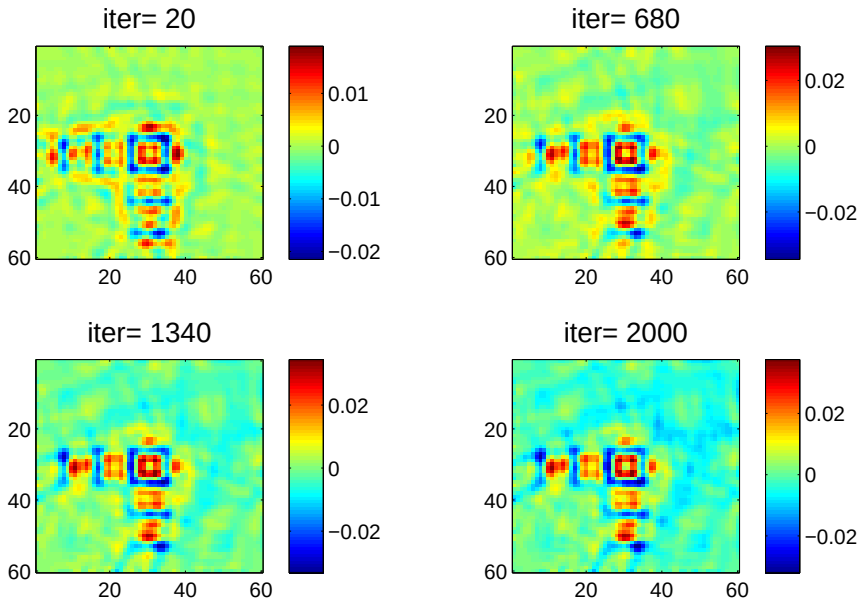

Figure 4.23: Result at different iteration number for reconstruction with component averaging

.

where δ is a nonzero priori value. As an example, Figure 4.26 explains the L_1 norm constraint. For the two-dimensional problem, the L_1 and L_2 constraints are shown as a square and a circle, respectively. While the least squares solution is dense, L_1 produces a sparse solution. In large dimensional problem the sparsity becomes more clear.

The constrain in the minimization problem 4.38 can be applied to the objective function by choosing a positive regularization parameter λ, similar to the Tikhonov regularization method. Therefore, the sparsity regularization becomes the minimization of L1 functional:

$$F(x) = \|Ax - b\|_2^2 + \lambda\|x\|_1 \tag{4.39}$$

The mentioned algorithms cannot be applied to the convex problem, directly. Because, the L1 term $\|x\|_1$ has a non-smooth behavior i.e. the derivative of x does not exist for zero value terms. For non-smooth case, the following approaches were proposed: iteratively reweighted least square (IRLS), l1-ls, gradient-projection for sparse reconstruction (GPRS), and Bregman iteration.

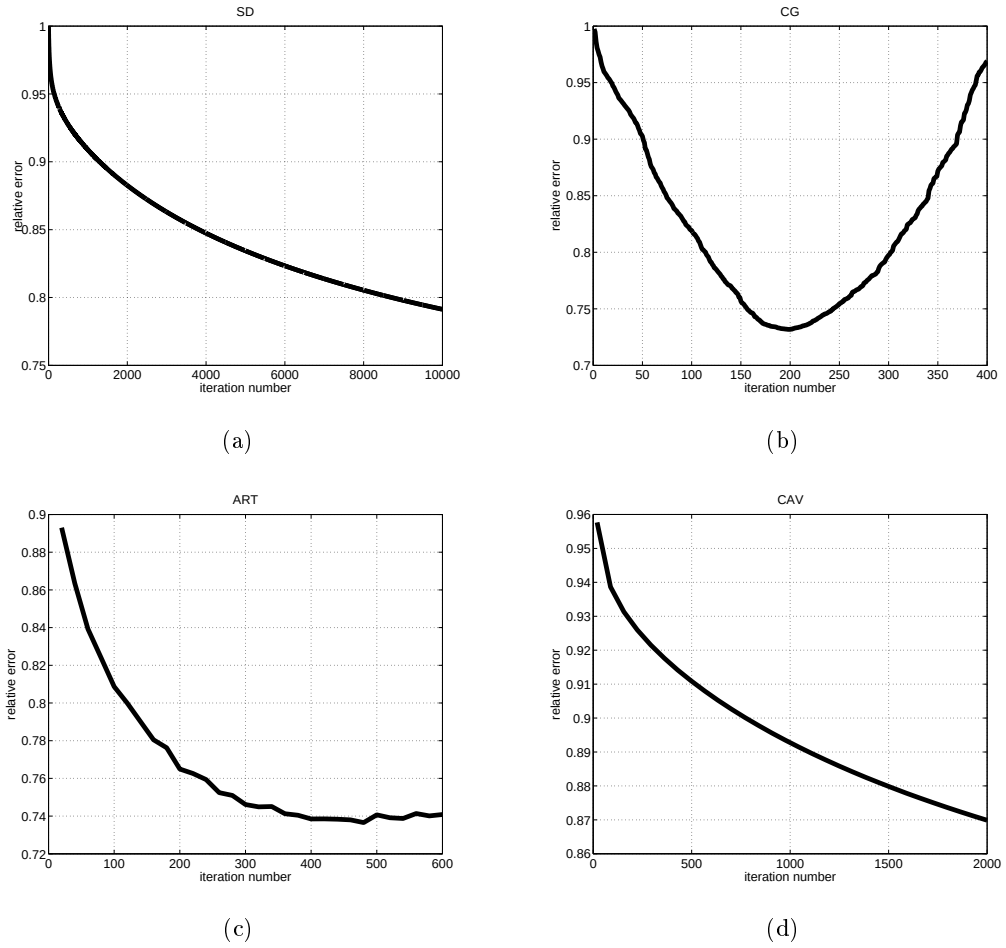

Figure 4.24: relative error $\epsilon_r = \frac{\|\sigma_{exact} - \sigma_{reconstructed}\|}{\|\sigma_{exact}\|}$ with respect to iteration number (a) Steepest Descent (b) Conjugate gradient least square (c) Randomized ART (d) Component Averaging.

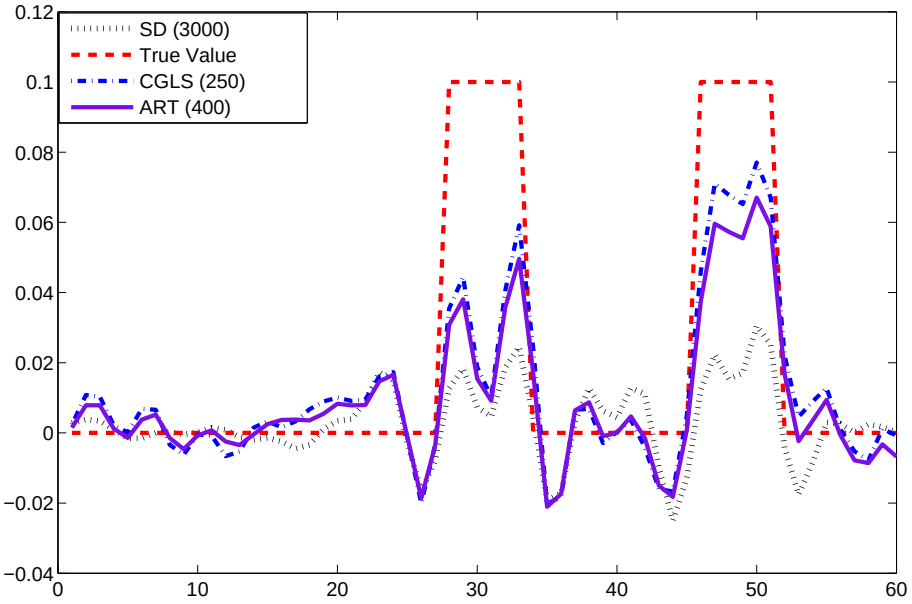

Figure 4.25: Conductivity perturbation along x=0 for different iterative algorithms. The iteration numbers are shown in the parenthesis

.

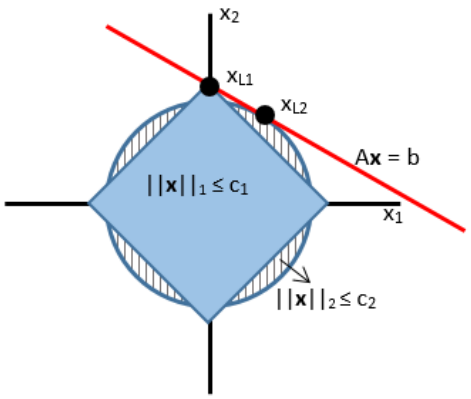

Figure 4.26: Geometric interpretation of the two-dimensional problem with L1 norm minimization (4.38). The square area shows the region $\|x\|_1 \leq c_1$, the circle shows the region with $\|x\|_2^2 \leq c_2$. In this 2-dimensional model space, an arbitrary constraint equation , $\mathbf{A}x - b = 0$, defines a line. The minimum 2-norm residual model satisfying the constraint, x_{L2}, will not generally be a sparse. However, due to the presence of corners in the L1-norm contour, the minimum L1-norm model satisfying the constraint, $x_{L1} = [0\ c1]^T$, tends to be a sparse.

.

In continue, these algorithms are explained, briefly.

4.4.3.1 Iteratively Reweighted Least Square (IRLS)

The IRLS algorithm deals with the gradient of the functional 4.39 at the points where x is differentiable.

$$\nabla F(x) = 2\mathbf{A}^T\mathbf{A}x - 2\mathbf{A}^T b + \lambda \sum_{i=1}^{m} \nabla |x_i| \tag{4.40}$$

The $\mathbf{W}$ is defined as a diagonal matrix with the elements

$$\mathbf{W}_{i,i} = \frac{1}{|x_i|} \tag{4.41}$$

The gradient of functional is written in the matrix multiplication format.

$$\nabla F(x) = 2\mathbf{A}^T\mathbf{A}x - 2\mathbf{A}^T b + \lambda \mathbf{W}x \tag{4.42}$$

Since $\mathbf{W}$ depends on the x, this is a nonlinear system equation. The final solution cannot be obtained, so for each iteration, a solution is determined. The elements of the diagonal matrix is calculated from the previous iteration results. To overcome the non-differentiability of x, a tolerance ϵ is defined.

$$\mathbf{W}_{i,i} = \begin{cases} 1/|x_i| & |x_i| \geq \epsilon \\ 1/\epsilon, & |x_i| \leq \epsilon \end{cases} \tag{4.43}$$

The solution for each iteration is determined by solving the following equation. The iteration proceeds until the convergence is achieved:

$$(2\mathbf{A}^T\mathbf{A} + \lambda \mathbf{W})x = 2\mathbf{A}^T b \tag{4.44}$$

In a large and sparse system case, it is better to write the problem in the form of least squares as in (4.45) and use the LSQR or other mentioned iterative methods.

$$\left\| \begin{bmatrix} \mathbf{A} \\ \sqrt{\frac{\lambda}{2}}\mathbf{W} \end{bmatrix} x - \begin{bmatrix} b \\ 0 \end{bmatrix} \right\|_2^2 \tag{4.45}$$

4.4.3.2 Iterative Shrinkage/Thresholding

In the Iterative Shrinkage/Thresholding (IST) algorithms, the format of 4.39 is changed and the problem is solved using the gradient projection methods. The algorithms is started with the matrix multiplication and is continued via shrinkage/thresholding [57]. The main step of the IST algorithms is:

$$x_{k+1} = T_{\lambda t_k}\left(x_k - 2t_k A^T(\mathbf{A}x_k - b)\right) \tag{4.46}$$

where t is the step length and T is the shrinkage operator defined as:

$$T_\alpha(x)_i = (|x_i| - \alpha))_+ \, sgn(x_i) \tag{4.47}$$

For convergence of x_k to the optimum solution of (4.39), the step length t_k should be bounded by the 0 and $1/\|\mathbf{A}^T\mathbf{A}\|$ i.e. $t_k \in (0, 1/\|\mathbf{A}^T\mathbf{A}\|)$.

In IST algorithms, the convergence rate depends on the system matrix $\mathbf{A}$. These algorithms are too slow when $\mathbf{A}$ is heavily ill-conditioned. to overcome this drawback, two-step iterative shrinkage/thresholding (TwIST) was proposed [58]. In TwIST, the proceeding iteration x_{k+1} is obtained from both x_k and x_{k-1}. So, the iteration becomes:

$$x_k = T_{\lambda t_k}\left(x_0 - 2t_k \mathbf{A}^T(\mathbf{A}x_0 - b)\right) \tag{4.48}$$

$$x_{k+1} = (1-\alpha)x_{k-1} + (\alpha - \beta)x_k + \beta T_{\lambda t_k}\left(x_k - 2t_k A^T(\mathbf{A}x_k - b)\right) \tag{4.49}$$

where α and β are the internal parameters of the algorithm which result in the convergence for a specific bound [58].

4.4.3.3 Results

In Figure 4.27 and 4.28 simulation results for 1% noise level are shown. The regularization parameter of IRLS λ is selected from L-curve plot given in Figure 4.14. At the first iteration, the result is same as Tikhonov regularization. There

exists nonzero coefficients in the region where the perturbation is zero. As iteration of IRLS proceeded, the sparsity of the solution increases. Therefore, the reconstructed values are close to the real values.

In TwIST algorithm, the step length t_k is chosen as $0.1/\|\mathbf{A}^T\mathbf{A}\|$. The regularization parameter λ is the most critical parameter. If it is too large, the optimum solution of x goes to zero; and if it is too small, the solution tends to converge least square solution. The condition on convergence (optimal solution is zero) is given [59] as:

$$\lambda \geq \lambda_{max} = \|2A^T b\|_\infty \tag{4.50}$$

where $\|x\|_\infty = \max_i |x_i|$ corresponds to the l_∞ norm of x. In Figure 4.28, the results for different λ values are shown. As λ increases, the sparsity of the solution increases. The optimal value of λ is found as $3e-5\lambda_{max}$. If the priori information given as the conductivity perturbation is nonnegative, the nonnegativity constraint can be imposed. This can done by equalizing the negative values to zero. Therefore, the solution will be more close the true values as shown in one dimensional plot in Figure 4.30.

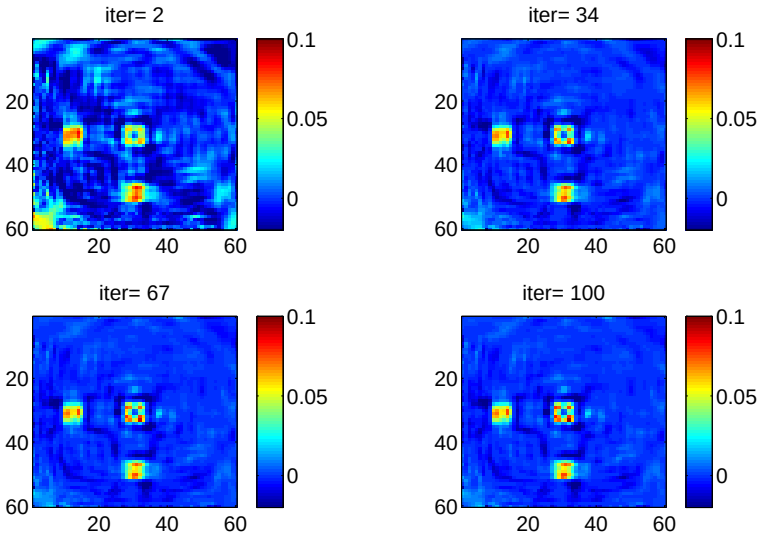

Figure 4.27: Result at different iteration number for reconstruction with iteratively reweighted least square algorithm($\lambda = 5e-31$)

.

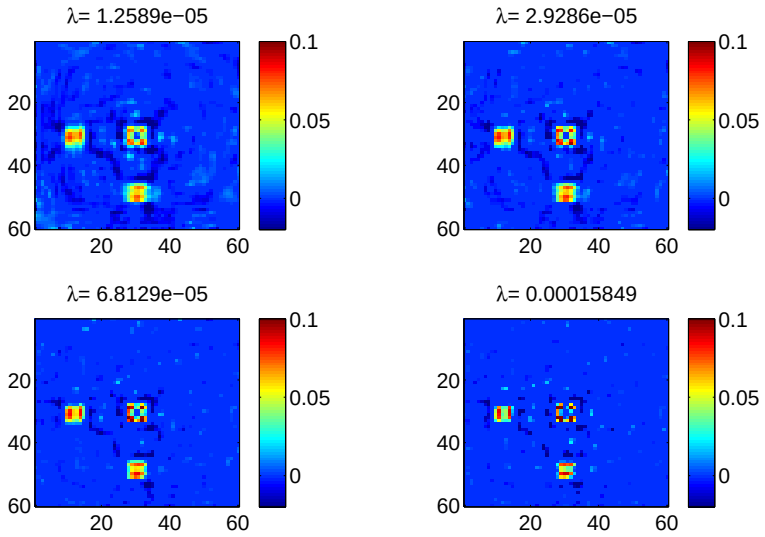

Figure 4.28: Two-step iterative shrinkage thresholding (TwIST) with different regularization parameters

.

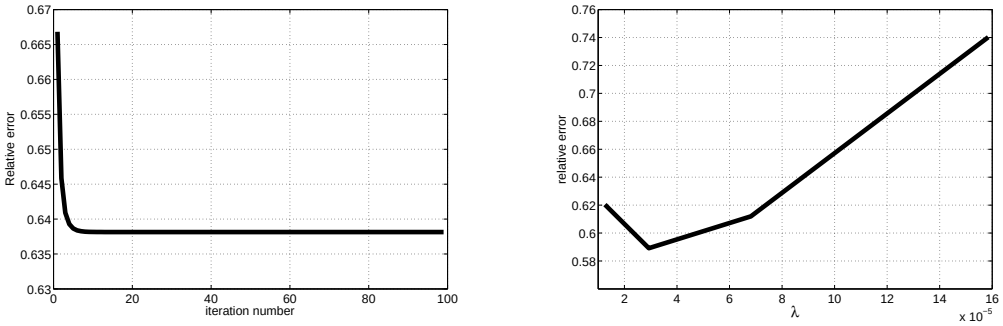

(a) (b)

Figure 4.29: Relative error (a) vs iteration number in IRLS ($\lambda = 5e-31$) (b) vs regularization parameter in TwIST

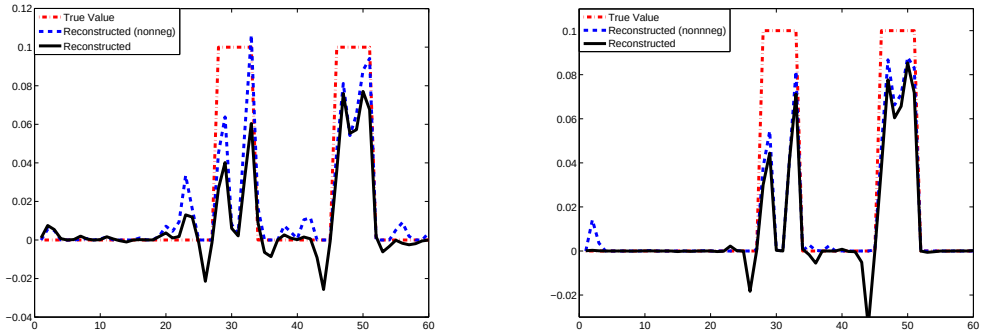

(a) (b)

Figure 4.30: Conductivity perturbation along x=0 (a) IRLS (iter=100) (b) TwIST ($\lambda = 3e-5\lambda_{max}$)

CHAPTER 5

INITIAL EXPERIMENT FOR LFEIT

5.1 Experimental Setup

In this section the description of the LFEIT experimental setup is given. The feasibility of the LFEIT method is evaluated by means of the setup shown in Figure-5.1. A burst signal is generated from the signal generator to feed the ultrasound (US) transducer. The generated burst signal is amplified with a high-power RF amplifier (Amplifier Research 150A100B) with 52 dB gain. A single element unfocused immersion type (Olympus V-303-SU) US is employed to produce the US excitation. The US wave produces movement in the particles of the medium. The selected medium is a cylindrical glass tube with a height of 10 cm and diameter of 2.5 cm. The upper half of the glass mold is filled with sunflower oil and the lower part is filled with the saline water. The sample mold is placed in the static magnetic field. Since the conductivities of the saline water and oil are different from each other, a velocity current distribution is induced in the z-directional boundary between them. A receiver coil is inserted in the same direction of the static magnetic field to sense the magnetic flux density variation of this current. The received signal is amplified and filtered with a custom made amplifier. The filtered signal is amplified more with a commercial wide-band low noise amplifier (Miteq AU-1291).

In the following sections, each block of the setup is explained with details and the set up evaluation results are given.

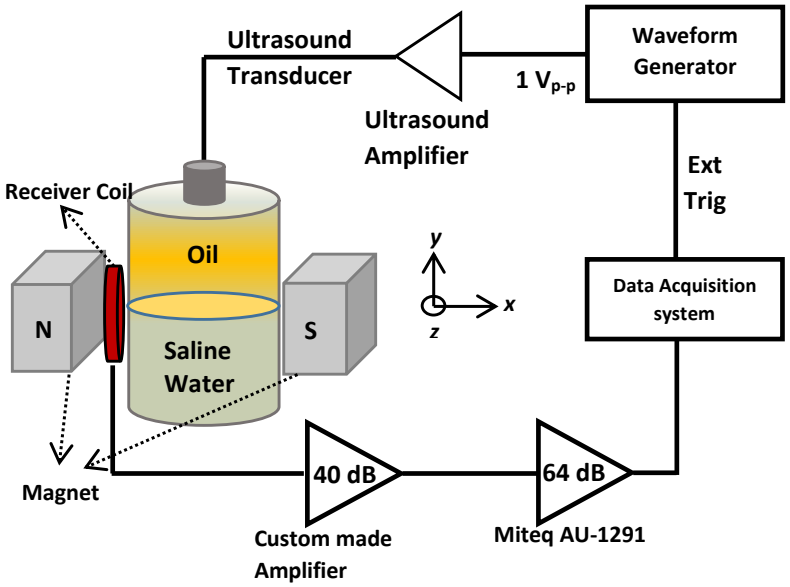

Figure 5.1: Schematic of the experimental setup

5.2 Ultrasound Transducer

To generate a particle movement inside the medium an immersion type unfocused ultrasound transducer (Olympus A-303-SU) is used. To acquire the pressure pattern of the transducer, a needle hydrophone (Onda Corporation, CA, USA) in the METU ULTRAMEMS laboratory of Electrical and Electronics Engineering Department was used [60]. The measurement which is done for 10 Volt peak-to-peak excitation are provided in the Figure-5.2. The maximum pressure of 0.02 MPa is measured at 1 MHz excitation.

5.3 Magnetic Field

The amplitude of the received signal from the receiver coil is proportional to the strength of the magnetic field. Therefore, creating the strong and homogeneous magnetic field is essential in the experiment. A neodymium magnet (NdFeB) N42 type is chosen to create such a field. This type of magnet can be easily

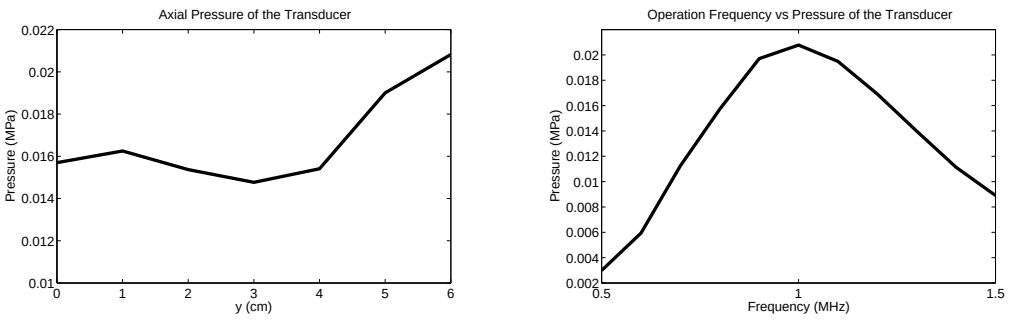

(a) (b)

Figure 5.2: The pressure pattern of the transducer for 10V peak-to-peak excitation. (a) Axial pressure at 1MHz (b) pressure vs frequency at the distance of 6 cm from transducer

assembled and has a strong permanent magnet behavior which is shown in Table-5.1 [61].

Table5.1: Characteristic of NDFeB N42

Characteristic	units	min	Nominal	maximum
Remanent flux density (Br)	mT	1280	1300	1320
Coercivity (HcB)	kA/m	867	935	1003
Intrinsic Coercivity (HcJ)	kA/m	955		

The strongest current density should be developed in the oil-saline interface. The width of the induced current density should be same as the diameter of the ultrasound probe. Therefore, the distance between N and S poles of the magnet can be decreased up to the transducer diameter by choosing an appropriate cylindrical tube. Since the detectable current density is developed at the conductivity interface, a small magnet is chosen. In addition, the small magnets are more available and assembling them is easier. Four pieces of $40 \times 20 \times 10$ mm magnet are used to create the field. In order to keep them stable, two plastic box of $40 \times 20 \times 20$ mm are produced and inserted into the main plastic box via adjustable screws (Figure-5.3). The gap length between each box can be arranged according to the size of the tube and the coil.

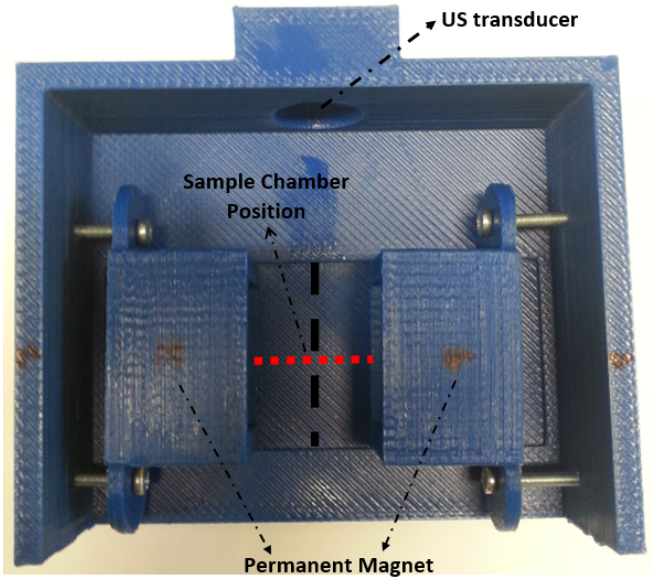

Figure 5.3: The permanent magnet system. The red line and black line represent the lateral and axial direction of transducer, respectively.

The distribution of the field in the gap was measured when the poles are placed 2.7 cm a way from each other. The measurements were performed by a calibrated Gauss meter (F.W. Bell 5180, 0.1 mT to 3 T) along two different lines. First scan line is along x-direction at the center of magnets or the lateral direction, and the second line is the axial direction of the transducer. The scan results are given in Figure-5.4 as dashed line. Same model is simulated in COMSOL Multyphysics. The model is simulated with coercivity of 900 kA/m. At the center of the magnets, the flux density is 0.2 Tesla (2 kG). Its amplitude decreases along the lateral direction and increases along the axial direction.

5.4 Test Chamber

A Plexiglas test tube of 22 mm diameter and 100 mm in height is used as a test chamber. Its opening has the same diameter with the ultrasound transducer. In order to form an interface which separate mediums of different conductivities, the sunflower oil and saline water are poured into the tube. The oil is chosen as one of the mediums:

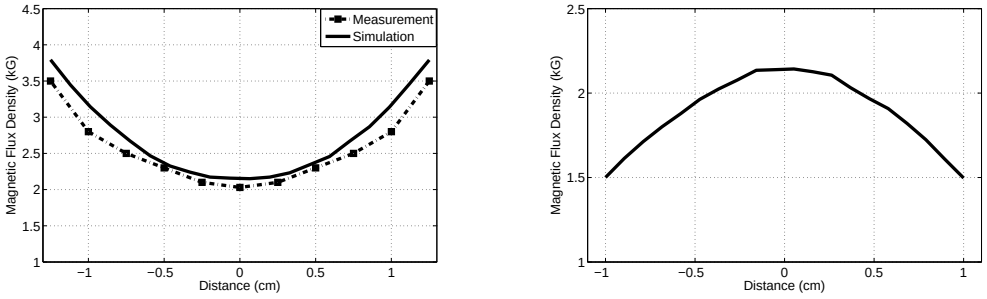

(a) (b)

Figure 5.4: Measured and simulated profile of the magnetic flux density at the center of magnets along (a) lateral and (b) axial directions.

i-) To obtain a higher signal amplitude, the reflection at the interface should be low. As shown in Table-5.2, the oil has similar acoustic properties to the water, so the reflection from the interface will be less.

ii-) The boundary formed between each medium should be smooth to avoid the reflections due to angular incidence of the ultrasound wave. Oil does not dissolve in water and it has lower mass density comparing the water. If the tube placed vertical, a perpendicular interface forms easily.

iii-) The conductivity of the oil is very low ($(2-10)\times 10^{-9}$S/m . If it is used in addition to saline water (2-4 S/m), a high conductivity gradient can be obtained at the interface.

Table5.2: Acoustic and electrical properties of the oil in comparison with the saline water.

Material	Saline Water	Oil
Mass density (kg/m^3)	1000	920
Speed of sound (m/s)	1482	1470
Acoustic impedance $(MRayls)$	1.482	1.352
Conductivity (S/m)	2-4	$(2-10)\times 10^{-9}$

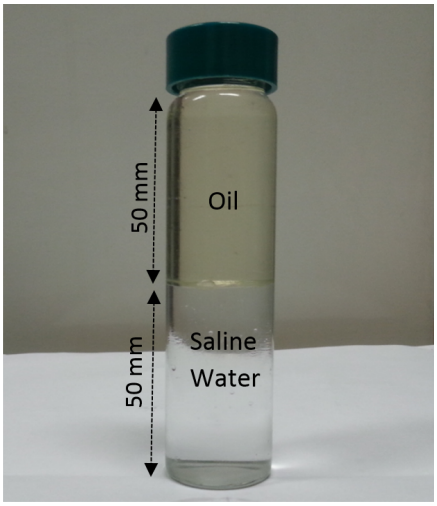

Figure 5.5: Test chamber filled with oil and saline water.

5.5 Amplifier

A burst sinusoidal shown in Figure 5.6-a is used as the excitation signal to protect the US transducer. In addition, during the burst signal excitation, there exists a large signal as given in Figure 5.6-b at the output of the RF power amplifier which has similar characteristic in time and frequency domain. If a long pulse is used, the radiation from the output of the RF power amplifier will dominate the LFEIT signal. Io avoid such interferences, the excitation should not occur while the ultrasound wave is passing through any interface. Therefore, a short burst pulse should feed the transducer. 1 MHz, 5 cycle burst sinusoidal with pulse repetition period of 1 ms is considered for the experiment.

The pressure wave developed inside the medium and the excitation signal are similar. Thus, the induced voltage in the coil is also a burst sinusoidal. To detect the voltage in the coil by an oscilloscope or data acquisition card, it should be amplified with a high gain factor. Since the signal is very weak and the noise can suppresses it, the amplifier and the filter should be selected carefully. The frequency characteristic of the given excitation signal is shown in Figure-5.7. To suppress the irrelevant frequency component, the signal should be filtered by a band-pass filter which has cut-off frequencies of 0.7 and 1.4 MHz. As discussed

in Section 3.4.1, by decreasing the bandwidth of the amplifier, the minimum detectable voltage is also decreased.

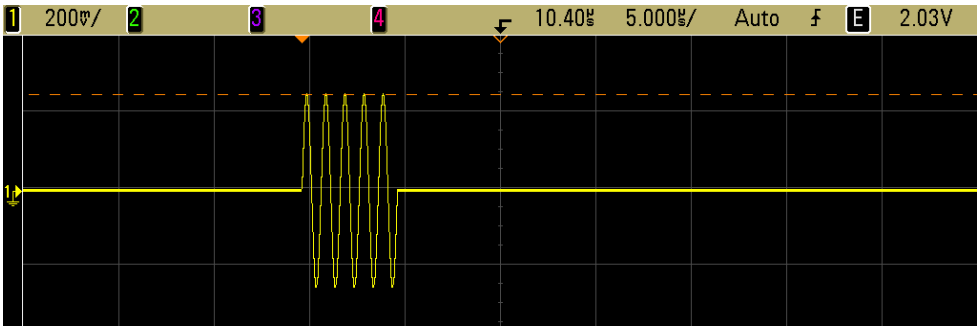

(a)

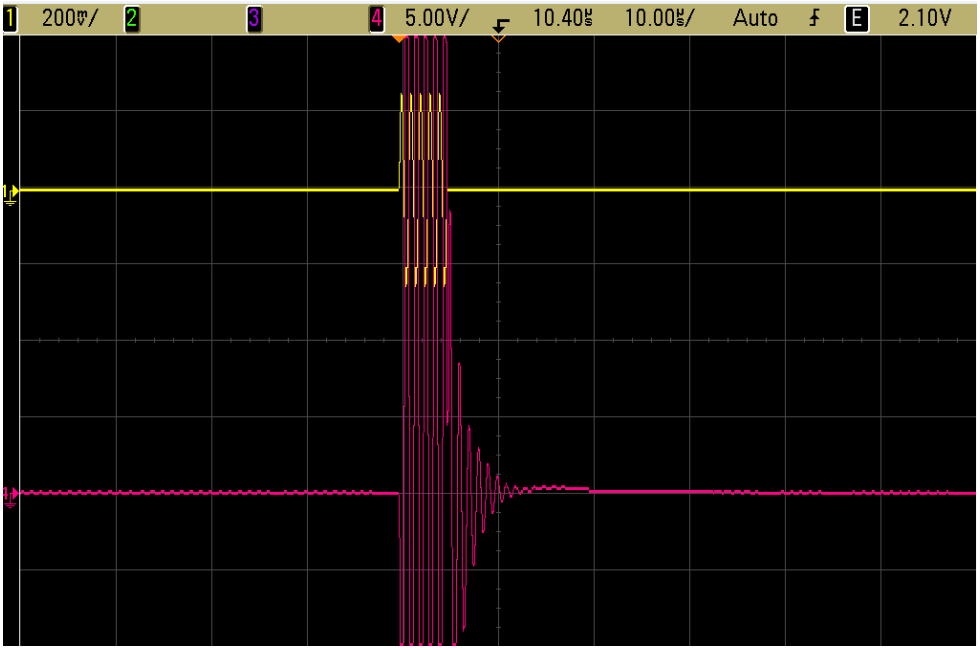

(b)

Figure 5.6: (a) 5 cycle 1 MHz burst sinusoidal excitation signal (b) The signal at the output of the RF power amplifier is shown below of the burst excitation

The proper amplifier should have a good noise characteristics. Among the commercially available options, Miteq AU-1291 is one of the best choices. Its noise figure is 1.6 dB and it has 64 dB gain. It operates between 0.01 MHz and 500 MHz [62]. The input impedance of this amplifier is measured as 75 Ω. Since the signal is very weak, further amplification is needed. A custom-made amplifier

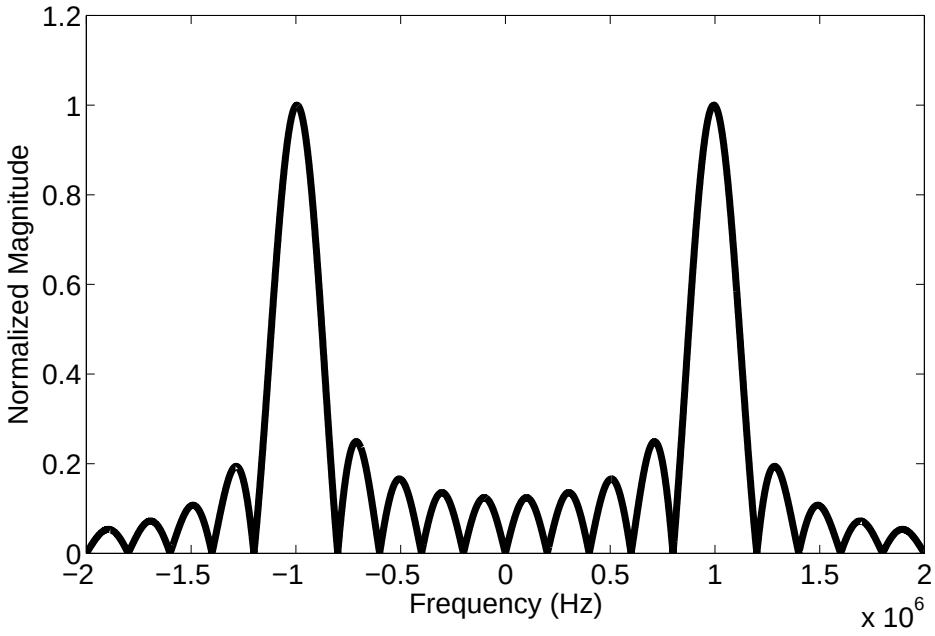

Figure 5.7: Normalized Fourier transform magnitude of 1 MHz, 5 cycle burst sinusoidal with 1 ms pulse repetition interval.

with a filter block is designed by AD600JN amplifier. The amplifier section of the experimental set up is given in Figure-5.8. AD600JN is a low noise, wideband variable gain amplifier. Its characteristics is given below [63]:

i-) Input impedance: 100 Ω. Output impedance: 2 Ω

ii-) Noise figure: 5.3 dB

iii-) Input noise spectral density : 1.4 $nV/\sqrt{(Hz)}$

iv-) 0 to 40 dB gain and DC to 35 MHz bandwidth

The gain of AD600JN is adjusted by the applied voltage to pin 16. The cut-off frequency of the filter is set by R1 and C1 components. Since the input impedance of the AU-1291 is low, TL072 is used as a buffer to prevent the loading effect. The gain characteristic of the amplifier stage is given in Figure-5.9. As it can be seen in this figure, the gain is 102 dB around 1 MHz. Further amplification adds too much distortion to the output. A low pass filter is not implemented, because the TL072 and AD600JN attenuate the signal at frequencies higher than 1 MHz. Therefore, they behave as a low filter with cut-off

frequency between 1-2 MHz.

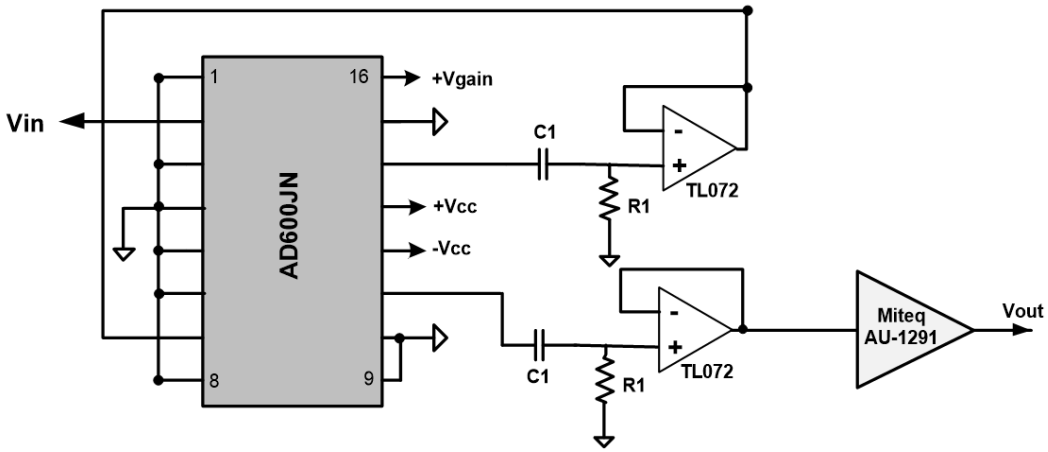

Figure 5.8: Schematic of the voltage amplifier.

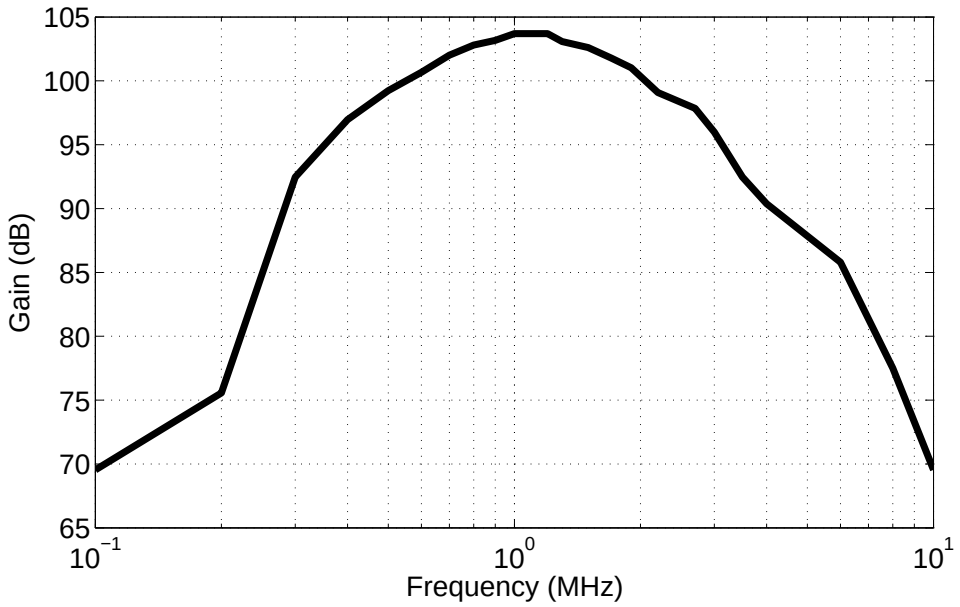

Figure 5.9: Gain vs frequency of the two stage amplifier.

5.6 Induction Coil Sensor

An multilayer air coil sensor is used to measure the time dependent magnetic flux density. These types of coil sensor have advantages of design simplicity, high turn numbers, linear response. Since the voltage induced in the coil has same frequency and spatial distribution with the pressure wave generated inside the medium, it should have the following properties:

i-) To acquire the maximum voltage the resonance frequency should be around 1 MHz.
ii-) To increase the sensitivity of the coil, the size of coil should not be much higher than the lateral length of the ultrasound wave. Because the magnetic flux density generated inside the medium is weak at the region where the pressure is low.

The coil shown in Figure 5.10 satisfies the mentioned criteria. The design rule and parameter selection such induction coil are given in [64]. The radius of the sensor is 1 cm and this value corresponds to the 7 wavelength. Since 5 cycle excitation is applied to the transducer, the sensitivity of sensor will be high. The inductance (@1MHz) and the resistance are measured as 25μH and 0.2 Ω.

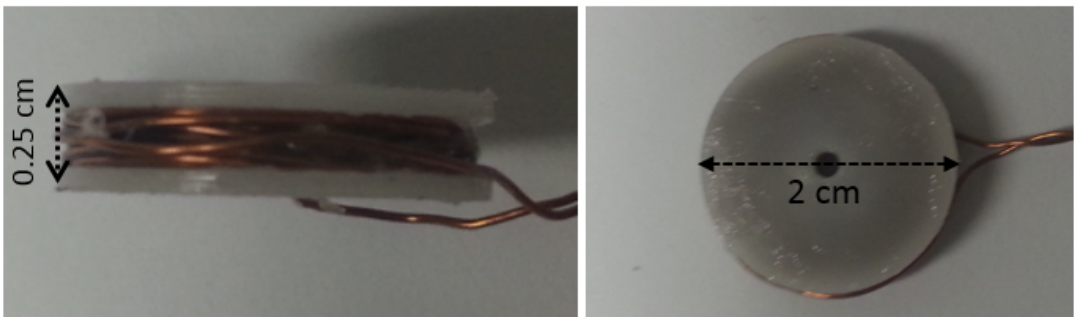

Figure 5.10: Side (left) and top (right) view of the induction coil sensor. The length of the coil is 0.25 cm and diameter is 2 cm. The number of the turns,N, is 70.

To acquire the induced voltage, the induction coil is connected to a voltage amplifier. Since the coil has the internal resistance R, inductance L and self-capacitance C, the voltage at the input of the amplifier depends on the frequency. Moreover, the amplifier has an internal resistance Ri and capacitance Ci. To determine the transfer function $H(\omega)$ between the induced voltage Vind and the voltage at the input of the amplifier Vi, an equivalent circuit is given in Figure 5.11. $H(\omega)$ can be expressed as:

$$\frac{V_i(\omega)}{V_{ind}(\omega)} = H(\omega) = \frac{K}{1 - (\frac{\omega}{\omega_r})^2 + i2D\frac{\omega}{\omega_r}} \tag{5.1}$$

where K is a voltage division factor:

$$K = \frac{R_i}{R + R_i} \tag{5.2}$$

and ω_r is the resonant angular frequency

$$\omega_r = \frac{1}{\sqrt{KLC_T}} \tag{5.3}$$

where C_T is the equivalent capacitance, $C_T = C + Ci$. The damping of the resonant circuit is represented as D, and it is further expanded as:

$$D = \frac{\sqrt{K}}{2}\left(\frac{\sqrt{\frac{L}{C_T}}}{R_i} + \frac{R}{\sqrt{\frac{L}{C_T}}}\right) \tag{5.4}$$

Since $R << R_i$ and the inductance L is much grater than C_T, K can be assumed to be 1 and D becomes:

$$D = \frac{\sqrt{\frac{L}{C_T}}}{2R_i} \tag{5.5}$$

If the sensor is tuned to resonance frequency, then $H(\omega)$ becomes:

$$H(\omega_r) = \frac{R_i}{\sqrt{\frac{L}{C_T}}} \tag{5.6}$$

5.7 Results and Discussion

Experiments are performed with a given setup in Figure 5.1. The excitation signal is a 5 cycles 1 MHz burst sinusoidal with the pulse repetition rate of 500μs.

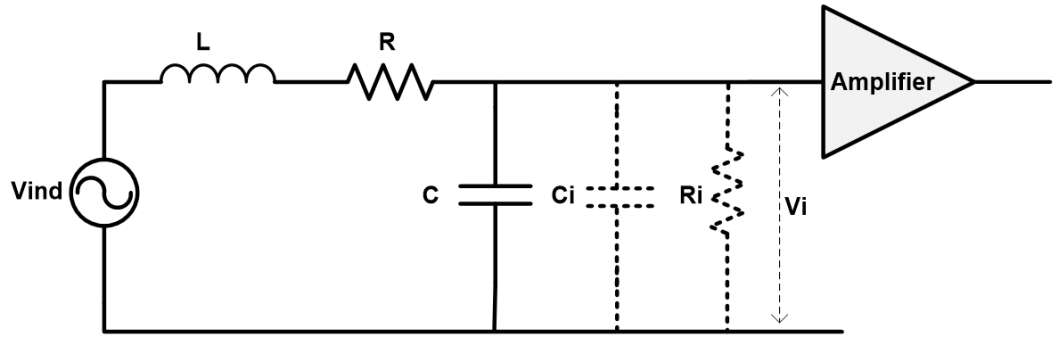

Figure 5.11: Equivalent circuit of the induction coil sensor loaded with amplifier internal capacitance (Ci) and internal resistance (Ri). L, R, C are inductance, resistance and capacitance of the coil. Vind is the induced voltage and Vi is the voltage at the input of the amplifier

The received signal and the signal at the output of the RF power amplifier are acquired by a digital oscilloscope. The result is given in Figure 5.13. The channel 4 (purple) shows the signal received by the induction coil sensor. At three time instants, a nonzero signal is observed. At time zero, the radiation from the output of the RF power amplifier is observed. At the second and the third time instants, the pulse echo signals coming from oil-water and water-glass interfaces are observed. Since the acoustic impedance of the oil and water are different from each other, the incident pressure wave is reflected from the boundary (4.5% of the incident wave is reflected from oil-water interface). The reflected pressure wave generates a voltage at the input of the transducer because of direct piezoelectric effect. To understand whether it is pulse echo signal or not, the output of the RF power amplifier is observed at the channel of the oscilloscope. Existing at the same time and having similar shapes verify that they are pulse-echo signals. The LFEIT signal is expected to exist at the half time of the pulse-echo signal coming from the oil-water interface. However, there was not any distinguishable LFEIT signal because the noise level is high. The reasons can be listed as:

i-) The maximum allowed voltage level in the input of US transducer is 300 V_{p-p}.

The pressure developed in the medium is 0.6 MPa.
ii-) The thermal noise level of the receiver is 0.5 μV, approximately.
iii-) The strength of the static magnetic field is low.

To detect the LFEIT signal, the signal level should be higher than the thermal noise level. Therefore,

i-) A US transducer which can develop higher pressure should be used.
ii-) Since neodymium magnets cannot produce high static magnetic field, a magnet similar to in the magnetic resonance imaging system should be utilized.
iii-) The noise figure of the receiver system should be lower.
iv-) The sensitivity of the receiver coil should be increased or low-noise coil should be designed.

Instead of induction coil, an electrode pair can be used for measurement [26], [29] (Figure 5.12). The electrode pair should be placed in the direction of the velocity current flow. During the experimental study of LFEIT, a sample chamber which has strip electrode is used and the results are shown in Figure 5.14-5.15. The LFEIT signal is detectable in this configuration because the velocity current tends to flow on the surface of the electrodes. The measurement taken from the electrode pair is given in Figure 5.16. The signal power is lower than the coil measurement. Even if the observed signals are not the LFEIT signals, they are related to the velocity current distribution. Therefore, they should be investigated in a future study.

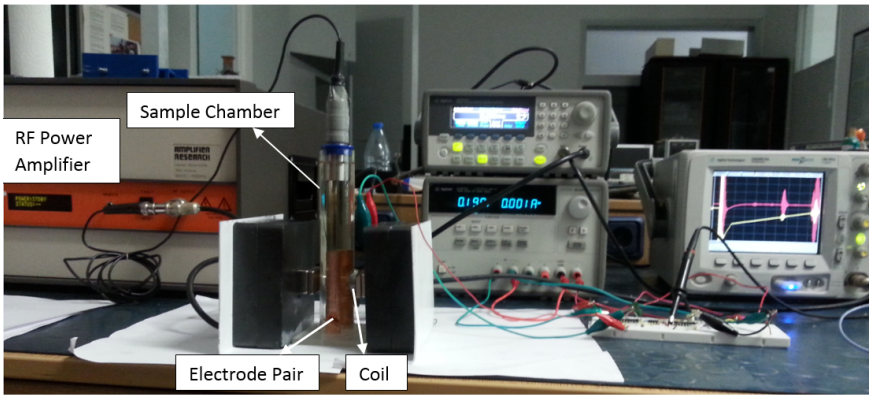

Figure 5.12: Experiment setup for the electrode measurement. The coil is placed to sense the magnetic flux density of current distribution on the electrode surface.

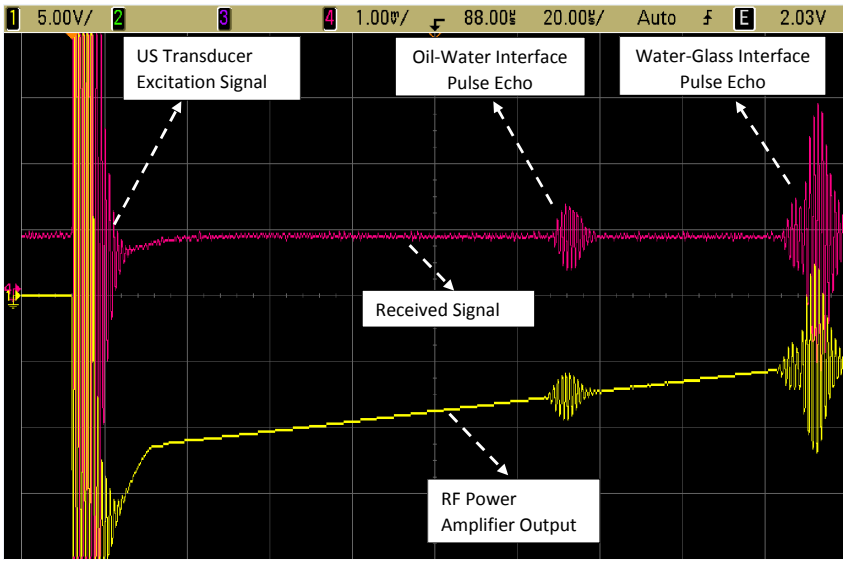

Figure 5.13: The received signal (purple) and the signal at the output of the RF power amplifier (yellow). The excitation is 5 cycles 1 MHz burst sinusoidal.

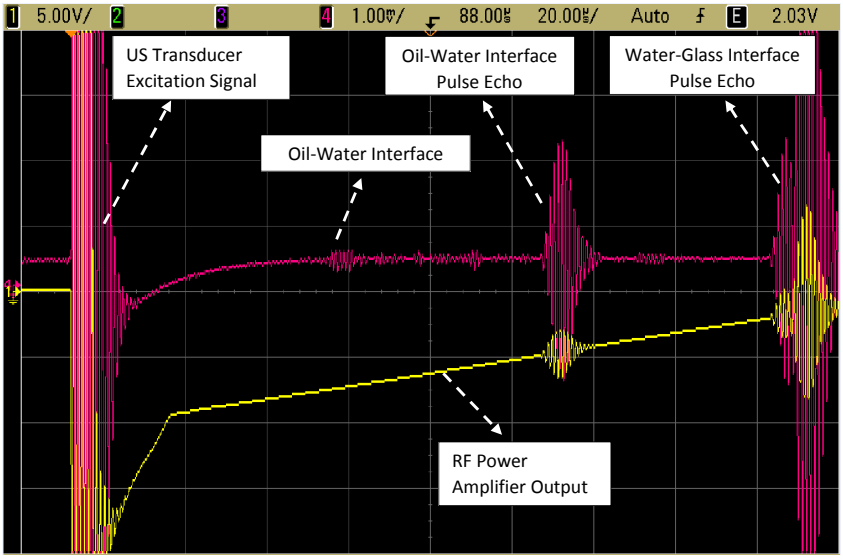

Figure 5.14: The received signal (purple) and the signal at the output of the RF power amplifier (yellow). The excitation is 5 cycles 1 MHz burst sinusoidal. The electrode pair is placed in z direction (current flow direction)

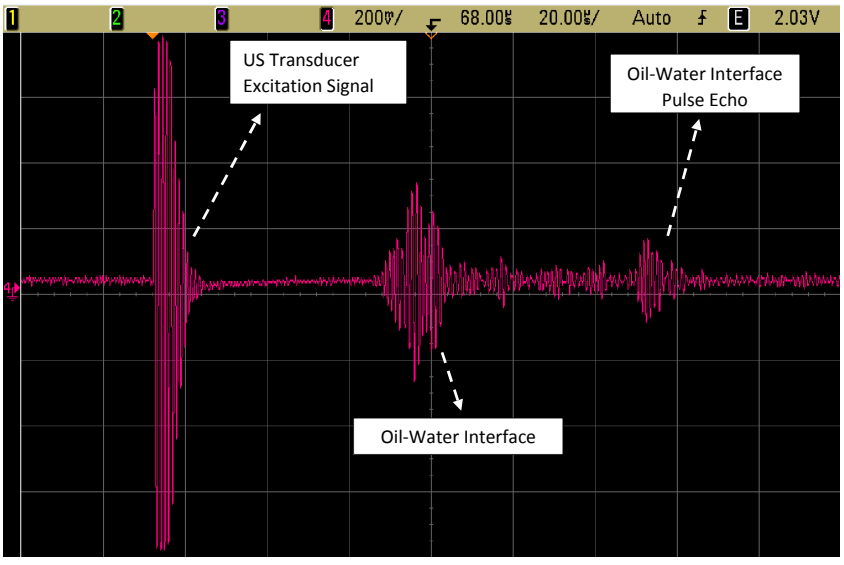

Figure 5.15: The received signal. The excitation is 5 cycles 1 MHz burst sinusoidal. The electrode pair is placed in x direction (normal of coil area)

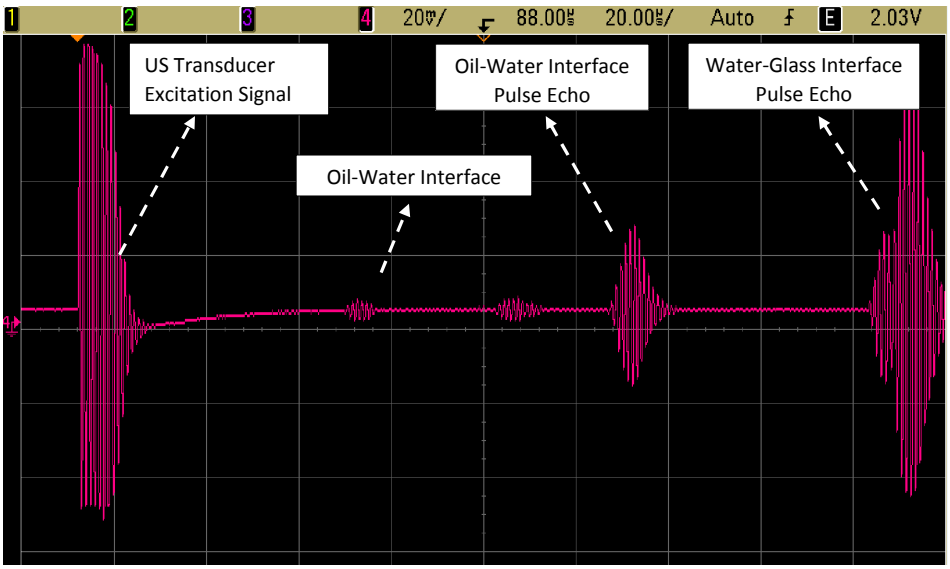

Figure 5.16: The received signal. The excitation is 5 cycles 1 MHz burst sinusoidal. The electrode pair is placed in z direction

CHAPTER 6

CONCLUSION

In this thesis, the LFEIT method is studied both numerically and experimentally. The forward and inverse problems of the LFEIT method are examined in detail. Forward problem deals with two different problems namely the original problem and the reciprocal problem of LFEIT, whereas inverse problem deals with the characteristics of the imaging modality and the image reconstruction methods. In the original problem, under a static magnetic field, a velocity current distribution is generated inside the conductive medium by an ultrasound excitation. Thereafter, a time dependent magnetic flux density which occurs due to the velocity current distribution is measured using an induction coil sensor. On the other hand, in the reciprocal problem, electric field distribution in the conductive medium is determined to derive the relation between the conductivity distribution and measurements.

In [1], the theory and basic assumptions behind the original problem of LFEIT is derived in detail. In this study, the reciprocal problem formulation and general time dependent reciprocity relation is reviewed.

In the original problem,the characteristics of the LFEIT method is analyzed using numerical methods. Finite element method (FEM) based commercial solver COMSOL Multiphysics is used to examine the piezoelectric, acoustic and electromagnetic modules. In the piezoelectric module, a 16 elements phased array transducer is modeled with a PZT-5H material to generate an ultrasound wave inside the conductive medium. In the acoustic module, an acoustic wave propagation problem is solved. The source of acoustic wave is the inward acceleration

applied to the interface of the piezoelectric material and conductive body. Note that, the contribution of the acoustic dipole sources due to the interaction of the velocity currents and the magnetic field is not taken into account. To validate the FEM based results of the acoustic module, the same problem is solved by developing an FDTD model. It is showed that the results are consistent with each other. In the electromagnetic module, the magnetic flux density and the induced voltage on the coil are calculated.

In the reciprocal problem, the electric field distribution in a conductive medium is calculated by using COMSOL Multiphysics. In that case, since the magnetic field module of COMSOL Multiphysics could not solve the problem accurately, the Poisson's equation in the mathematical module is used. The result of COMSOL Multiphysics are verified by an implemented FEM simulation and semi-analytical solution by using series expansion method.

In addition to these numerical studies, the feasibility and limitations of the LFEIT method are also explored. The problems of ultrasound frequency, the current limitation and the ultrasound exposure are being discussed. It is shown that, for high excitation frequency the amplitude of the received signal decreases; and for low frequency the spatial resolution of the imaging system decreases. For safety considerations, the current limitation is set to 2 A/m^2, and the maximum value of the ultrasound pressure (15 MPa) is determined according to this current amplitude. However, a pressure of 15 MPa is not feasible, since that much pressure results in cavitation in the tissue. To avoid tissue damage, the maximum allowed pressure is 1.5 MPa.

In the inverse problem part, the conductivity perturbation image is reconstructed by using different regularization methods. To that end, the sensitivity matrix of the imaging system is obtained by linearization. For linearization, the reciprocal electric field is assumed to be equal to the one calculated for the homogeneous conductivity distribution. The simulations show that the linearization assumption is valid up to 50% perturbation in the initial conductivity distribution. Consequently, a linear system of equations is obtained to reconstruct the true conductivity perturbation. The performance of the imaging system is

investigated by considering the number of independent measurements, the condition number of the sensitivity matrix, the sensitivity of each region, the decay behavior of the singular values. The number of the independent measurement can be increased by changing the transducer position or the steering angle of the pressure wave. The decay behavior of the singular values depends on the shape of the pressure wave and the coil configuration. In the case of single pulse pressure wave, the singular value decay pattern has a better behavior than the damped sinusoidal wave, that is the case of realistic pressure distribution. The coil configuration determines the sensitivity of each pixel. When the encircling coil is used the sensitivity of center pixel is low. To overcome the sensitivity problem of the center pixel, instead of the encircling coil, two xy coils can be used. However, as observed in their singular value pattern, the signal power obtained by the encircling coil is higher than the two xy coil case. Since the integral equation derived in the forward problem is in the form of IFK, the imaging problem is expected to be ill-posed. This is also shown by determining the condition number of the sensitivity matrix. Three different classes of regularization methods; spectral filtering, iterative, and sparse regularization methods, are implemented and compared to each other. The performances of these methods are similar to each other except the SD type iterative methods (e.g. SIRT). However, since the conductivity perturbation has a sparse distribution, the sparse regularization provides better results.

In the experimental study, a simple setup is built to explore the feasibility of the LFEIT method. To get a higher signal amplitude, instead of the realistic tissues, an oil-saline water medium is used. However, since the LFEIT signal amplitude remains under the noise floor, the signal could not be acquired in the proposed setup. The reason of low signal power can be listed as:

i-) The strength of the static field is low (0.3 T).
ii-) The US transducer cannot produce the pressure wave higher than 0.6 MPa.
iii-) The minimum detectable signal is in the order of μV.
iv-) The sensitivity of the induction coil is low.

In this thesis, the numerical studies of the LFEIT are investigated in 2D. The

limitations and the feasibility of the method is determined according to that results. In experimental part, the initial works are provided. As a consequence, there are some points that should be analyzed in the future. They can be listed as follows:

i-) 3D simulations to analyze the effect of the depth.
ii-) Development of fast and reliable numerical tools for the electromagnetic simulations.
iii-) Simulations on the realistic tissue geometries.
iv-) Development of the realistic phantoms and conducting experiments on them.
v-) Increasing the sensitivity of the induction coil.
vi-) Building stronger static field in the setup.
vii-) Design and implementation of low-noise receiver setup.

REFERENCES

[1] R. Zengin, *Electrical Impedance Tomography Using Lorentz Field.* PhD thesis, Middle East Technical University, 2012.

[2] P. C. Hansen, *Discrete Inverse Problems: Insight and Algorithms.* Society for Industrial and Applied Mathematics, 2010.

[3] C. C. Boring, T. S. Squires, T. Tong, and S. Montgomery, "Cancer statistics, 1994," *CA: A Cancer Journal for Clinicians*, vol. 44, no. 1, pp. 7–26, 1994.

[4] Y. Zou and Z. Guo, "A review of electrical impedance techniques for breast cancer detection," *Medical Engineering & Physics*, vol. 25, pp. 79–90, Mar. 2003.

[5] G. Simonetti, E. Cossu, M. Montanaro, C. Caschili, and V. Giuliani, "What's new in mammography.," *European journal of radiology*, vol. 27 Suppl 2, pp. S234–S241, 1998.

[6] K. Rosenberg, "Ten-year risk of false positive screening mammograms and clinical breast examinations.," *Journal of nurse-midwifery*, vol. 43, no. 5, pp. 394–5, 1998.

[7] T. Widlak and O. Scherzer, "Hybrid tomography for conductivity imaging," *Inverse Problems*, vol. 28, p. 084008, Aug. 2012.

[8] C. Barber, B. Brown, and I. Freeston, "Imaging spatial distributions of resistivity using applied potential tomography," 1983.

[9] D. C. Barber and B. H. Brown, "Applied potential tomography.," *Journal of the British Interplanetary Society*, vol. 42, no. 7, pp. 391–393, 1989.

[10] D. S. Holder and D. Djajaputra, "Electrical Impedance Tomography: Methods, History and Applications," 2005.

[11] N. G. Gencer, M. Kuzuoglu, and Y. Z. Ider, "Electrical impedance tomography using induced currents.," *IEEE transactions on medical imaging*, vol. 13, no. 2, pp. 338–350, 1994.

[12] I. L. Freeston and R. C. Tozer, "Impedance imaging using induced currents.," *Physiological measurement*, vol. 16, no. 3 Suppl A, pp. A257–A266, 1995.

[13] N. G. Gençer, Y. Ziya, and S. J. Williamson, "Electrical impedance tomography: induced-current imaging achieved with a multiple coil system.," *IEEE Transactions on bio-medical engineering*, vol. 43, no. 2, pp. 139–149, 1996.

[14] M. Joy, G. Scott, and M. Henkelman, "In vivo detection of applied electric currents by magnetic resonance imaging," 1989.

[15] G. C. Scott, M. G. Joy, R. L. Armstrong, and R. M. Henkelman, "Measurement of nonuniform current density by magnetic resonance.," *IEEE transactions on medical imaging*, vol. 10, no. 3, pp. 362–374, 1991.

[16] G. Scott, M. Joy, R. Armstrong, and R. Henkelman, "Sensitivity of magnetic-resonance current-density imaging," *Journal of Magnetic Resonance (1969)*, vol. 97, no. 2, pp. 235 – 254, 1992.

[17] E. J. Woo, S. Y. Lee, and C. W. Mun, "Impedance tomography using internal current density distribution measured by nuclear magnetic resonance," vol. 2299, pp. 377–385, July 1994.

[18] Y. Z. Ider, "Use of the magnetic field generated by the internal distribution of injected currents for Electrical Impedance Tomography (MR-EIT)," *Turkish J. of Electrical Eng. And Computer Sciences, ELEKTRIK*, vol. 6, no. 3, pp. 215–225, 1998.

[19] N. G. Gençer and M. N. Tek, "Forward problem solution for electrical conductivity imaging via contactless measurements.," *Physics in medicine and biology*, vol. 44, pp. 927–40, Apr. 1999.

[20] A. Korjenevsky, V. Cherepenin, and S. Sapetsky, "Magnetic induction tomography: experimental realization.," *Physiological measurement*, vol. 21, no. 1, pp. 89–94, 2000.

[21] G. H., "Magnetic induction tomography," vol. 1126.

[22] X. Li, Y. Xu, and B. He, "Imaging Electrical Impedance of Biological Tissue from Acoustic Measurements by means of Magnetoacoustic Tomography with Magnetic Induction (MAT-MI): A Model Study ," *IEEE Transactions on Biomedical Engineering*, vol. 54, no. 2, pp. 323–330, 2007.

[23] R. Xia, X. Li, and B. He, "Magnetoacoustic tomographic imaging of electrical impedance with magnetic induction.," *Applied physics letters*, vol. 91, p. 83903, Aug. 2007.

[24] Q. Ma and B. He, "Magnetoacoustic tomography with magnetic induction: a rigorous theory.," *IEEE Transactions on bio-medical engineering*, vol. 55, pp. 813–6, Feb. 2008.

[25] R. B. H. Wen, J. Shah, "NIH Public Access," *IEEE Trans Biomed Eng.*, vol. 45, no. 1, pp. 119–124, 1998.

[26] H. Wen, "Volumetric Hall Effect Tomography – A Feasibility Study," *Ultrasonic Imaging*, vol. 21, pp. 186–200, July 1999.

[27] a. Montalibet, J. Jossinet, and a. Matias, "Scanning Electric Conductivity Gradients with Ultrasonically-Induced Lorentz Force," *Ultrasonic Imaging*, vol. 23, pp. 117–132, Apr. 2001.

[28] Y. Xu, S. Haider, A. Hrbek, and I. X. I. Graz Univ Technol, "Magneto-acousto-electrical tomography: A new imaging modality for electrical impedance," in *13th International Conference on Electrical Bioimpedance/8th Conference on Electrical Impedance Tomography*, vol. 17, (Graz, AUSTRIA), pp. 292–295, 2007.

[29] S. Haider, a. Hrbek, and Y. Xu, "Magneto-acousto-electrical tomography: a potential method for imaging current density and electrical impedance.," *Physiological measurement*, vol. 29, pp. S41–50, June 2008.

[30] H. Zhang and L. V. Wang, "Acousto-electric tomography," *Proc. SPIE 5320, Photons Plus Ultrasound: Imaging and Sensing*, vol. 5320, pp. 145–149, July 2004.

[31] H. Lorentz, "The theorem of poynting concerning the energy in the electromagnetic field and two general propositions concerning the propagation of light amsterdammer akademie der wetenschappen 4 p. 176 (1896).," *Amsterdammer Akademie der Wetenschappen*, p. 4 p. 176, 1896.

[32] "COMSOL multiphysics, in www.comsol.com.."

[33] R. S. C. Cobbold, "Foundations of Biomedical Ultrasound," *Oxford University Press*, Dec. 2007.

[34] B. A. Auld, "Wave propagation and resonance in piezoelectric materials," *The Journal of the Acoustical Society of America*, vol. 70, no. 6, 1981.

[35] J. Yang, *An Introduction to the Theory of Piezoelectricity*, vol. 9. Springer US.

[36] B. Larisa, "The finite element method for the wave equation."

[37] D. S. M. Cook, Robert D. and M. E. Plesha, *Concepts and Applications of Finite Element Analysis*, vol. 9. John Wiley & Sons.

[38] H. Azhari, *Basics of Biomedical Ultrasound for Engineers*. John Wiley Sons, 2010.

[39] "ICNIRP (1998) guidelines for limiting exposure to time-varying electric, magnetic, and electromagnetic fields (up to 300 Ghz)."

[40] Food and D. Administration, "Revised (510k) diagnostic ultrasound guidance for 1993," February 1993.

[41] J. Abbott, *Rationale and derivation of Mi and Ti - A review*. Ultrasound Med. Biol 25(3), 1999.

[42] Food and D. Administration, "Use of mechanical index in place of spatial peak, pulse average intensity in determining substantial equivalence," April 1993.

[43] J. Smith, *Modern communication Circuits*. 2 ed.

[44] C. H. T. Richard C. Aster, Brian Borchers, *Parameter Estimation and Inverse Problems*. Academic Press, 2012.

[45] P. C. Hansen, *Rank-Deficient and Discrete Ill-Posed Problems: Numerical Aspects of Linear Inversion (Monographs on Mathematical Modeling and Computation)*. Society for Industrial and Applied Mathematics, 1998.

[46] J. B. Bell *Mathematics of Computation*, vol. 32, no. 144, pp. pp. 1320–1322, 1978.

[47] P. Hansen, "The discrete picard condition for discrete ill-posed problems," *BIT Numerical Mathematics*, vol. 30, no. 4, pp. 658–672, 1990.

[48] P. C. Hansen, "The l-curve and its use in the numerical treatment of inverse problems," in *in Computational Inverse Problems in Electrocardiology, ed. P. Johnston, Advances in Computational Bioengineering*, pp. 119–142, WIT Press, 2000.

[49] M. Hanke, *Conjugate Gradiednt type methods for ill-posed problems*. Scientific and Technical, Longman, 1995.

[50] V. Morozov, *Methods for Solving Incorrectly Posed Problems(translation ed.: Nashed M. Z.)*. New York: Springer, 1984.

[51] W. Auzinger, "Iterative solution of large linear systems," 2013.

[52] A. C. Kak and M. Slaney, *Principles of Computerized Tomographic Imaging (Classics in Applied Mathematics)*. Society for Industrial and Applied Mathematics, 2001.

[53] T. Strohmer and R. Vershynin, "A Randomized Kaczmarz Algorithm with Exponential Convergence," *Journal of Fourier Analysis and Applications*, vol. 15, pp. 262–278, Apr. 2008.

[54] L. Landweber, "An Iteration Formula for Fredholm Integral Equations of the First Kind," *American Journal of Mathematics*, vol. 73, pp. 615–624, July 1951.

[55] Y. Censor, D. Gordon, and R. Gordon, "Component averaging: An efficient iterative parallel algorithm for large and sparse unstructured problems," *Parallel Computing*, vol. 27, pp. 777–808, 2001.

[56] P. C. Hansen and M. Saxild-Hansen, AIR Tools – A MATLAB Package of Algebraic Iterative Reconstruction Techniques, Journal of Computational and Applied Mathemat- ics, 2011; doi:10.1016/j.cam.2011.09.039.

[57] A. Beck and M. Teboulle, "A fast iterative shrinkage-thresholding algorithm for linear inverse problems," *SIAM J. Img. Sci.*, vol. 2, pp. 183–202, Mar. 2009.

[58] J. M. Bioucas-Dias and M. a. T. Figueiredo, "A new twIst: two-step iterative shrinkage/thresholding algorithms for image restoration.," *IEEE Transactions on image processing : a publication of the IEEE Signal Processing Society*, vol. 16, pp. 2992–3004, Dec. 2007.

[59] K. Koh, S. Kim, and S. Boyd, "l1 ls: A MATLAB solver for large-scale l1-regularized least squares problems," 2007.

[60] C. B. Top, *Harmonic Motion Microwave Doppler Imaging Method.* PhD thesis, Middle East Technical University, 2013.

[61] A. M. Technologies, "Sintered neodymium-iron-boron magnets N42" [Online]. Available: www.arnoldmagnetics.com/WorkArea/DownloadAsset.aspx?id=5305

[62] Miteq, "Au-1291" [Online]. Available: https://www.miteq.com/docs/MITEQ-AU-1291-E1210.PDF

[63] A. Devices, "Dual, low noise, wideband variable gain amplifiers AD600/AD602" [Online]. Available: http://www.analog.com/static/imported-files/data_sheets/AD600_602.pdf

[64] U. C. Inan, "Design and implementation of the magnetic field sensor for biomedical applications," 2014.